Role of Molecular Opacities in Circumstellar Dust Shells

von

Dipl.-Phys. Christiane Helling

aus Berlin

Vom Fachbereich 04 (Physik)
der Technischen Universität Berlin
zur Erlangung des akademischen Grades

Doktor der Naturwissenschaften (Dr. rer. nat.)

genehmigte Dissertation

Berlin 1999

D 83

Promotionsausschuß

Vorsitzender: Prof. Dr. von Oppen
Berichter: Prof. Dr. E. Sedlmayr
Priv. Doz. Dr. J.P. Kaufmann

Tag der mündlichen Prüfung: 12.Mai 1999

Er liegt auf dem Berg und schaut in die Ferne. Über ihm schweben lichte Wolken. Unverwandt schaut er durch das Fernglas in der Erwartung des weißen Dampfers draußen auf dem See. Bald wird er in der himmelfarbenden Ferne vorüberziehen wie im Film. Und aus dem Schornstein steigt Rauch auf.

Tschingis Aitmatow, *Der weiße Dampfer*

Meinen Eltern

To my parents

Abstract

This thesis investigates the influence of molecular opacities on the structure and the dynamics of circumstellar dust shells around carbon stars on the Asymptotic Giant Branch (AGB). The investigations are performed in the framework of time-dependent spherical symmetric model computations, where a coupled equation system is solved describing the hydrodynamics, the chemical composition of the gas, the radiative transfer in grey approximation, and the dust formation, growth and evaporation in a self-consistent way. The role of the molecular opacities concerns the following: (i) molecular opacities have a decisive influence on the structure of the atmosphere as function of optical depth, and (ii) molecules can directly exert a considerable force on the gas by radiation pressure. The evaluation of both effects requires the calculation of the flux-mean opacity which in this work is either replaced by the Planck mean opacity (upper limit) or by the Rosseland mean opacity (lower limit).

New Planck mean and Rosseland mean gas opacities have been calculated and tabulated for different element abundances, based on several millions of spectral lines of CO, TiO, SiO, H_2O, CH, CN, C_2, C_3, HCN, and C_2H_2 beside several continuum sources. Both mean opacities show a similar behavior at high temperatures, but can differ by as much as three orders of magnitude at low temperatures due to the strong frequency-dependence of the molecular opacities. The larger Planck mean gas opacities reach about 10% and 30% of the dust opacity in case of a fully condensed carbon-rich and oxygen-rich gas, respectively.

In the model calculations, a large gas opacity (e. g. Planck means) generally causes a less dense atmosphere, which consequently leads to smaller amounts of dust, smaller mass loss rates, lower terminal wind velocities and lower dust-to-gas ratios.

When using the Planck means, both the initial static models and the dynamical models for *carbon stars* exhibit local pressure inversions in the inner regions, i. e. a local increase of pressure density with increasing distance from the central star. These inversions are caused by strong radiation pressure on molecules. A closer inspection in the (T, ρ) plane reveals that the inversions coincide with the maximum particle concentration of C_3, suggesting a causal connection. The occurrence of pressure inversions illustrates the important influence molecular opacities can have especially on the inner dust-free regions of a circumstellar shell.

Thus, strong molecular opacities cause two contrary effects: a general lowering of the density, but also local density enhancements caused by the pressure inversions. In conjunction with the dust formation, which strongly depends on density and temperature, new interrelations and additional effects occur in the models, which are not present in case of small gas opacities. For instance, radiation pressure on molecules can introduce perturbations into the velocity field, which may be amplified and can steepen into shocks by dust formation at larger distances. Shock waves generated

by the interior pulsation of the star can be damped and partly reflected when they encounter a finite region of increasing density.

An analysis of the chemical composition of the gas in the time-dependent models reveals a multi-layered structure of the molecules situated behind shock waves. The levitation of the outer atmospheres due to pulsation-induced shocks and/or radiation pressure on molecules leads to much larger molecular densities than expected from standard (static) model atmospheres, in particular regarding the polyatomic molecules like H_2O, CO_2, SO_2, HCN and C_2H_2. These molecules reach their highest particle densities at radial distance as large as 1.5 to 3 stellar radii. A comparison of the calculated column densities of these molecules with recent *Infrared Space Observatory* (ISO)-observations shows that the levitation provides a promising approach to explain the formation of the so-called "warm molecular layers"[1]. Dust formation at the outer edge of such a density-enhanced region amplifies the levitation and causes an additional *backwarming* of the molecular layer.

[1]This term has been invented by observational astronomers in order to describe the strong absorption and/or emission features attributed to these molecules.

Contents

List of Figures

List of Tables

"Der Zustand der Gegenwart ist die Wirkung der Vergangenheit."
Imanuel Kant

Chapter 1

Introduction

1.1 Frame & Status

The Asymptotic Giant Branch (AGB) phase corresponds to the short stage of stellar evolution during which intermediate- and low-mass stars (main-sequence mass $1 \ldots 8\,M_\odot$)[1] attain their highest luminosities ($3 \times 10^3 L_\odot \ldots < 5 \times 10^4 L_\odot$), but also experience heavy mass loss ($10^{-8} \ldots 10^{-4} M_\odot$/yr) with a dust-to-gas ratio of about $\approx 10^{-3}$ (Knapp 1985) and a relatively low outflow velocity of the order of 10 km/s which rapidly drives them towards the planetary-nebula phase and the final cooling to white dwarfs (Habing 1996, Le Bertre 1998, Wallerstein & Knapp 1998). AGB stars have a low effective temperature between $\sim 2000\,$K and $\sim 3200\,$K. Elemental abundances are – except for the carbon in carbon-rich stars – roughly the same as in the sun (Habing 1996, Wallerstein & Knapp 1998). Most AGB stars are variable on intermediate or long time scales. Mira variables, which are of special interest for this work, have pulsation periods of $100 - 1000$ days (Le Bertre 1998, $\sim 300 - 500$ days in Wallerstein & Knapp 1998) and large visual amplitudes of $> 2.5\,$mag. They belong to the class of long periodic variables. There is consensus that mass loss probably sets both the maximum luminosity that a star can achieve and the time it spends on its evolution up along the AGB (Gustafsson & Ryde 1996).

AGB stars are most revealing for critical issues in stellar structure, nucleosynthesis and stellar evolution. Their circumstellar envelopes produce almost all nuclei of interstellar dust (Gehrz 1989) and the carbon stars alone return already about $0.3\,M_\odot$/yr to the Galaxy (Wallerstein & Knapp 1998). Mass loss from AGB stars is a main, perhaps the major, contributer to the evolution of the light element abundances ($\leq m_{\mathrm{Fe}}$) in the Galaxy. AGB stars are therefore important interfaces between stellar and interstellar media as they have a strong relevance for the circuit of matter of any galaxy as every star is born with the elemental composition of the interstellar medium that forms it.

Already in the early days of spectroscopy, the differences between oxygen-rich (M-type) and carbon-rich (C-type) AGB stars have been noticed as the former are characterized by molecules like TiO and H_2O but the latter by superposed bands of molecules like CH, CN, and C_2. The reason is the different chemical composition

[1]Carbon-rich AGB stars have masses approximately between 1.2 and 4 $M_\odot$. For stellar masses greater than about 4 $M_\odot$ hot-bottom burning is thought to prevent carbon-star formation (Boothroyed et al. 1993) depending on the metalicity of the star (Gustafsson & Ryde 1996).

caused by the different carbon-to-oxygen abundance and the chemical blocking due to the CO molecule which is photodissociated only at distances from the star of typically $\lesssim 10^{17}$ cm depending on the mass loss rate (Mamon et al. 1988). Another difference is the kind of dust particles formed in these envelopes: carbonaceous particles in carbon-rich envelopes but silicates and other metal-oxides in oxygen-rich ones. Infrared observations indicate that red giants often radiate strongly in the IR for which circumstellar dust grains were found to be the cause. The wavelength dependence of this excess emission suggests the dust grains to be either of carbonaceous[2] or silicate[3] type (Stein et al. 1969, Woolf & Ney 1969). The visual and near IR[4] colors of oxygen-rich and carbon-rich stars are quit different because of the very different dust opacities (amorphous or graphite). Carbon dust is opaque at visual wavelengths while silicate dust is not (soot is black, e.g. glass is transparent). As a result, carbon-rich stars are much more obscured at a given mass loss rate than oxygen-rich stars are and have much larger IR excesses.

Dust particles have a large impact on the structure of a circumstellar envelope by their ability of scattering and absorbing photons. Momentum is thus transfered from the radiation field to the dust component and next from the dust particles to the gas by frictional forces. The efficiency of these processes is influenced by the size of the particles, the density of the gas, but also by the luminosity of the star (Habing 1996). If dust is once present, radiation pressure on dust is very likely the reason for mass loss of late type stars.

However, heavy mass loss of about $10^{-7} M_{\odot}/\mathrm{yr}$ has also been observed for stars without dust in the circumstellar envelope for which radiation pressure due to large gas opacities has been suggested as possible wind driving mechanism. One example is the symbiotic star EG Andromedae ($T_{\star} = 3800$K, van Buren et al. 1994)

To shed some light from the theoretical point of view, it is important to build a model which treats all these processes consistently. Considerable progress has been achieved in the last two decades concerning the dynamic modeling of the atmospheres and circumstellar envelopes of Miras and other long-periodic variables (Wood 1979, Bowen 1988, Fleischer et al. 1992, Winters et al. 1994, Höfner et al. 1995)[5] but also concerning the consistent treatment of a detailed radiative transfer in hydrostatic model atmospheres (e.g. Jørgensen 1989, Plez et al. 1991, Gustafsson & Jørgensen 1994, Tsuji et al. 1994). While the main interest of the dynamic models for cool stars has been to treat the complex of dust formation, growth and evaporation self-consistently coupled to the hydrodynamic complex, the main interest of static models has been the interpretation of stellar spectra on the basis of detailed radiative transfer calculations. The drawbacks are the necessity of the grey approximation in the radiative transfer in the first case and the neglect of dynamical effects in the latter case.

Nevertheless, hydrodynamic models have successfully been used to predict mass loss rates, dust-to-gas ratios, outflow velocities (Fleischer et al. 1995, Winters et al. 1997a), light curves of long-periodic variables which are heavily obscured by carbon-rich circumstellar dust shells, as well as their spectral energy distributions

[2] 11.3μm feature ascribed to SiC (Treffers & Cohen 1994)
[3] $10 - 18\mu$m feature ascribed to amorphous silicate (Day 1974)
[4] near-IR $\approx 1 - 5\,\mu$m
[5] For a recent review on time-dependent hydrodynamic models see Woitke (1998).

(Winters et al. 1994b). Prominent examples are IRC+10216 (Winters et al. 1994a) where the distance of the object could be deduced, and AFGL 3068 (Winters et al. 1997a). Evidence for size distributions for grains to be ejected into the ISM (Winters 1998) and for the heteromolecular composition of oxygen-rich grains in dependence on the hydrodynamical situation (Jeong et al. 1999) has been gained. A sample of time-dependent hydrodynamic models has been used to come up with a mass loss formula for a particular range of stellar parameters (Arndt et al. 1997) which was successfully applied in modeling tip-AGB stellar evolution in the presence of a dust-induced, carbon-rich "superwind" (Schröder et al. 1999).

Hydrostatic models are in use for detailed synthetic spectrum computations for cool giant stars, e.g. TX Piscum (Jørgensen 1989, Ohnaka et al. 1998) or the brown dwarf Gliese 229B (e.g. Allard et al. 1996), but also for hotter supergiants like R Coronae Borealis (Asplund et al. 1997), and for abundance analysis of a wide variety of stars (e.g. Plez et al. 1992, Tsuji et al. 1994, Asplund et al. 1998).

Recently, synthetic spectrum computations have been performed on top of hydrodynamic model structures (Höfner et al. 1998) by Loidl et al. (1998) and Alvarez & Plez (1998) allowing for a study of the phase variation of the molecular absorption features. It has been pointed out that molecular features, which vary in time, cannot be computed from a series of hydrostatic model spectra. For example, Tsuji et al. (1997) used static model atmospheres to analyze observed SWS[6] spectra of a Mira (S Virgenis) but needed to introduce a "warm molecular layer" at about $2\,R_\star$, which was suggested to be generated by pulsation shocks, in order to explain e.g. H_2O excess absorption and CO excess emission in the observed spectra.

At first, however, the basic results of hydrodynamic model computations of circumstellar envelopes as originally presented by Fleischer et al. 1992 (and later also by Höfner & Dorfi 1997) and our present understanding of the principle scenario of dust driven winds will be summarized.

1.2 Basic results of time-dependent hydrodynamic models

The present status of time-dependent modeling of circumstellar envelopes of cool pulsating AGB stars concerns the investigation of the complex interplay between hydrodynamics, thermodynamics, dust formation and evaporation, chemistry, and radiative transfer. In order to solve the respective equations for such a complex system (Sect. 4.1) in an acceptable amount of time, approximations like grey radiative transfer, equilibrium chemistry and spherical symmetry have to be applied.

The radial course of time-dependent dust driven wind models is roughly divided into two different zones:

1. The innermost region ($\lesssim 2R_\star$) is characterized by a large density gradient. The gas elements are periodically hit by shock waves and the gas is levitated by the instantaneous outward accelerations.

[6]Short Wavelength Spectrometer

2. The outer region ($\gtrsim 2R_\star$) is characterized by a much slower density decrease, i.e. a larger scale hight. At about $2R_\star$, effective dust formation sets in and radiation pressure on dust causes an acceleration of the gas by friction due to momentum transfer.

According to the large density gradient in the atmosphere, small scale waves (subsonic), created e.g. at the inner boundary by a piston, steepen up into strong shocks. In the innermost regions, these shocks cause large time variations of the atmospheric structure which, nevertheless, can still be considered as a "disturbance" of the static stratification. In the outer atmosphere, shock waves cause a completely different dynamical behavior of the gas which no longer can be understood on the basis of static or stationary models.

Shock waves introduce a new, outward directed, additional force on the gas which causes a levitation of the outer atmosphere resulting in densities being larger by orders of magnitudes compared to static models. The gas being hit by a shock wave is strongly compressed and, hence, can form dust more easily. Radiation pressure on dust causes a further outward acceleration of the gas since momentum is transfered by friction. Moreover, perturbations can be introduced into the velocity field by radiation pressure on dust which may result in the creation of a new, dust induced shock wave. The gaseous material is again compressed in the post-shock region and favors further dust growth.

The newly formed dust layer effectively blocks the outgoing radiation and heats the material in lower regions closer to the star. This backwarming effect temporarily prevents the formation of dust by an increase of temperature in these inner regions. Next, the new dust layer is driven out by radiation pressure, thereby becoming transparent again (radial dilution) and a new cycle of dust formation begins. The result is an inhomogeneous distribution of the dust across the circumstellar envelope: the dust grains are concentrated in distinct layers.

The outflow is very likely initiated by pulsation but it is accelerated outwards by the radiation pressure on dust. Although the interior pulsation plays such an important role for the onset of dust formation, pulsation alone cannot drive a substantial mass loss in models discussed in Fleischer (1994). Further findings in the models are as follows.

Exterior κ-mechanism: Even models without an external stimulation via the interior pulsation can produce a shell-like dust structure, shock waves, and an outflow only due to the presents of large amounts of dust. The dust complex builds up an self-maintaining mechanism which can produce an outflow and strong shock waves which pass the atmosphere. The density scale hight must be sufficiently low at small radial distances to allow dust formation already in the initial phase, and the backwarming will then initiate pressure-driven waves. Fleischer (1994) remarks that such κ-instabilities could well develop also in models where radiation pressure on molecules causes an initial levitation of the atmosphere.

Eigenperiod: The exterior κ-mechanism introduces a characteristic time-scale or characteristic period (eigenperiod) to the system. The eigenperiod is the characteristic time scale between two dust-induced shocks, and is inherent to the dust-forming system. It is anti-correlated to the C/O-ratio, i.e. an increase of C/O increases the amount of condensible matter and causes a shortening of the eigenperiod. The eigenperiod increases with higher stellar luminosity.

Multiperiodicity: A model is multiperiodic if the piston period divided by the atmosphere's eigenperiod yields an integer value. A multiperiodic model shows after $n > 1$ periods the same radial structure like n periods ago. Also models without an eigenperiod can show multiperiodicity since the characteristic time scale between two subsequent dust-induced shocks must not be constant.
If the eigenfrequency and the frequency of the exterior force have an integer ratio, constructive interference occurs. Otherwise, destructive interference causes irregular oscillations of the system or even chaotic oscillations. A Lagrangian layer of such atmospheres can be considered as a system of non-linear coupled oscillators (Geyer 1997). From detailed analysis of single Lagrangian elements, Fleischer (1994) concluded that multiperiodicity is a consequence of the hydrodynamics rather than of the dust complex: the dust shell is forced by the pulsation to oscillate with a certain period, defined by the hydrodynamic conditions in the circumstellar shell, which in turn are also a consequence of the dust formation process. A key mechanism to multiperiodicity is the periodic damping of shock waves by the previously formed dust.

Dependence on the input parameter:
• An increasing stellar mass causes an decreased mass loss rate because of the larger gravitational force to be overcome.
• An increasing C/O ratio causes an increasing final outflow velocity because the radiation pressure on dust is increased since more carbon is available to form carbon dust. In contrast, the mass loss rate decreases since the gas density decreases due to the increasing outflow velocity. Consequently, the gas-to-dust ratio is not much affected.
• A decreasing stellar luminosity causes decreasing mass loss rates and decreasing final outflow velocities since the radiative acceleration is increased.
• A higher piston amplitude causes a stronger levitation. The higher input of mechanical energy results in an increased mass loss rate. The final outflow velocity is not affected since the interior pulsation can only affect the inner regions whereas the outflow velocity is determined by the radiation pressure on dust at large radial distances.

1.3 Radiation pressure on molecules

Since long, strong gas opacities have been in discussion as a possible wind initiator (e.g. Maciel 1976, Jørgensen & Johnson 1992, Achmad et al. 1997) not only due to atomic lines, but also due to the rich line spectra of molecules obeying a large potential of absorbing radiation and therefore, influencing the hydrodynamics by a possibly large radiation pressure. Many investigations have been performed regarding this effect in the framework of hydrostatic models (e.g. Jørgensen & Johnson 1992), some in the framework of stationary models for supergiants (e.g. Achmad et al. 1997) and for Miras (e.g. Maciel 1976).
The *radiative acceleration* (see also Sect.4.1.1)

$$a_{\rm rad} = \frac{4\,\pi}{c}\int_0^\infty \chi_\nu H_\nu d\nu = \frac{4\,\pi}{c}\chi_{\rm H} H,$$

which enters into the *equation of motion* (see Eq. 4.4), becomes especially important if $a_{\rm rad}$ exceeds the local gravitational acceleration g, since it becomes the dominant force in this case. The radiative acceleration is determined by the interplay between the opacity χ_ν and the Eddington flux H_ν.

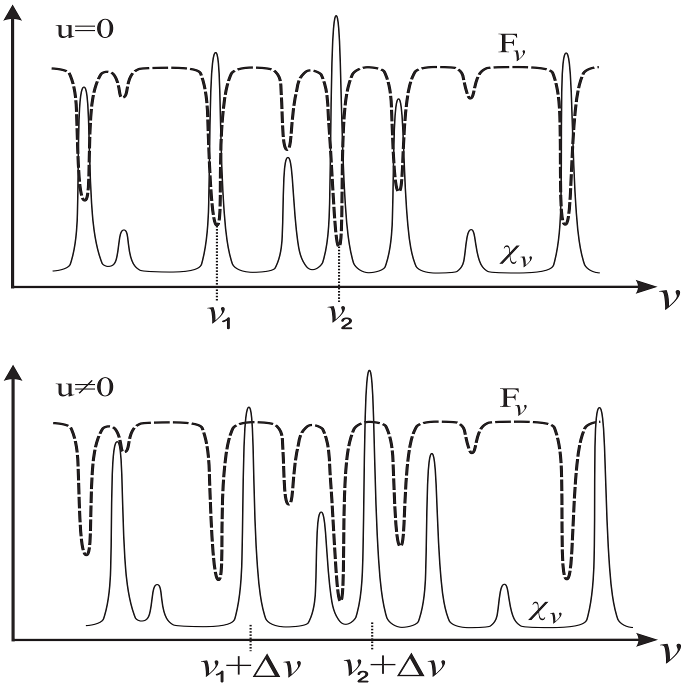

Figure 1.1: The correlation between the radiation flux $F_\nu = 4\,\pi\,H_\nu$ and opacity χ_ν with (lower panel) and without (upper panel) a velocity field u

In hot and dense regions of an atmosphere, where the mean free path of all photons of arbitrary wavelengths is smaller than a characteristic scale hight of the medium, the radiative energy can only escape where the opacity of the gas is small (*diffusion limit*). Hence, large fluxes occur at frequencies where the gas opacity is small (upper panel, Fig. 1.1). In the diffusion approximation $H_\nu \sim 1/\chi_\nu$ holds (e.g. Mihalas 1978, p. 51). However, in the outer part of the atmosphere and the circumstellar envelope the gas becomes optically thin and the diffusion approximation is not valid. A correlation $H_\nu \sim 1/\chi_\nu$ might still exist, if the opacity χ_ν of the gas in the photosphere (where the radiation emerges) had a very similar ν-dependence as the gas at the position of interest. Such a situation, however, is very unlikely to occur, since the gas is in a different physical state (smaller ρ, lower T) than in the photosphere. Consequently, the lines will usually have different relative strengths and profiles. Moreover, the gas may be in a different chemical state, i.e. new opacity species can be present, contributing with different lines. In addition, the flux is not correlated to the local physics any more in the optically thin regime, and lines may be Doppler-shifted to frequencies where flux escaped from inner layers ($\nu_1 + \Delta\nu$, $\nu_2 + \Delta\nu$, lower panel, Fig. 1.1). For example, if the gas moves with a hydrodynamical velocity $u = 20\,$km/s and the thermal velocity is $v_{\rm th} = 0.5\,$km/s (e.g. TiO at 1000 K), a line would be shifted by about 40 Doppler-widths form its original position ν_0 (see Sect. 3.1.1.1). Regarding the flux weighted mean opacity $\chi_{\rm H}$ which enters into the equation for the radiative acceleration $a_{\rm rad}$, two cases can be distinguished:

i) $H_\nu \sim 1/\kappa_\nu \;\Rightarrow \chi_{\rm H} = \chi_{\rm Ross}$
when a large flux is correlated to a small opacity

ii) $\chi_{\rm H} \approx \chi_{\rm Planck}$
when the flux is not correlated to the opacity.

The latter approach seems to be more reasonable in the optically thin case, where the anti-correlation between χ_ν and H_ν has likely disappeared as argued above. Case ii) will usually lead to much larger values of $a_{\rm rad}$, since $\chi_{\rm Planck}$ can be larger than $\chi_{\rm Ross}$ by as much as 3 orders of magnitude (see Sect. 3.3). Therefore, models where the flux weighted mean opacity is approximated by the Planck mean gas opacity $\chi_{\rm Planck}$ can be used as a tool to study the **upper limit** of the effects molecules can have on the structure and the dynamics of extended atmospheres while models computed with a Rosseland mean $\chi_{\rm Ross}$ or a constant gas opacity can serve as the **lower limit** case.

This work intends to contribute to the above mentioned discussion whether mass loss can be influenced or even initiated by radiation pressure on molecules by such studies in the framework of time-dependent hydrodynamic models.

1.4 Aim and structure of this work

The aim of this thesis is to investigate the role molecular opacities can play in circumstellar dust shells. Beside providing the chemical reservoir for dust formation, molecules may also have a direct influence on the structure and the dynamics of the atmosphere of AGB stars. While the former is based on the dominant influence of the molecular opacities in the inner atmosphere, the latter is a consequence of the strong radiation pressure on molecules as outlined above. Molecular opacities enter into the system of equations which describes the non-linear coupling between the hydrodynamics, thermodynamics, radiative transfer, chemistry, and the dust complex via a force-term in the equation of motion and via the calculation of the optical depth.

It shall be studied how molecular absorption interacts with the local velocity field and which influence it has on the density structure of circumstellar dust shells. The investigations aim on a better understanding of the influence molecular opacities can impose on the dust formation by their effect on hydrodynamics and thermodynamics.

The work is structured as follows:

Chapter 1 sets the state regarding the classification of the stars mainly concerned in this work and regarding the theoretical modeling of stellar atmospheres and circumstellar dust shells. The idea of radiation pressure on molecules with regard to the presence of strong velocity fields is outlined.

Chapter 2 discusses the abundances of the molecules with special regard to those species entering into the calculations of the gas opacities. These investigations are based on the assumption of chemical equilibrium and serve as a preparation of the following chapter.

Chapter 3 gives an overview about the theory of opacity calculation in LTE as well as the methods of opacity computation applied in this work. Rosseland and Planck mean gas opacities are calculated for various elemental compositions for temperature $T \epsilon$ [500K, 10 000K] and for total hydrogen densities $n_{<\rm H>} \epsilon$ [$10^5 {\rm cm}^{-3}, 10^{15}$ ${\rm cm}^{-3}$]. Differences are discussed for carbon- and oxygen-rich gases with solar, LMC, and SMC[7] metalicities. The results are discussed in comparison to similar computations of other works. Furthermore, molecular opacities and dust opacities are compared to each other. It is investigated which degree of condensation a gas must achieve to cause the dust to become the dominating opacity species. It is shown, for example, that pure iron dust is always negligible in comparison to the molecular gas opacities.

Chapter 4 contains the complex of modeling stellar atmospheres and circumstellar dust shells for which, at first, the theoretical background is outlined. In the framework of static models it is shown that, if the molecular opacities exceed a certain critical value, the radiation pressure on molecules becomes locally the dominating force in the equation of motion. In this case pressure inversions occur in order to stabilize the system. It is investigated whether these pressure inversions also occur in hydrodynamic models where the inner regions of the atmosphere is perturbed by the interior pulsation. Furthermore, the influence of the molecular opacities on the overall density of the circumstellar shell is studied, and hence, its influence on mass loss rate, outflow velocity and dust-to-gas ratio. Since molecules dominate mainly the opacity where no dust has formed yet, the inner radial regions of the circumstellar shells are studied in detail with view on a possible influence of molecular opacities on the velocity field. It is investigated how the propagation of shock waves generated by the interior pulsation is modified by the presents of pressure inversions, and which additional effects can occur due to the complex interplay between dust formation, shock propagation, and strong molecular absorption.

Recent ISO[8] observations suggest the presents of so-called "warm molecular layers" as possible explanation for excess absorption of e.g. H_2O in the framework of static models. It is therefore investigated whether the levitation by shocks or by radiation pressure on molecules may be part of the explanation for the generation of such molecular layers.

Chapter 5 summarizes the results of this work and gives an outlook regarding further important topics to be studied concerning dust forming environments.

[7] LMC = Large Magellanic Cloud, SMC = Small Magellanic Cloud
[8] ISO = Infrared Space Observatory

"Also schließt er messerscharf, daß nicht sein kann, was nicht sein darf"
Wilhelm Busch

Chapter 2

Composition of the gas

In order to determine any kind of opacity, the composition of the matter has to be known. In this work, the state of the gas is assumed to be in local thermodynamic equilibrium (LTE), and the concentrations of atoms, ions, and molecules are computed by assuming chemical equilibrium (CE). This chapter regards the composition of the gas and especially discusses the concentration of those molecules which enter into the opacity calculation.

The most realistic treatment of the formation of molecules which allows for non–equilibrium effects is the solution of a complete rate network for all reactions possibly involved in the formation process. Because a mere complete rate network is capable of describing chemical non-equilibrium situations, large effort has been put into its construction by several workers (e.g. Beck 1993, Patzer 1998), the most serious problem being still the missing data for the reaction rates. Since such a rate network is computationally far too time consuming for the purposes of this work, chemical equilibrium is assumed here. In general, the assumption of CE is justified in situations where (i) the expansion time scale is small compared to the formation time scales of the molecules and where (ii) ionizing photons are absent (Beck et al. 1992).

2.1 Chemical equilibrium

The chemical equilibrium is a consequence from the thermodynamical principle of the minimization of the free enthalpy $G = E + p\,V - T\,S$ for a thermodynamical system at a given temperature T and pressure p. It expresses a competition between the minimization of the energy E and the maximization of the entropy S.

In a thermodynamic equilibrium state, the partial pressure of the molecule A_aB_b is given by the law of mass action

$$p(A_aB_b) \;=\; \frac{p(A)^a p(B)^b}{(p^{\ominus})^{a+b-1}} \exp\left(\frac{\Delta G^{\ominus}(T)}{RT}\right), \tag{2.1}$$

where $\Delta G^{\ominus}(T)$ is the free enthalpy of formation for the fictitious reaction $aA + bB \rightarrow A_aB_b$ at standard pressure $p^{\ominus}$, a and b being the stoecheometric factors of the atoms A and B, respectively. It is convenient to introduce a so-called pressure equilibrium constant $K_p(T)$ such that

$$K_p(T) = \frac{p(A_a B_b)(p^{\ominus})^{a+b-1}}{p(A)^a p(B)^b}. \tag{2.2}$$

The temperature dependence of $K_p(T)$ can be fitted with a 4th-order polynom to the data of e.g. the JANAF tables (Chase et al. 1985) with the coefficients $c_0 \ldots c_4$

$$\log K_p(T) = c_0 + c_1\theta + c_2\theta^2 + c_3\theta^3 + c_4\theta^4, \tag{2.3}$$

where $\theta = T/5040K$. In addition, the principle of element conservation

$$\epsilon_{\rm el}\, n_{<\rm H>} = \sum_{\rm Species} a_{\rm y}\, n_{\rm y} \tag{2.4}$$

has to be fulfilled. $n_{\rm y}$ is the number density of the species y containing the element el and $\epsilon_{\rm el}$ the elemental abundance of the element el with respect to hydrogen. The number densities $n_{\rm y}$ can be converted into partial pressure $p_{\rm y}$ by use of the ideal gas law such that $p_{\rm y} = n_{\rm y}\, kT$.

2.1.1 Numerical approach

The chemical equilibrium is numerically treated as a system of algebraic equations. Each molecule and each ion is represented by one equation given by the law of mass action (Eq. (2.1)) which is substituted into the equation of element conservation (Eq. (2.4)). The system of equations is completed by describing the charge conservation. This system of N([1]) equations with N unknowns is solved by a Newton-Raphson iteration. The routine used here bases on the work of Gail & Sedlmayr (1986) which has been improved and extended (Woitke 1997).

The basic input parameters are

- the gas temperature T [K],
- the total hydrogen number density $n_{<\rm H>} = \rho/\sum_{\rm el}\epsilon_{\rm el} m_{\rm el}$ [cm^{-3}], ρ being the gas density and $m_{\rm el}$ the atomic weight of the element el.
- the elemental abundances $\epsilon_{\rm el}$ (see Tab. 2.1) and the carbon-to-oxygen ratio $\epsilon_{\rm C}/\epsilon_{\rm O}$ (hence fore called C/O)
- polynomial coefficients for $\log K_p(T)$ for 148 molecules and ions[2]

[1] $N-1$ equations for the elements and one for electrons

[2] The $c_{\rm i}$ (i=0, ... ,4) are mainly taken from Gail & Sedlmayr (1986) but for TiO, TiO_2, Ti^+, C_3, Si^+, S^+, Fe^+, new polynomial fits were performed from the JANAF tables (Chase et al. 1985). Coefficients for C_3H and TiS were taken from Tsuji (1973), and those for TiC were kindly provided by Gauger (1997).

	solar		LMC	SMC		
element	$\epsilon'_{\rm solar} = \log(10^{\epsilon_{\rm el}})$	reference	$\epsilon'_{\rm LMC} = \log(10^{\epsilon_{\rm el}})$	$\epsilon'_{\rm SMC} = \log(10^{\epsilon_{\rm el}})$	reference	element
H	12.00	AG89	12.00	12.00	RD92	H
He	10.99	"	10.94	10.91	"	He
C	8.60	G91	8.04	7.73	"	C
N	7.97	GN93	7.14	6.63	"	N
O	8.87	"	8.35	8.03	"	O
Ne	8.07	"	7.61	7.27	"	Ne
Na	6.33	AG89	7.15	5.96	"	Na
Mg	7.58	"	7.47	6.98	"	Mg
Al	6.47	"	[solar][a]	6.40	AG89, RD92	Al
Si	7.55	"	7.81	7.03	RD92	Si
S	7.21	"	6.70	6.59	"	S
K	5.12	"	[solar][a]	[solar][a]	AG89	K
Ca	6.36	"	5.89	5.69	RD92	Ca
Cr	5.67	"	5.47	5.10	"	Cr
Mn	5.39	"	5.21	5.03	"	Mn
Fe	7.51	"	7.23	6.84	"	Fe
Ni	6.25	"	6.04	5.85	"	Ni
Ti	4.93	B92	4.81	4.49	"	Ti

Table 2.1: Logarithmic elemental abundances, which are used in this work and which are derived from observations of the solar photosphere. Listed are also the elemental abundances for the Large Magellanic Cloud (LMC) and the Small Magellanic Cloud (SMC). The abbreviations refer to: AG89 = Anders & Grevesse (1989), G91 = Grevesse et al. (1991), GN93 = Grevesse & Noels (1993), B92 = Bizzarri et al. (1992), RD92 = Russel & Dopita (1992).

[a] Not all the values for Al and K were available for the LMC and the SMC, therefore, the solar elemental abundances have been assumed.

2.1.2 Influence of thermo-chemical data

The correctness of the thermo-chemical data depends very much on the progress made by experimental chemistry. The thermo-chemical data used by Tsuji (1973) and those obtained from the JANAF tables (Chase et al. 1985) differ partly and large deviations in $\log K_p$ can be found at low temperatures for certain molecules.

For instance, deviations in the $\log K_p$-data for TiO_2 result in an increase of the TiO number density of up to three orders of magnitudes with respect to the results of Tsuji (1973). This was tested by inserting the $\log K_p$ data from Tsuji (1973) for TiO and TiO_2 in the data collection used in this work.

Resent investigations of Köhler et al. (1997) have lined out that the new data for the MgO bond energy (3.5 eV) causes a much smaller MgO number density because the free oxygen is rather bound in OH which has a somewhat higher bond energy (4.4 eV) than MgO. The situation was quite different with a slightly higher bond energy of MgO as suggested by elder determinations of the MgO's dissociation energy.

Furthermore, also the choice of the molecules and ions included in the sample for which the chemical equilibrium calculation is done, is very important for the results. This concerns the atomic opacity species at high temperatures (compare Table 3.2) which are overestimated if the respective ions are not taken into account. At the low temperature end of the opacity tables, also the molecular opacities may be overestimated if important molecular species are missing in the chemistry calculation (compare Table 3.3).

2.2 Concentrations of the line opacity molecules

Hydrogen and helium account for 98% of the mass in stars of solar composition. In all hydrogen-rich, cool stars, H_2 is the most abundant molecule throughout the atmosphere. It is, followed by CO, one of the most stable molecules. Molecules composed of H, C, N, and O or even heavier elements are much less abundant.

Figures 2.1 and 2.2 show contour plots illustrating the concentrations relative to hydrogen ($\log n_{\rm y}/n_{<\rm H>}$) of the molecules H_2O, CO, SiO, TiO, CH, CN, HCN, C_2, C_3, and C_2H_2 in the (T, $n_{<\rm H>}$) plane. The gas temperature T ranges from 500K to 10 000K, the total hydrogen density $n_{<\rm H>}$ covers a range from 10^5cm^{-3} to 10^{15}cm^{-3} on a grid of 101×101 points. Figure 2.3 shows the absolute number densities of the opacity species together with other abundant molecules and ions as function of the gas temperature T for a representative gas pressure $P_{\rm gas}$=1 dyn/cm^2.

• <u>Carbon monoxide CO</u>

Carbon monoxide is one of the most stable molecules due to its very high dissociation energy (11.1 eV). It is very abundant in a carbon-rich as well as in an oxygen-rich chemistry over a wide range of temperatures and densities (chemical CO blocking). However, at temperatures lower than about 600K the carbon in the oxygen-rich case and the oxygen in the carbon-rich case is no longer locked in CO. This happens at even lower temperatures for decreasing densities. The now available carbon goes into CH_4 but in the carbon-rich case also into C_2H_2 (see e.g. Helling et al. 1996). The available oxygen causes an increase of the SiO and H_2O densities but also TiO peaks at low temperatures and high densities in the carbon-rich case (left column, Fig. 2.3). At temperatures roughly higher than 3000K (depending on density) carbon is mainly present in atomic form.

• <u>Titan oxide TiO</u>

The concentration of titan oxide has a plateau of maximum number density at temperatures of roughly 3000K down to 1500K in the oxygen-rich case. This temperature range becomes narrower with decreasing density. A plateau of similar concentration occurs in the carbon-rich case between about 1000K and 800K. Hence, independent on the carbon-to-oxygen ratio, TiO will play an important role at low temperatures. In regions where TiO is less abundant, the Ti is either bounded by TiO_2 at lower temperature or in atomic form at high temperatures until it is ionized (see Fig. 2.3). At low temperatures, TiO_2 contains most of the titanium available in an oxygen-rich as well as in a carbon-rich case[3].

The thermo-chemical data used by Tsuji (1973) lead to a somewhat different picture. The main difference is that TiO_2 exceeds TiO at much lower temperatures ($T \sim 650$ K at $P_{\rm gas} = 1$ dyn/cm^2). Therefore, in this work, TiO has a higher number density compared to Tsuji (1973).

[3] For implications on oxygen-rich dust formation see Jeong et al. (1998).

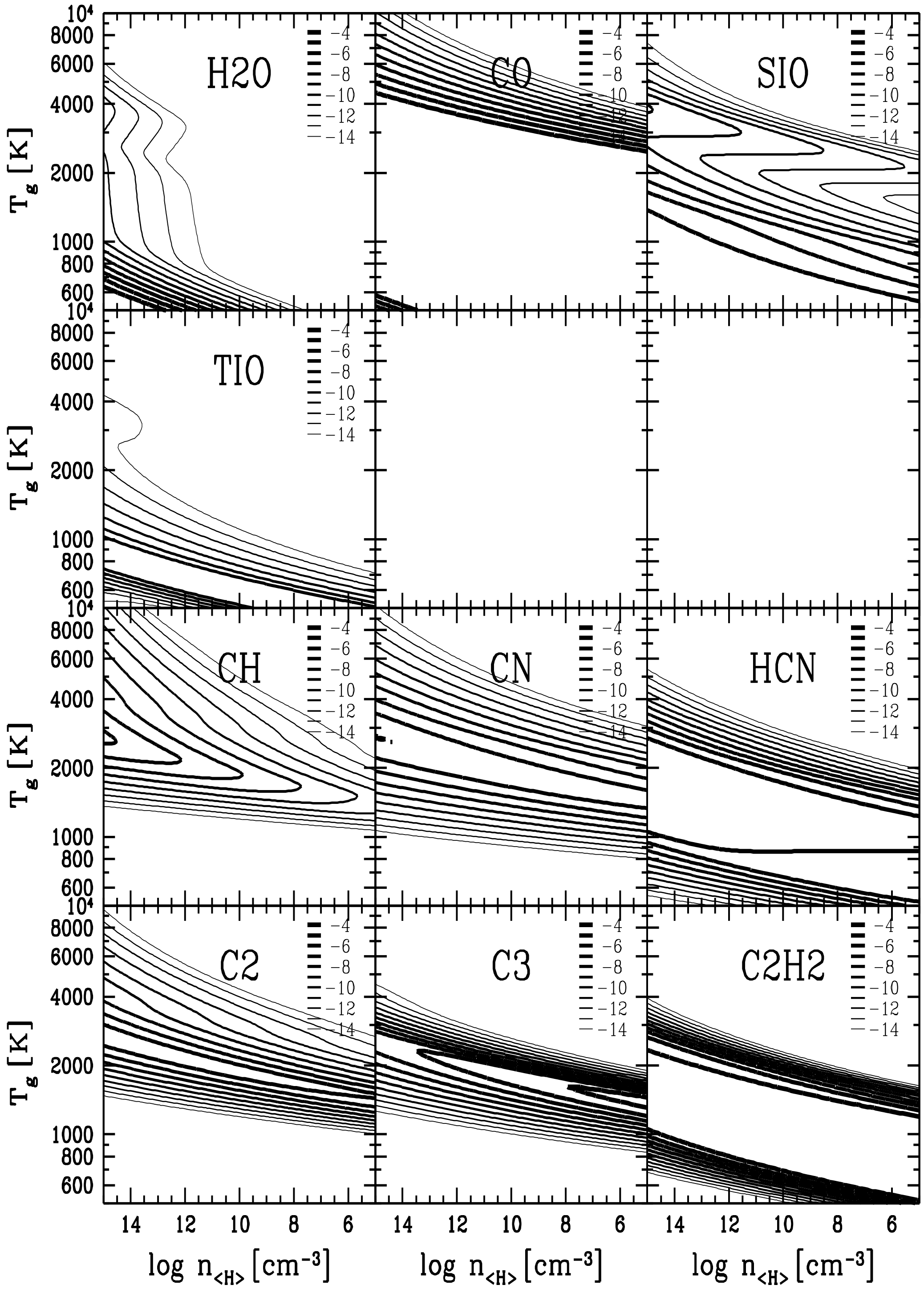

Figure 2.1: Logarithmic concentrations log $n_y/n_{<H>}$ of the line opacity carrying species relative to hydrogen in the carbon-rich case in chemical equilibrium (C/O=1.8).

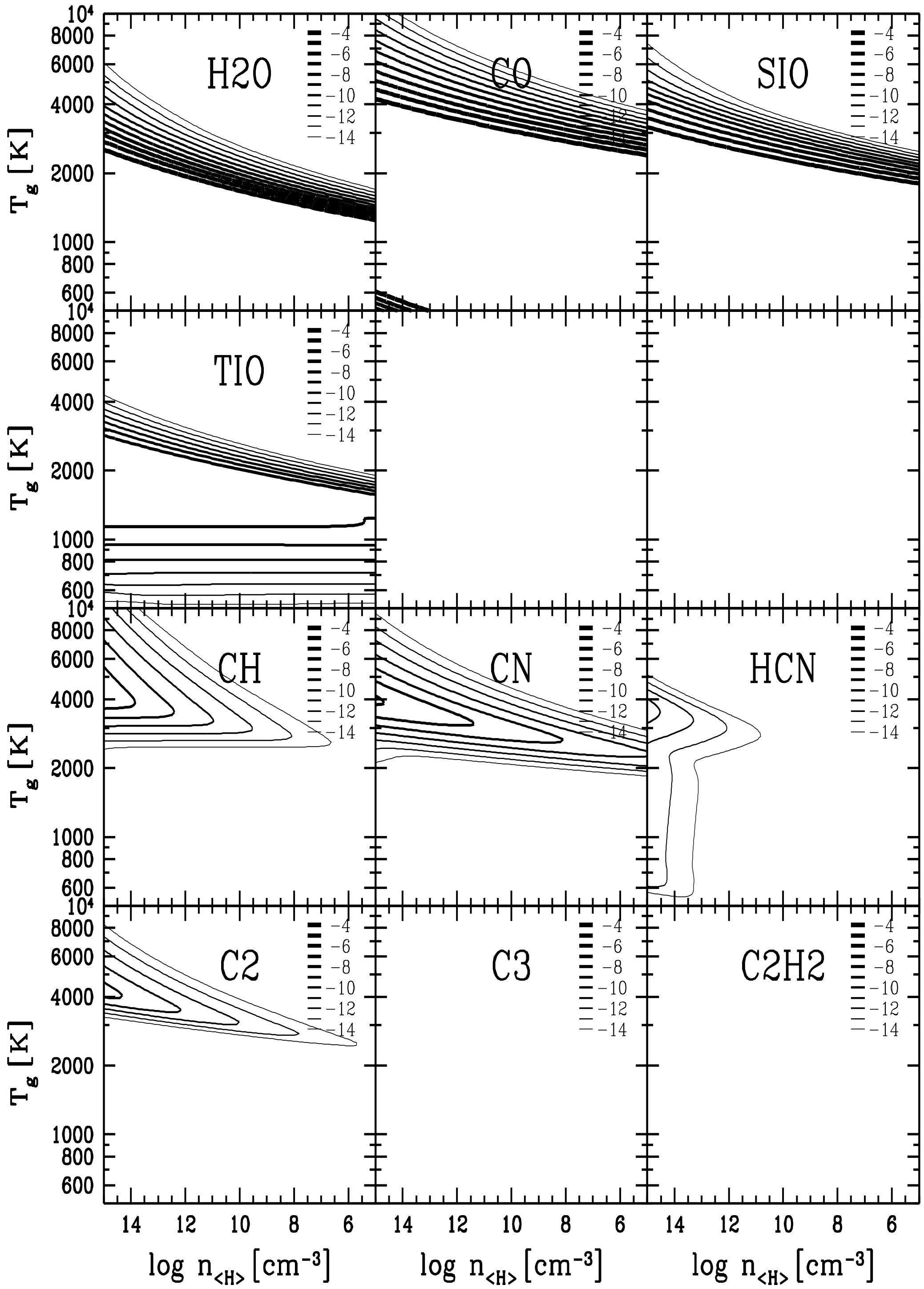

Figure 2.2: Logarithmic concentrations log $n_{\rm y}/n_{<{\rm H}>}$ of the line opacity carrying species relative to hydrogen in the oxygen-rich case in chemical equilibrium (C/O=0.43).

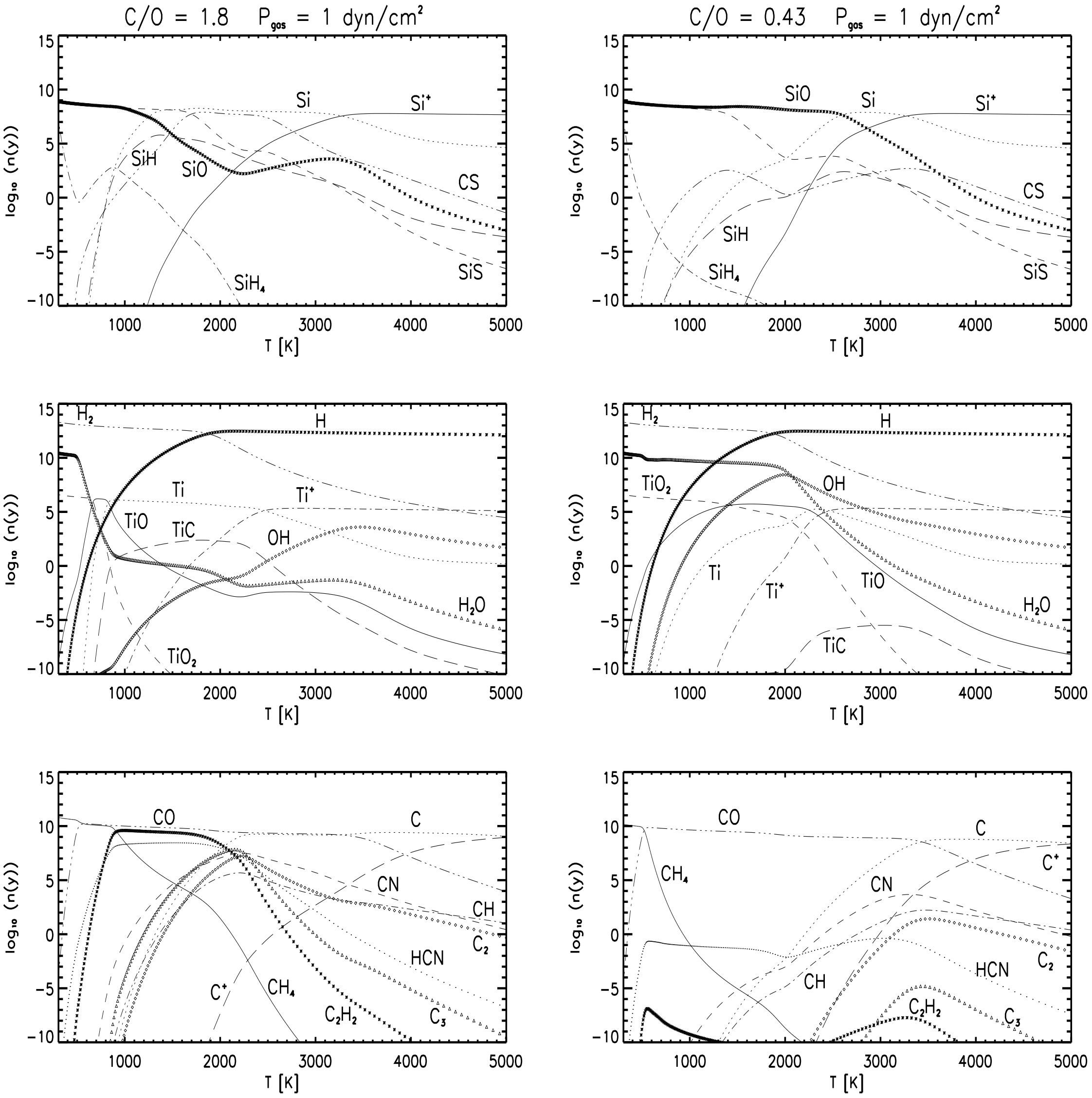

Figure 2.3: Total number densities $n(y) = n_{\mathrm{y}}$ for the line opacity species beside other abundant atoms, molecules and ions at $P_{\mathrm{gas}} = 1\,\mathrm{dyn/cm^2}$ for C/O = 1.8 (left column) and C/O = 0.43 (right column)[4]

• Silicon oxide SiO

Silicon oxide forms a strong plateau at temperatures lower than ≈ 3000K in the oxygen-rich case. This border shifts to ≈1500K in the carbon-rich case. Apart from SiO, SiS is abundant at low temperatures and silicon is mostly locked up into these two molecules at temperatures roughly below 3000K. At temperatures higher than about 3000K, silicon is mainly atomic unless it ionizes (see Fig. 2.3). Remarkable is the very high SiO number density at low temperatures ($T < 1000\,\mathrm{K}$) irrespective of the carbon-to-oxygen overabundance.

• Water H_2O

Gaseous water shows a similar behavior like SiO. It reaches a plateau of high number

[4] $10^6\ \mathrm{dyn/cm^2} = 1$ bar ; 1 atm = 1.013 bar = $1.013\,10^5$ Pa

density at $T \sim 2000$ K in the oxygen-rich case which slightly decreases with decreasing total hydrogen density. Such a plateau is also reached in the carbon-rich case, but at much lower temperatures, namely at $T \sim 600$ K. This temperature limit decreases with decreasing total hydrogen density. H_2O remains abundant down to ≈ 500 K for both cases and reaches a number density comparable to the most abundant carbon bearing species of about 10^{-4} relative to hydrogen. Towards higher temperatures, H_2O drops rapidly and e.g. OH is formed.

• CH, CN, C_2, C_3, HCN, C_2H_2

The number densities of CH, CN, C_2, C_3, HCN, and C_2H_2 depend very much on the carbon-to-oxygen ratio. All these molecules are abundant in the carbon-rich case. The polyatomic molecules C_3, HCN, and C_2H_2 reach number densities of about 10^{-4} relative to hydrogen which is 2-3 magnitudes larger than those of the two-atomic molecules CH, CN, and C_2 (except CO) in a carbon-rich equilibrium chemistry.

CH and CN are already present at almost the same high temperatures as CO in both case. HCN is moderate abundant at high temperatures and high densities also in the oxygen-rich case.

Note that singly ionized silicon and titanium (Si II, Ti II) influence the chemical equilibrium already at moderate temperatures; all the Si and Ti is ionized at $T > 2800$ K for $P_{\mathrm{gas}} = 1\,\mathrm{dyn/cm}^2$.

2.3 Conclusions

Summarizing the results of the chemical equilibrium computations, it is found that the line opacity species to be considered in this work are amongst the most abundant species. This is one of the reasons[5] why these molecules have been included as molecular opacity species in model atmosphere computations (cf. Table 3.3).

> Remarkable is that the O-bearing molecules SiO, H_2O, and TiO are abundant at low temperatures and high densities also in a carbon-rich environment.

Therefore, SiO, H_2O and TiO might also contribute to the total opacity at low temperatures in the carbon-rich case. In contrast, the contribution of the carbon bearing species to the total opacity in the oxygen-rich case will be negligible.

Considering the high abundances of SiS and CS, it might be worth including both molecules as line opacity species in the computations in further investigations.

[5]The other criterion is a large absorption coefficient of the molecule.

"Wenn Sie keine Materialgleichungen haben, brauchen Sie gar nicht erst anzufangen."
Wolfgang Muschik, May 1998

Chapter 3

Computation of line and continuum opacities

Late type giant stars exhibit complex line spectra which indicate strong interaction of radiation and matter. Molecules, which have been identified in such spectra, influence the thermodynamic structure of the atmosphere by line blanketing, blocking of the radiation emitted by the stellar interior, and by backwarming of the deeper atmospheric strata. A detailed description of such effects in stellar atmospheres requires a detailed knowledge of the possible radiative transitions of atoms, molecules, solids, and even of ions if hotter environments are considered.

Often, the amount of information available from quantum-mechanical calculations or laboratory experiments is too large (e.g. molecular line lists with data for about 10^6 bound–bound transitions) to be handled in physically complex calculations. Statistical methods are therefore applied which do not provide the quantity but ideally the quality of the desired information.

In statistical methods, one attempts to replace the complicated frequency variation of line opacities by a smaller number of frequency points. The most simple possibility is an average of the opacity over the whole frequency range of the spectrum (*mean opacity*).

Although it is known from many numerical experiments that cool star model atmospheres computed with mean opacities differ in any case largely from those computed with a detailed monochromatic opacity, mean opacities are still the most comprehensive and often the only applicable possibility for including molecular opacities in computations of physically complex systems like e.g. pulsating stars.

The idea of the *sampling methods* is either to average the opacity of a certain number of small frequency intervals instead over the whole spectral range (Tsuji 1994), or to take the opacity into account at a pre-chosen number of frequency points without any averaging process. The statistic character of the second variant of sampling methods is preserved because of the non–existence of any kind of correlation between the location of the sampling points and the location of the absorption lines in the spectrum. The two major sampling techniques are the *Opacity Distribution Function* (ODF) and the *Opacity Sampling* (OS) method, respectively. Both techniques (OS and ODF) produce, properly applied, nearly identical model atmospheres (see for example Ekberg et al. 1986), but difference lies in e.g. computational speed and flexibility in variation of model parameters.

The present chapter starts with an introduction to the theory of absorption coefficient calculation, and the theory about the OS method and mean opacities which both will be applied in this work. It follows an overview of the gaseous species considered as carriers of line and continuum opacity and scattering. The computed mean gas opacities will be compared to other works and to opacities of dust grains for carbon-rich and oxygen-rich environments.

3.1 Theoretical background – the opacity

The *opacity*, or the extinction coefficient $\chi(\boldsymbol{r}, t, \nu)$ at radial position $\boldsymbol{r}$, frequency ν and at time t describes the removal of energy from the radiation field by matter. One distinguishes between extinction by absorption, $\kappa(\boldsymbol{r}, \nu, t)$, and extinction by scattering, $\sigma(\boldsymbol{r}, t, \nu)$. The total opacity can be written as

$$\chi^{\mathrm{tot}}(\boldsymbol{r}, t, \nu) = \chi^{\mathrm{g}}(\boldsymbol{r}, t, \nu) + \chi^{\mathrm{d}}(\boldsymbol{r}, t, \nu) \tag{3.1}$$

with

$$\chi^{\mathrm{g}}(\boldsymbol{r}, t, \nu) = \kappa^{\mathrm{tot,g}}(\boldsymbol{r}, t, \nu) + \sigma^{\mathrm{tot,g}}(\boldsymbol{r}, t, \nu), \tag{3.2}$$

$$\chi^{\mathrm{d}}(\boldsymbol{r}, t, \nu) = \kappa^{\mathrm{tot,d}}(\boldsymbol{r}, t, \nu) + \sigma^{\mathrm{tot,d}}(\boldsymbol{r}, t, \nu). \tag{3.3}$$

g and d denote the extinction of the gaseous species and dust particles, respectively.

3.1.1 The gas absorption coefficient

The gas absorption coefficient $\kappa^{\mathrm{tot,g}}(\boldsymbol{r}, t, \nu)$ at any given frequency ν, radial position $\boldsymbol{r}$ and time t contains contributions from all possible transitions (bound-bound[1], bound-free[2], free-free[3]) of the gaseous species in the stellar atmosphere. For practical reasons, one distinguishes between continuum absorption $\kappa^{\mathrm{cont}}(\boldsymbol{r}, t, \nu)$ and the effect of individual spectral atomic and molecular lines, called line absorption, $\kappa^{\mathrm{line}}(\boldsymbol{r}, t, \nu)$,

$$\kappa^{\mathrm{tot,g}}(\boldsymbol{r}, t, \nu) = \kappa^{\mathrm{line}}(\boldsymbol{r}, t, \nu) + \kappa^{\mathrm{cont}}(\boldsymbol{r}, t, \nu). \tag{3.4}$$

The line absorption coefficient $\kappa^{\mathrm{line}}(\boldsymbol{r}, t, \nu)$ is the sum of all line absorption coefficients $\kappa^{\mathrm{line}}_{\nu,\mathrm{y}}(\boldsymbol{r}, t)$ of all absorbing species y in the gas phase contributing to the frequency ν

$$\kappa^{\mathrm{line}}(\boldsymbol{r}, t, \nu) = \sum_{\mathrm{y}} \kappa^{\mathrm{line}}_{\nu,\mathrm{y}}(\boldsymbol{r}, t). \tag{3.5}$$

$\kappa^{\mathrm{line}}_{\nu,\mathrm{y}}(\boldsymbol{r}, t)$ can be expressed (e.g. Mihalas 1978) by

$$\kappa^{\mathrm{line}}_{\nu,\mathrm{y}}(\boldsymbol{r}, t) = \sum_{l<u} \frac{h\nu_{lu}}{4\pi} \left[n_l B_{lu} \Phi_\nu^{lu} - n_u B_{ul} \Psi_\nu^{ul} \right], \tag{3.6}$$

[1] b-b: A photon is absorbed by an atom or a molecule resulting in a transition from one bound state to another (photoexitation).

[2] b-f: Due to photon absorption an electron escapes with a finite kinetic energy from an atom or molecule (photoionization).

[3] f-f: An electron moving in the electromagnetic field of an ion, atom or molecule absorbs a photon which alters the kinetic energy of the electron.

where $h\nu_{lu}/4\pi$ is the energy per solid angle removed from the radiation field by transitions from a lower (denoted with l) to an upper (denoted with u) state of an atom, ion or molecule. n_l and n_u are the occupation numbers (level populations) of the lower and upper transition state, respectively, h and k are the Planck and the Boltzmann constant. B_{lu} and B_{ul} are the Einstein coefficients for absorption and for stimulated emission. Φ_ν^{lu} is the absorption line profile, Ψ_ν^{ul} the emission line profile. ν is any frequency whereas ν_{lu} denotes the line center frequency. Assuming complete redistribution, i.e. assuming that the absorption and the emission process exhibit the same spectral distribution, yields $\Phi_\nu^{lu} = \Psi_\nu^{ul}$. In this work, local thermal equilibrium (LTE) is assumed and only in this case $\Phi_\nu^{lu} = \Psi_\nu^{ul}$ is valid (Mihalas 1978). In LTE, the occupation numbers are described by the Boltzmann distribution

$$\frac{n_u}{n_l} = \frac{g_u}{g_l}\, e^{-\frac{h\nu_{lu}}{kT}}, \tag{3.7}$$

where g_u and g_l denote the statistical weights of the upper and the lower transition state, respectively. The thermodynamical state of the matter in LTE is determined by two local thermodynamic quantities and, hence, one can obtain the gas absorption coefficient as function of T and ρ, i.e. $\kappa^{\mathrm{tot,g}}(\boldsymbol{r}, t, \nu) = \kappa_\nu^{\mathrm{tot}}(\rho(\boldsymbol{r}, t), T(\boldsymbol{r}, t)) = \kappa_\nu^{\mathrm{tot,g}}(\rho, T)$.

With these assumption and the relation $g_u B_{ul} = g_l B_{lu}$ one derives from Eq. (3.6) the absorption coefficient at frequency ν, temperature T and density ρ of the gaseous absorbing species y

$$\kappa_{\nu,\mathrm{y}}^{\mathrm{line}}(\rho, T) = \sum_{l<u} \frac{h\nu_{lu}}{4\pi} g_l B_{lu}\, \frac{\Phi_\nu^{lu} n_\mathrm{y}}{Z_\mathrm{y}(T)}\, e^{-\frac{E_l}{kT}} \left[1 - e^{-\frac{h\nu_{lu}}{kT}}\right]. \tag{3.8}$$

$n_\mathrm{y} = n_\mathrm{y}(\rho, T)$ is the number density of the absorbing species y, $Z_\mathrm{y}(T)$ is the partition function of the species y at temperature T

$$Z_\mathrm{y}(T) = \sum_l g_l e^{-\frac{E_l}{kT}}. \tag{3.9}$$

A possible pressure dependence of the partition function is neglected. E_l is the excitation energy from the ground state to the state of level l and ν_{lu} is the transition frequency. The factor $\left[1 - \exp(-\frac{h\nu_{lu}}{kT})\right]$ is referred to as the correction for stimulated emission which only occurs under the assumption of LTE. One extracts the line absorption cross section $\sigma_\nu^{\mathrm{abs,line}}$ from Eq. (3.8) by applying the relations

$$gf = \frac{m_\mathrm{e} c\, h\nu_{lu}}{4\pi^2 e^2}\, g_l B_{lu}, \tag{3.10}$$

and $\kappa_{\nu,\mathrm{y}}^{\mathrm{line}}(\rho, T) = \sigma_\nu^{\mathrm{abs,line}}(T)\, n_\mathrm{y}(\rho, T)$, and finds

$$\sigma_{\nu,\mathrm{y}}^{\mathrm{abs,line}}(T) = \frac{\pi\, e^2}{m_\mathrm{e} c}\, gf\, \frac{\Phi_\nu^{lu}}{Z_\mathrm{y}(T)}\, e^{-\frac{E_l}{kT}} \left[1 - e^{-\frac{h\nu_{lu}}{kT}}\right]. \tag{3.11}$$

The factor gf, called the gf-value, is the weighted oscillator strength, m_e the electron's mass, c the speed of light, and e the electron's charge.

It is possible to find similar expressions for the continuum cross sections $\sigma_{\nu,\mathrm{y}}^{\mathrm{abs,cont}}(T)$, one for each process (see Mihalas 1978, Allen 1973, or references given in

Table 3.2). They shall not be outlined here in further detail since the molecular line absorption processes are of special interest for this work.

In the frame of model atmosphere computations, line absorption cross sections are calculated from tabulated values of the transition frequency ν_{lu}, the excitation energies E_l, and the gf-values for each absorption species. In addition, the partition functions have to be known. They are available in form of tables, too, whereas the number densities n_{y} are computed assuming chemical equilibrium. The used line profile function Φ_ν^{lu} will be discussed in the next subsection.

3.1.1.1 The line profile function

In this work, the absorption line profile $\Phi_\nu^{lu} = \Phi_\nu$ is assumed to be a Gaussian profile

$$\Phi_\nu = \frac{1}{\sqrt{\pi}\Delta\nu_{\mathrm{D}}}\, e^{-\left(\frac{\nu-\nu_0}{\Delta\nu_{\mathrm{D}}}\right)^2} \tag{3.12}$$

with $\nu_0 = \nu_{lu}$ being the central line frequency (laboratory frequency), ν the frequency to be considered in the observers frame, and $\Delta\nu_{\mathrm{D}}^2 = (\nu_0^2/c^2)(v_{\mathrm{th}}^2 + v_{\mathrm{turb}}^2)$ the Doppler broadening (Lang 1992) being the frequency width due to thermal and micro-turbulence broadening. The thermal velocity can be calculated from $v_{\mathrm{th}} = \sqrt{2kT/m_{\mathrm{y}}}$ with m_{y} the mass of the molecular species y. v_{turb} is the micro-turbulence velocity which is usually introduced by observers to explain an otherwise unidentified line broadening effect.

•Line broadening

Assuming LTE, the applicability of the Gauss profile in the frame of opacity computations in moving media shall be evaluated by comparing typical values of the natural line broadening and the collisional line broadening to the Doppler broadening.

a) The *thermal line broadening (Doppler broadening)* for the example molecules CO, TiO, SiO, and C_2H_2 are computed from the respective thermal velocities for a temperature of 1000K:

CO	$v_{\mathrm{th}} = 0.77$km/s	$\Delta\nu_{\mathrm{D}}/\nu_0 = 2.57\ 10^{-6}$
TiO	$v_{\mathrm{th}} = 0.51$km/s	$\Delta\nu_{\mathrm{D}}/\nu_0 = 1.7\ 10^{-6}$
SiO	$v_{\mathrm{th}} = 0.61$km/s	$\Delta\nu_{\mathrm{D}}/\nu_0 = 2.05\ 10^{-6}$
C_2H_2	$v_{\mathrm{th}} = 0.79$km/s	$\Delta\nu_{\mathrm{D}}/\nu_0 = 2.66\ 10^{-6}$

The thermal line broadening is therefore of the order of $\Delta\nu_{\mathrm{D}}/\nu_0 \approx 10^{-6}$ if the turbulent velocity is neglected. If e.g. a turbulent velocity of $v_{\mathrm{turb}} = 2.5$ km/s is considered, the Doppler broadening is dominated by turbulent line broadening.

b) The *natural line broadening* $\Delta\nu_{\mathrm{nat}}$ can be estimated from the radiative life time τ_{rad} of an excitation state as $\Delta\nu_{\mathrm{nat}} = 1/\tau_{\mathrm{rad}}$. Measured life times of electronic and vibrational transitions are averaged values in most cases, and the average is taken over several rotational levels in one vibrational level (see Larsson 1983). For example, for CO, TiO, and SiO the following radiative life times for vibrational, electronic, and rotational transitions, respectively, can be found. The spectroscopic names of the example transitions ($n_u \rightarrow n_l$, $v_u \rightarrow v_l$, $j_u \rightarrow j_l$) are given in brackets behind the molecule's name. Data for TiO are taken from Hedgecook et al. (1995), for CO from Razig & Smirnov (1980), and for SiO from Langhoff & Bauschlicher (1993).

<u>CO:</u> $(X^1\Sigma^+ \rightarrow X^1\Sigma^+,\ 1{\rightarrow}0,\ j' \rightarrow j'')$
$\nu_{\rm vib} = 6.4\ 10^{13}{\rm s}^{-1}$ $\tau_{\rm rad,vib} = 0.03$ s $\Delta\nu_{\rm nat}/\nu = 5.18\ 10^{-13}$
<u>TiO:</u>$(f^1\Delta \rightarrow a^1\Delta,\ 0{\rightarrow}0,\ j' \rightarrow j'')$
$\nu_{\rm el} = 5.7\ 10^{14}{\rm s}^{-1}$ $\tau_{\rm rad,el} = 4.32\ 10^{-8}$ s $\Delta\nu_{\rm nat}/\nu = 4.03\ 10^{-8}$
<u>SiO:</u>$(X^1\Sigma^+ \rightarrow X^1\Sigma^+,\ 0{\rightarrow}0,\ 1{\rightarrow}0)$
$\nu_{\rm rot} = 4.49\ 10^{10}{\rm s}^{-1}$ $\tau_{\rm rad,rot} = 3.3\ 10^5$ s $\Delta\nu_{\rm nat}/\nu = 6.74\ 10^{-17}$
<u>SiO:</u> $(X^1\Sigma^+ \rightarrow X^1\Sigma^+,\ 0{\rightarrow}0,\ 100{\rightarrow}99)$
$\nu_{\rm rot} = 4.19\ 10^{12}{\rm s}^{-1}$ $\tau_{\rm rad,rot} = 0.25$ s $\Delta\nu_{\rm nat}/\nu = 9.53\ 10^{-13}$
<u>SiO:</u> $(X^1\Sigma^+ \rightarrow X^1\Sigma^+,\ 0{\rightarrow}0,\ 250{\rightarrow}249)$
$\nu_{\rm rot} = 8.99\ 10^{12}{\rm s}^{-1}$ $\tau_{\rm rad,rot} = 0.018$s $\Delta\nu_{\rm nat}/\nu = 6.1\ 10^{-12}$

The typical radiative life times of electronic transitions of molecules are $\tau_{\rm rad,el} \approx 10^{-8}$s, of vibrational transitions $\tau_{\rm rat,vib} \approx 0.01\ldots 1$s, and for rotational transitions $\tau_{\rm rat,rot} \approx 10^{-2}\ldots 10^6$s depending on the frequency.

c) The *collisional line broadening* is estimated by considering the typical time between two collisions : $\Delta\nu_{\rm col} = 1/\tau_{\rm col} = n\,\sigma_{\rm col} v_{\rm th}$ where n is the particle density of the collision partner ($n = n_{<{\rm H}>}$ being an upper limit) and $\sigma_{\rm col}$ the collisional cross section[4] which is for molecules typically $\sigma_{\rm col} \approx 10^{-15}{\rm cm}^2$.

line broadening	$\nu_{\rm el} \approx 10^{14}{\rm s}^{-1}$	$\nu_{\rm vib} \approx 10^{13}{\rm s}^{-1}$	$\nu_{\rm rot} \approx 10^9\ldots 10^{12}{\rm s}^{-1}$
thermal			
$\Delta\nu_{\rm D}/\nu_0$ ($v_{\rm turb} = 0$)	10^{-6}	10^{-6}	10^{-6}
$\Delta\nu_{\rm D}/\nu_0$ ($v_{\rm turb} = 2.5$km/s)	10^{-5}	10^{-5}	10^{-5}
natural			
$\Delta\nu_{\rm nat}/\nu_0$	10^{-8}	10^{-13}	$10^{-12}\ldots 10^{-17}$
collisional			
$\Delta\nu_{\rm col}/\nu_0$ at $n_{<{\rm H}>} = 10^6{\rm cm}^{-3}$	10^{-18}	10^{-17}	$10^{-13}\ldots 10^{-16}$
$\Delta\nu_{\rm col}/\nu_0$ at $n_{<{\rm H}>} = 10^{15}{\rm cm}^{-3}$	10^{-9}	10^{-8}	$10^{-4}\ldots 10^{-7}$

Table 3.1: Comparison of line broadening effects for typical electronic, vibrational and rotational frequencies.

Typical values for the relative line broadening $\Delta\nu/\nu_0$ are compared in Table 3.1. The estimations indicate that – in view of the approximations made – the thermal line broadening is by far the most important mechanism to be considered for line profile function. If turbulent velocity can not be neglected, the Doppler width $\Delta\nu_{\rm D}/\nu_0$ is at least one order of magnitudes larger than the width due to collision or due to the natural life time of an excited state at the low densities present in stellar atmospheres. An exception is collisional broadening for rotational transitions at high densities which might be larger than the Doppler broadening.

•Line-shift

The line-shift with respect to the rest position of an absorbing material moving with the velocity u (Doppler effect) is given by $\Delta\nu_0 = \nu_0\ u/c$.

[4] $\sigma_{\rm col}$ is approximated by a geometrical cross section $\sigma_{\rm col} = \pi\, a^2$ with $a \approx 2$Å.

If $\Delta\nu_0 = \Delta\nu_{\rm D,th}$ and $u = 20$km/s being the outflow velocity of a stellar wind,
∘ a line would be Doppler shifted by about $40\Delta\nu_{\rm D,th}$ from its original position ν_0 if the line broadening is mainly due to thermal line broadening with $v_{\rm th} \approx 0.5$km/s (TiO at 1000K) or
∘ a line would be shifted about $8\Delta\nu_{\rm D,turb}$ from its original position ν_0 for a turbulent medium with $v_{\rm turb} \approx 2.5$km/s.

This is a strong indication for the necessity of a treatment of the radiative transfer problem in a moving medium. Up to know, however, the radiative transfer for dust forming environments as well as for molecule dominated environments can be handled only in quasi-static approximation and no line-shifts due to velocity fields can be taken into account.

3.1.2 The scattering coefficient

The total scattering coefficient is calculated as the sum of scattering on bound and on free electrons

$$\sigma^{\rm tot}(\rho, T, \nu) = \sigma_{\rm R}^{\rm tot}(\rho, T, \nu) + \sigma_{\rm T}(\rho, T), \tag{3.13}$$

$\sigma_{\rm R}^{\rm tot}(\rho, T, \nu)$ being the total scattering coefficient for Rayleigh scattering and $\sigma_{\rm T}(\rho, T)$ denoting the Thomson scattering.

3.1.2.1 Rayleigh scattering

The total scattering coefficient for the scattering on bound electrons (Rayleigh scattering) is the sum over all scattering coefficients for all atoms and molecules, y, of concentration $n_{\rm y}$

$$\sigma_{\rm R}^{\rm tot}(\nu, \rho, T) = \sum_{\rm y} \sigma'_{\rm R,y}(\nu)\, n_{\rm y}. \tag{3.14}$$

The cross section for Rayleigh scattering $\sigma'_{\rm R,y}(\nu)$ is the cross section for radiation incident upon atoms or molecules whose characteristic transition frequency $\nu_0 = \nu_{lu}$ is much larger than ν and is given by

$$\sigma'_{\rm R}(\nu) = \frac{8\pi}{3}\left(\frac{e^2}{m_{\rm e}c^2}\right)^2 \frac{\nu^4}{(\nu^2 - \nu_0^2)^2}. \tag{3.15}$$

3.1.2.2 Thomson scattering

The scattering coefficient for scattering on free electrons is the cross section $\sigma'_{\rm T}$ for radiation incident upon free electrons e of concentration $n_{\rm e}$,

$$\sigma_{\rm T}(\rho, T) = \sigma'_{\rm T}\, n_{\rm e} \tag{3.16}$$

with

$$\sigma'_{\rm T} = \frac{8\pi}{3}\left(\frac{e^2}{m_{\rm e}c^2}\right)^2. \tag{3.17}$$

3.1.3 The dust absorption coefficient

The dust opacity $\chi^{\mathrm{d}}(\boldsymbol{r},t,\nu)$, i.e. the extinction coefficient of the dust component, is defined as

$$\chi^{\mathrm{d}}(\boldsymbol{r},t,\nu) = \pi \int_{a_l}^{\infty} a^2 Q^{\mathrm{ext}}(\nu,a) f(\boldsymbol{r},a,t)\, da \tag{3.18}$$

with $Q^{\mathrm{ext}}(\nu,a)$ the extinction efficiency of a grain of radius a which can be calculated from Mie theory assuming homogeneous spherical particles for a given complex refractory index. $f(\boldsymbol{r},a,t)$ is the local size distribution function at radius $\boldsymbol{r}$. In order to apply Mie theory, the grain size is restricted to $a > a_l$ with a_l being the lower limit size of the grains which are considered to have macroscopic properties.

If scattering is neglected, $\chi^{\mathrm{d}}_{\nu}(\boldsymbol{r},t) = \kappa^{\mathrm{d}}_{\nu}(\boldsymbol{r},t)$ and $Q^{\mathrm{abs}}(\nu,a) = Q^{\mathrm{ext}}(\nu,a)$, otherwise $Q^{\mathrm{abs}}(\nu,a) = Q^{\mathrm{ext}}(\nu,a) - Q^{\mathrm{scat}}(\nu,a)$. In the small particle limit (SPL) of Mie theory $Q^{\mathrm{ext}}(\nu,a) \sim a$ and one can define $Q'(\nu) = Q^{\mathrm{abs}}(\nu,a)/a$ such that for large wavelengths $\lambda \gg 2\pi\, a$ the dust opacity can be expressed by

$$\kappa^{\mathrm{d}}_{\nu}(\boldsymbol{r},t) = \pi\, Q'(\nu) \int_{a_l}^{\infty} a^3 f(\boldsymbol{r},a,t)\, da. \tag{3.19}$$

From the moment method developed by Gail & Sedlmayr (1988) follows that the third moment $K_3(\boldsymbol{r},t)$ (see Eq. (4.23)) of the local size distribution function $f(\boldsymbol{r},a,t)$ of the dust particles appear on the r.h.s. of Eq. (3.19), and it hence reads

$$\kappa^{\mathrm{d}}_{\nu}(\boldsymbol{r},t) = \pi\, Q'(\nu)\, a_0^3 K_3(\boldsymbol{r},t), \tag{3.20}$$

with a_0 being the hypothetical radius of the monomers forming the dust particles. $K_3(\boldsymbol{r},t)$ can be related to a degree of condensation f_c by

$$f_c = \frac{K_3(\boldsymbol{r},t)}{n_{\mathrm{cond}}}, \tag{3.21}$$

n_{cond} being the number density of condensible material in the gas phase.

3.2 Opacity computations

The absorption cross section $\sigma^{\mathrm{abs,line}}_{\nu,\mathrm{y}}(T)$ of a molecule y varies strongly with frequency (see Fig. 3.1) and a detailed description is almost impossible in the framework of model atmosphere computations. Therefore, some kind of opacity approximation is needed, and the opacity computation methods which are applied in this work will be outlined in the following.

3.2.1 Opacity sampling

In the opacity sampling method (OS) a sufficiently large number N of pre-chosen sampling points ν_{i}, ($\mathrm{i} = 1,\ldots,N$) is more or less randomly distributed in the frequency range of interest. The monochromatic absorption cross section $\sigma^{\mathrm{abs,line}}_{\nu,\mathrm{y}}(T)$ is computed from line lists containing for each transition the frequency (wavenumber or wavelength), the gf-value, the excitation energy, and - if necessary - the isotopic

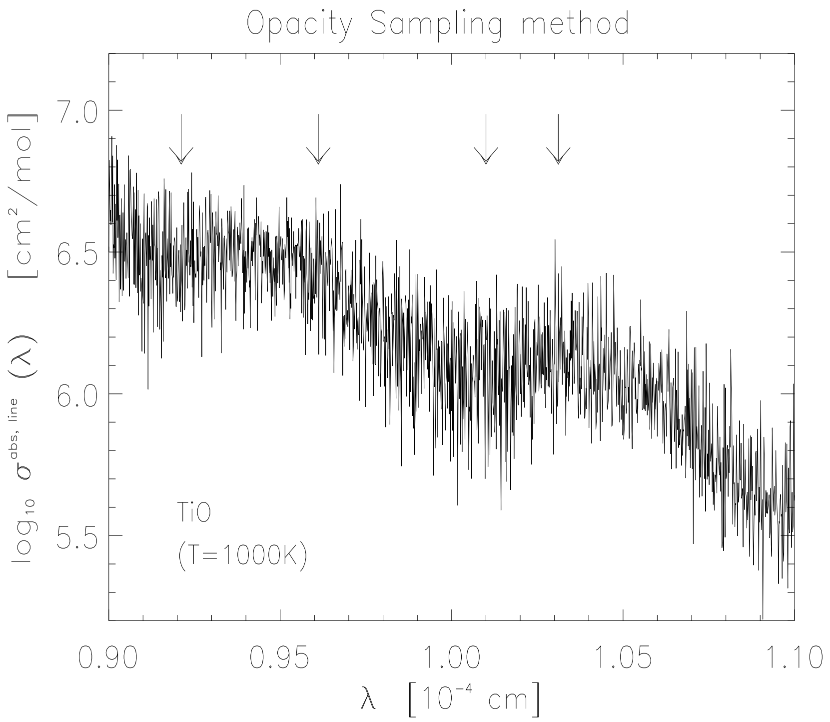

Figure 3.1: The opacity sampling method illustrated for the absorption cross section $\sigma_{\rm y}^{\rm abs,line}(T,\lambda)$ of TiO at $T = 1000$K in a wavelength interval of 0.2μm. The arrows indicate possible locations of sampling points in the wavelength space. Note that $\sigma_{\rm y}^{\rm abs,line}(T,\lambda)$ is given in cm^2 per mol.

shift[5]. The line profile is assumed to be a Gaussian with a contribution from a microturbulence velocity $v_{\rm turb} = 2.5\,$km/s. At each sampling point $\nu_{\rm i}$ the line contributions – which will be largest if the sampling point is close to the line center – are directly evaluated. Note that more than one line can contribute to one sampling point.

The sampling points where the line contributions may be evaluated are indicated by arrows in Fig. 3.1 where as an example the absorption cross section of TiO at $T = 1000$K is shown in a very small wavelength interval ($\Delta\lambda = 0.2\mu$m).

The total absorption coefficient $\kappa_\nu^{\rm tot,g}(\rho,T)$ of all the molecules considered at the sampling point $\nu_{\rm i}$ is an arithmetic sum of the opacity contribution of each species to that particular frequency (Eq. 3.5).

3.2.1.1 The distribution and number of sampling points

The statistical character of the variation of a complex absorption coefficient has to be well represented by the number of sampling points.

In static model atmosphere computations, which solve the full frequency dependent radiative transfer problem, distributions of approximately 5000 to 10 000 sampling points are applied. Such numbers result in very much alike atmospheric structures in models with equal stellar parameters.

The number of required points must be found by numerical experiments. Choosing a larger and larger number will lead to a "saturation" - above a certain number of

[5]Isotope shifts occur as a result of both nucleus mass and volume differences between isotopes.

sampling points, the resulting model atmosphere structure will no longer change by adding more sampling frequencies. Stellar atmosphere models calculated with fewer sampling points will asymptotically converge towards such an "ideal" model with increasing number of points.

It should be clear that a large number of ≈ 5000 sampling points is not applicable in dynamical models of stellar atmospheres and circumstellar envelops because the opacity has to be computed for each time step at each depth point (or radial position) and each frequency point (e.g. $10\,000 \times 512 \times 5000 \approx 10^{10}$ times). Therefore, investigations considering a reduced number of sampling points and respective errors were undertaken (Helling & Jørgensen 1998). It could be shown that already 20–50 sampling points can resemble a static atmosphere much better than any mean opacity. But still, the opacity computation would have to be carried out $10\,000\times512\times20 \approx 10^7$ times in a frequency-dependent dynamical models.

3.2.1.2 Opacity sampling in the model atmosphere code

One way of introducing opacity sampling in a model atmosphere program is to include explicitly a list containing either all the lines of interest or lines chosen by specific criteria at particular sampling points (Ekberg et al. 1986). The line list for each molecule is sampled separately and tables of the absorption cross section $\sigma_{\nu,y}^{\rm abs,line}(T)$ as function of frequency and temperature, and if necessary of microturbulence and pressure, are produced. When the radiative transfer program is executed, the absorption cross sections are interpolated in temperature (and microturbulence) and finally the total opacity of all the contributing molecules is calculated. It is sufficient to calculate the OS tables of the absorption coefficients once in order to use them also in further model calculations rather than to calculate them during every execution of the code.

3.2.2 Mean opacities

Mean opacities are used in a wide range of complex computations as in models of pulsating stars (e.g. Fleischer et al. 1995, Höffner et al. 1998) or models of stellar evolution (e.g. Carson et al. 1992, Schröder et al. 1998). Nevertheless, mean opacities are an approximation of the monochromatic opacity of the gas components of stellar atmospheres and envelopes in the frequency space.

3.2.2.1 Classical definition: Planck mean & Rosseland mean

•Planck mean
The Planck mean absorption coefficient is defined as

$$\kappa_{\rm Planck}(\rho, T) = \frac{\int_0^\infty \kappa_\nu(\rho, T) B_\nu(T)\, d\nu}{\int_0^\infty B_\nu(T)\, d\nu} \tag{3.22}$$

with $B_\nu(T)$ is the Planck function at frequency ν and temperature T.

According to this averaging process, the Planck mean gas absorption coefficient $\kappa^{\rm g}_{\rm Planck}(\rho, T)$ is dominated by the strong absorption lines. The respective dust mean can be written with Eq. (3.20) as

$$\kappa^{\mathrm{d}}_{\mathrm{Planck}}(\boldsymbol{r},t,T) = \pi\, a_0^3 K_3(\boldsymbol{r},t)\,\frac{\int_0^\infty Q'(\nu)\,B_\nu(T)\,d\nu}{\int_0^\infty B_\nu(T)\,d\nu} \tag{3.23}$$

$$= \pi\, a_0^3 K_3(\boldsymbol{r},t)\,Q'_{\mathrm{Planck}}(T), \tag{3.24}$$

$Q'_{\mathrm{Planck}}(T)$ being now the Planck mean absorption efficiency.

•Rosseland mean

The Rosseland mean opacity is defined as a reciprocal mean by

$$\chi_{\mathrm{Ross}}(\rho,T) = \left(\frac{\int_0^\infty \frac{1}{\chi_\nu(\rho,T)}\frac{\partial B_\nu(T)}{\partial T}d\nu}{\int_0^\infty \frac{\partial B_\nu(T)}{\partial T}d\nu}\right)^{-1}. \tag{3.25}$$

Due to the reciprocal process of averaging with the weighting function $\partial B_\nu(T)/\partial T$, the Rosseland mean gas opacity $\chi^g_{\mathrm{Ross}}(\rho,T)$ gives highest weight to continuum and weak absorption lines. If scattering is neglected the Rosseland mean dust opacity is

$$\kappa^{\mathrm{d}}_{\mathrm{Ross}}(\boldsymbol{r},t,T) = \pi\, a_0^3 K_3(\boldsymbol{r},t)\left(\frac{\int_0^\infty \frac{1}{Q'(\nu)}\frac{\partial B_\nu(T)}{\partial T}}{\int_0^\infty \frac{\partial B_\nu(T)}{\partial T}}\right)^{-1} \tag{3.26}$$

$$= \pi\, a_0^3 K_3(\boldsymbol{r},t)\,Q'_{\mathrm{Ross}}(T). \tag{3.27}$$

with $Q'_{\mathrm{Ross}}(T)$ being the Rosseland mean absorption efficiency.

3.2.3 Opacity species

Molecules like CO, CN, CH etc. are much less abundant than H_2 but have a much larger importance for the temperature structure of a cool stellar atmosphere since they have a much larger absorption cross sections in comparison to H_2 which is dipole inactive in the ground state. The same reason applies to N_2 although it is one of the most abundant molecules after CO in a solar like element composition.

3.2.3.1 Line opacity species

The CO line absorption is important in carbon-rich and in oxygen-rich atmospheres where CO occurs in equally high concentrations (compare Fig. 2.1 and 2.2). TiO, H_2O, and SiO are typically observed in oxygen-rich stars. CH, CN, C_2, C_3, HCN, and C_2H_2 are mainly responsible for the line opacity in carbon-rich stars; more complex molecules gaining importance with decreasing temperature.

In the following, those molecular line opacity species are summarized which are used in this work (compare also Sect. 2.2).

Isotopic line shifts are considered for the carbon bearing molecules concerning a prescribed $^{12}C/^{13}C$ ratio.

• Carbon monoxide CO

▷ Spectroscopically, carbon monoxide has a fundamental vibration-rotation band (1,0) between 4μm and 6μm with the center at 4.7μm. The first overtone (2,0) and the second

overtone (3,0) are observed at 2.3μm and at 1.5μm, respectively. Those bands are much weaker than the fundamental band (1,0).
◇ All three bands are included in the opacity data which base on absorption line data from Goorvitch (1994) adopted from Jørgensen (1996). The sampled data cover the wavelength range [1.5μm, 11μm].

• Titan monoxide TiO

▹ Titan monoxide has several electronic transitions between triplet and singlet states of 8 different electronic levels. The triplet system contains the red system (γ) ranging from 0.0214μm to 0.79μm, the blue-green system (α) ranging from 0.446μm to 0.6215μm, and the orange-red system ranging from 0.5849μm to 0.6629μm (γ'). The singlet system contains the orange system and two IR systems. The orange system is found between 0.559μm and 0.5733μm (β). The IR systems cover the ranges from 0.886μm to 0.9094μm (δ) , and from 1.0025μm to 1.1032μm (ϕ) (Pearse & Gaydon 1965). It was shown that TiO causes a significant heating in a stellar atmosphere (Jørgensen 1994a).
◇ The opacity data are based on a line list from Jørgensen (1994b) which includes the 7 electronic bands α, β, γ, $\gamma\prime$, ϵ, δ, and ϕ. The line list contains data for the 5 most abundant isotopes of ^{48}Ti^{16}O, ^{46}Ti^{16}O, ^{47}Ti^{16}O, ^{49}Ti^{16}O, and ^{50}Ti^{16}O ([6]) between $\approx$ 0.52μm and $\approx$ 1.1μm.

• Silicon monoxide SiO

▹ Silicon monoxide has important ro-vibrational bands of the $X^1\Sigma^+$ ground state in the mid IR part of the spectrum. Pure rotational radio frequencies and maser emission have also been observed.
◇The opacity data base on a line list from Langhoff & Bauschilder (1993) which includes the $X^1\Sigma^+$ ground state with its fundamental, first and second overtone transitions ($\nu = 0\ldots3$) ranging from [0.806μm, 2.45μm] and also data for the 3 isotopes ^{28}Si^{16}O, ^{29}Si^{16}O, and ^{30}Si^{16}O ([7]).

• Water H_2O

▹ Water has ro-vibrational transitions in the visible and IR part of the spectrum. The visible bands are very weak and band heads are not well defined in both spectral regions. Strong H_2O absorption occurs between 1.61μm and 1.78μm and between 1.3μm and 1.4μm.
◇ The opacity data are based on absorption line data from Jørgensen & Jensen (1993) which includes vibrational transitions of H_2O in its electronic ground state covering a wavelength range of about [0.34μm, 6.27μm].

• Methylidyne CH

▹ Three electronic transition systems are known from the spectroscopy of Methylidyne in regions of 0.43μm, 0.39μm and 0.3143μm and one vibrational-rotational band in the IR. The most pronounced spectral feature is the so-called G-band at $\approx$ 4300Å due to the 0–0 vibrational transition in the $A - X$ system.
◇ The opacity data are based on line data from Jørgensen et al. (1996) and include the 3 electronic ($A^2\Delta$–$X^2\Pi$, $B^2\Sigma^-$–$X^2\Pi$, $C^2\Sigma^+$–$X^2\Pi$) and one vibrational-rotational band ($X^2\Pi$–$X^2\Pi$). The line data cover the wavelength range [0.247μm, 11.05μm].

---

[6] The relative abundances of the isotopes are ^{46}Ti:^{47}Ti:^{48}Ti:^{49}Ti:^{50}Ti=0.08:0.073:0.738:0.055:0.054 (Jørgensen 1994b)

[7] The relative abundances of the isotopes are ^{28}Si:^{29}Si:^{30}Si=0.9223:0.0467:0.0310 (Aringer et al. 1997)

• Cyanide (Cyanogen) CN

▹ Cyanide has electronic transition bands in the violet and in the red part (which expands also into the UV) of the spectrum. The violet system has bandheads at 0.3590μm, 0.3883μm, and 0.4216μm which correspond to the (1,0), (0,0), and the (0,1) bands, respectively. The bandheads of the red systems are for the (1,0) band at 0.92μm, for the (0,0) band at 1.09μm, and for the (0,1) band at 1.41μm.
◇ The opacity data are based on a line list from Jørgensen & Larsson (1990) containing the data for the red system ($A^2\Pi$–$X^2\Sigma^+$) which is combined with the line list from Quercy et al. (1974) ranging now from $\left[2000\text{Å}, 3.003\mu\text{m}\right]$. The isotopic shift due to ^{12}CN and ^{13}CN is of minor importance of the total absorption coefficient (Jørgensen & Larsson 1990).

• Di-Carbon C_2

▹ In the blue-green-yellow part of the spectrum, the electronic transitions of the Swan system occurs with bandheads (1,0), (0,0), and (0,1) at 0.4737μm, 0.5165μm and 0.5635μm, respectively. The Phillips system with the electronic bands (1,0), (0,0), and (0,1) is located in the near IR. Its bandheads are at 1.01μm, 1.21μm, and 1.55μm, respectively. The third band system of C_2 are the Ballik-Ramsay bands with bandheads at 1.41μm, 1.77μm, and 2.5μm for the (1,0), (0,0), and the (0,1) bands, respectively.
◇ The opacity data base on data from Querci et al. (1974) (adopted from Jørgensen 1996) and the sampled data cover the wavelength range $[0.33\mu\text{m}, 14.5\mu\text{m}]$.

• Tri-Carbon C_3

▹ Tri-Carbon shows very rich absorption bands in the violet and the IR part of the spectrum. The strongest absorption is found between 0.38μm and 0.4μm. The so-called pseudo-continuum structure of the bands $^1\Sigma_u^-$–$\tilde{X}^1\Sigma_g^+$ (originated at 1890Å), $\tilde{A}^1\Pi_u$–$\tilde{X}^1\Sigma_g^+$ (at ≈ 4050Å), and the vibrational-rotational band system of the ground state (originating at $\approx 5.6\mu$m) makes its identification difficult.
◇ The opacity data base on a line list from Jørgensen et al. (1989) which contains data for the lowest 800 energy levels of C_3 in its ground state $^1\Sigma_g^+$ in a wavelength range of $[0.71\mu\text{m}, 7.5\mu\text{m}]$.

• Hydrogen cyanide HCN, Ethyne (Acethylen) C_2H_2

▹ Both molecules show strong ro-vibration absorption bands in the IR. A series of overlapping bands can be identified between 0.75μm and 13μm. Intense bands are identified at 3.1μm, 7.1μm, and 12.5μm. The 110–000 combination band of HCN at 3.56μm is important for the study of upper atmospheres as this spectral region has a well defined continuum.
◇ The opacity data for HCN and C_2H_2 are based on line lists from Jørgensen (1990). The HCN and the C_2H_2 line lists include combination band systems.

3.2.3.2 Continuum opacity species

The *continuum opacity* $\kappa_\nu^{\text{cont}}(\rho, T)$ accounts for the gross features in the energy distribution of the emergent spectrum of a star. It arises from bound-free or free-free transitions. The most important contributors to the continuum opacity are neutral (H I) and negative charged (H^-) hydrogen. In addition, the bound-free and free-free absorption of He I and He II, heavier elements (C I, Mg I, Al I, Si I) are taken into account. The continuum opacity is only a weak function of frequency compared to the line opacity.

The contribution of the continuum opacities are considered in the wavelength

species	b-f/f-f	Reaction	reference
HI	b-f	$H + h\nu \rightarrow H^+ + e^-$	Karzas & Latter (1961)
HI	f-f	$H^+ + e^- + h\nu \rightarrow H^+ + e^-$	
H^-	b-f	$H^- + h\nu \rightarrow H + e^-$	John (1988)
	f-f	$H + e^- + h\nu \rightarrow H + e^-$	
H+H	b-f	$H + H + h\nu \rightarrow H^+ + e^- + H$	Doyle (1968)
H_2^-	f-f	$H_2 + e^- + h\nu \rightarrow H_2 + e^-$	Somerville (1964)
H_2^+	b-f	$H_2^+ + h\nu \rightarrow H + H^+$	Mihalas (1965)
HeI	b-f	$He + h\nu \rightarrow He^+ + e^-$	Peach (1970)
	f-f	$He^+ + e^- + h\nu \rightarrow He^+ + e^-$	
He^-	f-f	$He + e^- + h\nu \rightarrow He + e^-$	Carbon et al. (1969)
CI	b-f	$C + h\nu \rightarrow C^+ + e^-$	Peach (1970)
	f-f	$C^+ + e^- + h\nu \rightarrow C^+ + e^-$	
MgI	b-f	$Mg + h\nu \rightarrow Mg^+ + e^-$	Peach (1970)
	f-f	$Mg^+ + e^- + h\nu \rightarrow Mg^+ + e^-$	
AlI	b-f	$Al + h\nu \rightarrow Al^+ + e^-$	Peach (1970)
	f-f	$Al^+ + e^- + h\nu \rightarrow Al^+ + e^-$	
SiI	b-f	$Si + h\nu \rightarrow Si^+ + e^-$	Peach (1970)
	f-f	$Si^+ + e^- + h\nu \rightarrow Si^+ + e^-$	

Table 3.2: Continuum opacity processes in absorption

range $[0.125\mu\mathrm{m}, 25\mu\mathrm{m}]$. The respective reactions and references are summarized in Tab. 3.2.

3.2.3.3 Scattering

In addition to the continuum opacity, scattering by fee electrons (Thomson scattering) and scattering by bound electrons (Rayleigh scattering) for HI and HeI was taken into account (Dalgarno 1962).

3.2.4 Numerical approach

The local opacities are computed as function of wavenumber $\tilde{\nu}$, the total hydrogen density $n_{<\mathrm{H}>}$ and temperature T assuming LTE and chemical equilibrium. In addition, the medium is assumed to be static (no line-shifts) and only thermal and microturbulent line broadening is taken into account. The elemental abundances ϵ_{i} are kept constant except for ϵ_{C}.

The opacity program is based on parts of the MARCS model atmosphere code (Gustafsson et al. 1975, Jørgensen et al. 1992)[8] in the version of Helling & Jørgensen (1998) and has been combined with a new equilibrium chemistry routine. The data of the pressure equilibrium constants have been updated and those of several additional atomic ions have been included. The program was extended to mean gas opacity computations.

The necessary entries for the opacity program are

[8]MARCS is a hydrostatic model atmosphere code which handles the complete frequency dependent radiative transfer problem together with convection including molecular line absorption, continuum absorption and scattering.

- input parameters
  ⊢ gas temperature T [K]
  ⊢ total hydrogen density $n_{<\mathrm{H}>}$ [cm^{-3}]
  ⊢ elemental abundances ϵ_{i}
  ⊢ carbon-to-oxygen ratio C/O
  ⊢ isotopic ratios
  ⊢ wavenumber $\tilde{\nu}$ [cm^{-1}]
  ⊢ microturbulence velocity $v_{\mathrm{turb}} = 2.5\,\mathrm{km/s}$

- input data
  ⊢ data for absorption cross sections $\sigma_{\nu,y}^{\mathrm{abs,line}}(T)$ [cm^2/mol]
  The absorption cross sections are available in tabulated form for each opacity species at every sampling point wavenumber and temperature. These tables were obtained by applying the OS method to line lists for each molecule on a wavenumber grid of 5 363 sampling points.
  ⊢ data for the partition functions $Z_y(T)$
  ⊢ data for the pressure equilibrium constants $K_p(T)$

3.3 Results of gas mean gas opacities

As a first step, tables of carbon- and oxygen-rich Rosseland mean gas opacities and Planck mean gas opacities on the basis of the Opacity Sampling method are calculated for solar element composition, for the elemental abundances of the Large Magellanic Cloud (LMC) and the Small Magellanic Cloud (SMC).

Rosseland mean and Planck mean gas opacities (Eqs. 3.22[9], 3.25) were computed for a 101×101 grid of $T\epsilon$ [500K, 10000K] and $n_{<\mathrm{H}>}\epsilon$ [$10^5\,\mathrm{cm}^{-3}$, $10^{15}\,\mathrm{cm}^{-3}$]. The gas was assumed to have solar elemental abundances or LMC or SMC abundances where the carbon abundance ϵ_{C} was treated as an additional free parameter that either C/O=1.8 or C/O=0.43. The mean gas opacities are computed per mass density; $\chi_{\mathrm{Ross}}/\rho$ and $\kappa_{\mathrm{Planck}}/\rho$ in [cm^2/g].

The mean gas opacities decrease towards low temperatures unless the temperature is so low that molecules are present. Since molecules are not present at high temperatures, the main contributions at $T > 6000\,\mathrm{K}$ come from the continuum species for both kinds of mean gas opacities.

In an intermediate temperature range ($\approx 3000\,\mathrm{K} \leq T \leq \approx 1500\,\mathrm{K}$ depending on the density), the increasing number densities of molecular opacity species cause an increase in both mean gas opacities. But at $T < 1500\,\mathrm{K}$ the number densities of most of the line opacity molecules decrease again. Instead, more complex molecules like CH_4 or C_6H_6 are present. The contribution at the lowest temperatures come mainly from H_2^- (f-f) continuum absorption and CO (but also SiO, H_2O) for carbon-rich chemistry and from H_2^- (f-f) and SiO and H_2O in oxygen-rich chemistry.

The overall structure of both means is characterized by the interplay between continuum opacities and the molecular line opacities. The Planck mean gas opacities are always larger than the Rosseland mean by at least 1 order of magnitude for the same T and $n_{<\mathrm{H}>}$ if the line opacity is dominant. This difference increases towards low

[9] including scattering

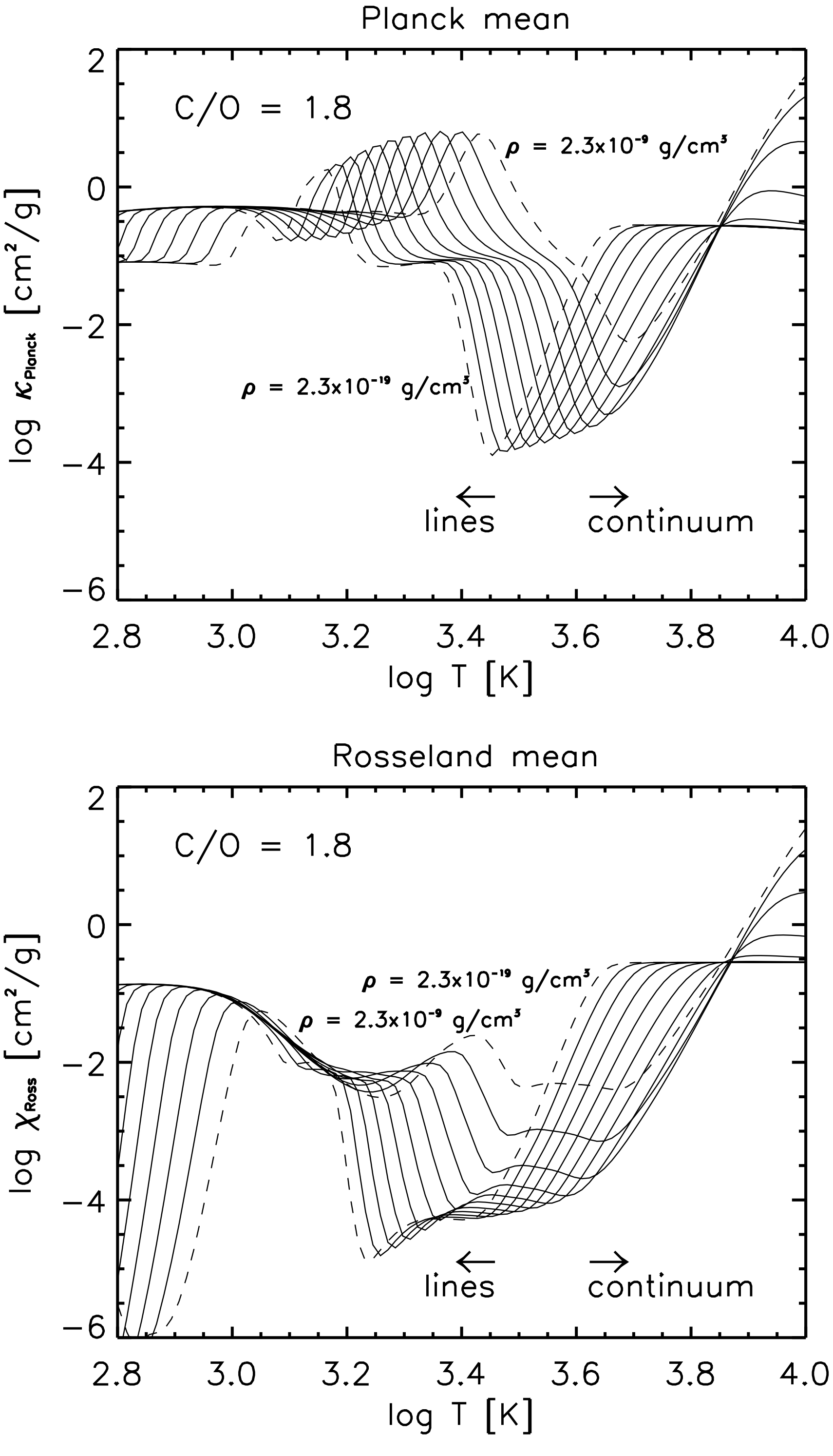

Figure 3.2: Carbon-rich Planck mean (upper panel) and Rosseland mean (lower panel) gas opacities as function of temperature T [K] and density ρ [g/cm^3] ($n_{<\mathrm{H}>} = 10^5 \ldots 10^{15}\mathrm{cm}^{-3}$) for solar metalicity. The dashed curves indicate the mean gas opacities at smallest ($\rho = 2.3\,10^{-19}\,\mathrm{g/cm^3}$) and largest ($\rho = 2.3\,10^{-9}\,\mathrm{g/cm^3}$) density. The arrows denote the temperature range where line or continuum absorption plays the most important role.

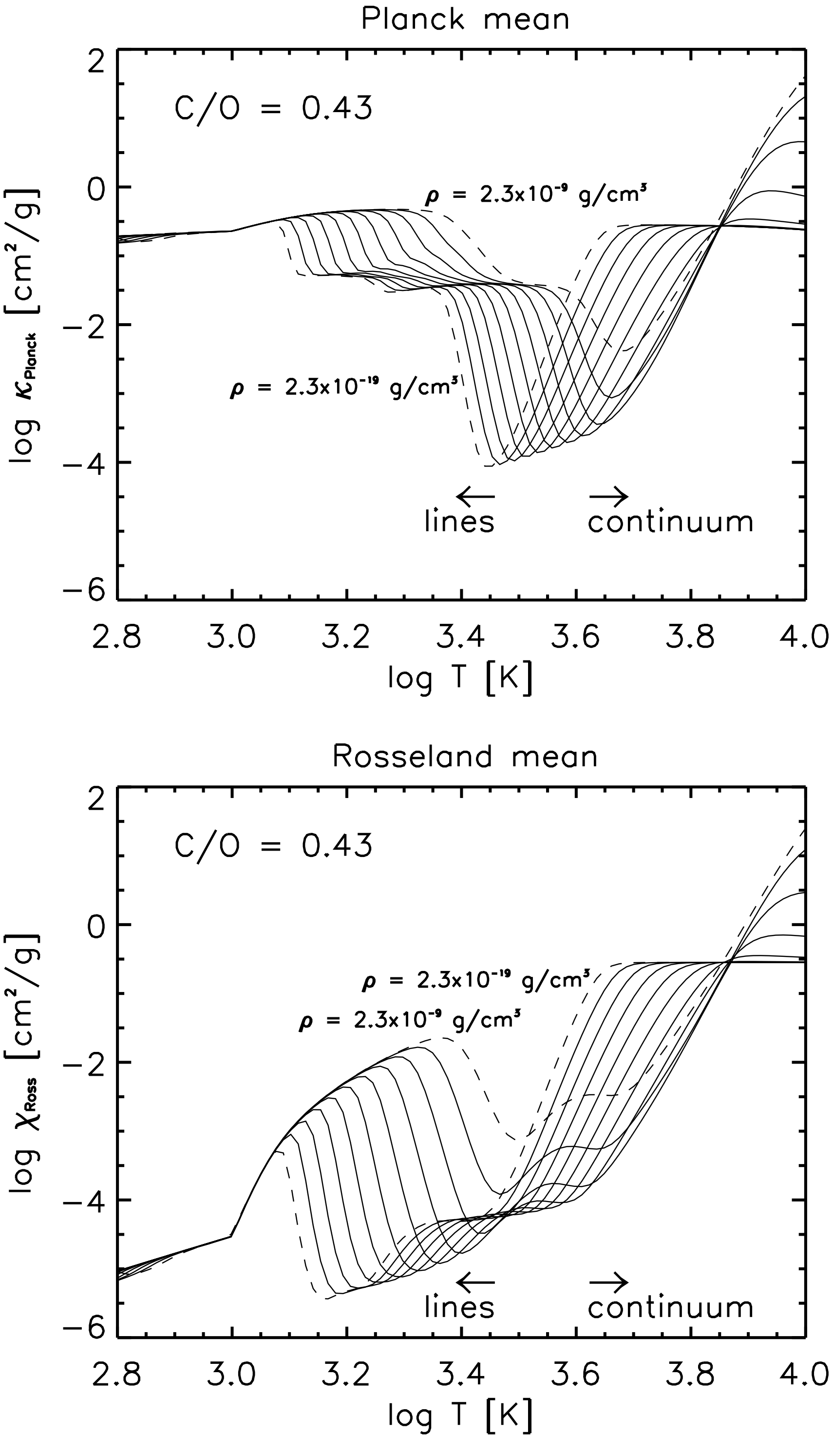

Figure 3.3: Oxygen-rich Planck mean (upper panel) and Rosseland mean (lower panel) gas opacities as function of temperature T [K] and density ρ [g/cm^3] ($n_{<\mathrm{H}>} = 10^5 \ldots 10^{15}\mathrm{cm}^{-3}$) for solar metalicity. The dashed curves indicate the mean gas opacities at smallest ($\rho = 2.3\,10^{-19}\,\mathrm{g/cm^3}$) and largest ($\rho = 2.3\,10^{-9}\,\mathrm{g/cm^3}$) density. The arrows denote the temperature range where line or continuum absorption plays the most important role.

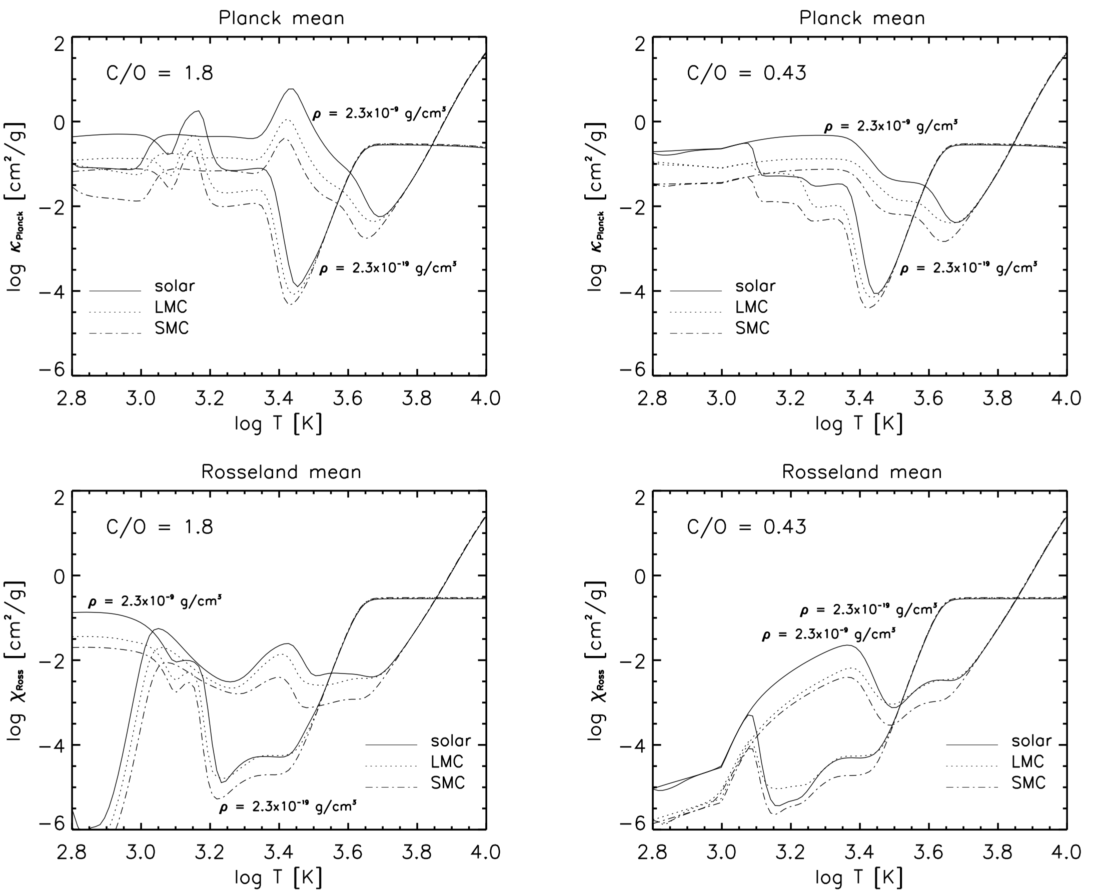

Figure 3.4: Comparison of mean gas opacities for different metalicity: solar, LMC, and SMC (Table 2.1) for $T \epsilon [630\mathrm{K}, 10\,000\mathrm{K}]$ and two exemplary densities. Indicated are opacities at the smallest ($\rho = 2.3\,10^{-19}\,\mathrm{g/cm^3}$) and at the largest ($\rho = 2.3\,10^{-9}\,\mathrm{g/cm^3}$) density: solid line - solar, doted line - LMC, dashed line - SMC.
Left: carbon-rich (C/O=1.8) Right: oxygen-rich (C/O=0.43)

temperatures. The reason for this behavior lies within the nature of the averaging processes: while the Planck mean is dominated by strong absorption lines of the molecules, the Rosseland mean is dominated by weak absorption. The continuum prevents the Rosseland mean to become zero because it is present at all frequencies considered.

The numerical process of averaging brings another question into play: the interval borders for the frequency integration. Usually, the data available dictate the frequency range considered while in theory the range goes from 0 to ∞.

With regard to the discussion of important opacity species to be taken into account, Rosseland mean and Planck mean gas opacities were re-computed for an carbon-rich chemistry (C/O=1.8) without the oxygen bearing opacity species TiO, SiO and H_2O. The same was done for oxygen-rich chemistry without CH, CN, C_2, C_3, C_2H_2, and HCN.

TiO, SiO and H_2O (or CH, CN, C_2, C_3, C_2H_2, and HCN in the oxygen-rich case) should not have any influence on the mean (or total) opacity in a carbon-rich gas as long as the oxygen is looked in carbon monoxyd CO. But if CO is destroyed, the now available oxygen causes an increase of the number density of TiO, SiO and H_2O (see left column, Fig. 2.3) at low temperatures in the carbon-rich case.

The missing oxygen containing opacities do not affect the carbon-rich mean opacity species over a wide temperature range. Only at low temperatures $T < 1000\,\mathrm{K}$ were the TiO, SiO and H_2O concentrations increase but those of di-atomic carbon molecules decrease, a noticeable difference of about half a magnitude occurs for the Planck mean gas opacities. The effect is independent of the gas density and occurs at almost the same temperature (about $T < 1000\,\mathrm{K}$) corresponding to the temperature where the CO density decreases. This effect is negligible for Rosseland mean gas opacities as they are determined by the continuum and the weak line opacity.

The neglect of CH, CN, C_2, C_3, C_2H_2, and HCN does not influence the oxygen-rich mean gas opacities in the investigated parameter range because the available carbon which no longer bound in CO causes an strongly increasing number density of CH_4 (right column, Fig. 2.3) which is not included as opacity species here.

The comparison of mean gas opacities for solar, LMC and SMC elemental abundances (see Table 2.1) is depicted in Fig. 3.4. The mean gas opacities for the SMC have the largest difference to the solar mean gas opacities, because the elemental abundances deviate at most. The large similarity at high temperatures is caused by the very similar elemental abundances of the main continuum absorption species He and H.
One further notes that the Rosseland mean opacities of the LMC show a better agreement with the solar mean gas opacities at lower temperature than the Rosseland mean gas opacities of the SMC. The reason is the good agreement of the solar and the LMC elemental abundances of the continuum species Mg (Al and K were assumed to be solar) beside H and He. Also the LMC element abundances of Si, O, and C are much closer to the solar values than the SMC abundances.

3.4 Comparison to other mean gas opacity computations

In the following, comparisons to other works considering mean gas opacities will be shown. In the literature, comparisons for Rosseland mean gas opacities at $T > 4000\,\mathrm{K}$ can be found in e.g. Neuforge (1993), other comparisons down to 1000 K have been shown by Alexander & Ferguson (1994).

The results of this work are compared to:

a) oxygen-rich Rosseland mean and Planck mean gas opacities from the Opacity Project (e.g. Seaton et al. 1994)
b) carbon-rich Rosseland mean gas opacities and Planck mean gas opacities from Sharp (1992)
c) carbon-rich and oxygen-rich Rosseland mean gas opacities from Scholz & Tsuji (1984)
d) carbon-rich and oxygen-rich Rosseland mean gas opacities and Planck mean gas opacities from Höfner (1997)
e) oxygen-rich Rosseland mean gas opacities and Planck mean gas opacities from Ohnaka & Tsuji (1998).

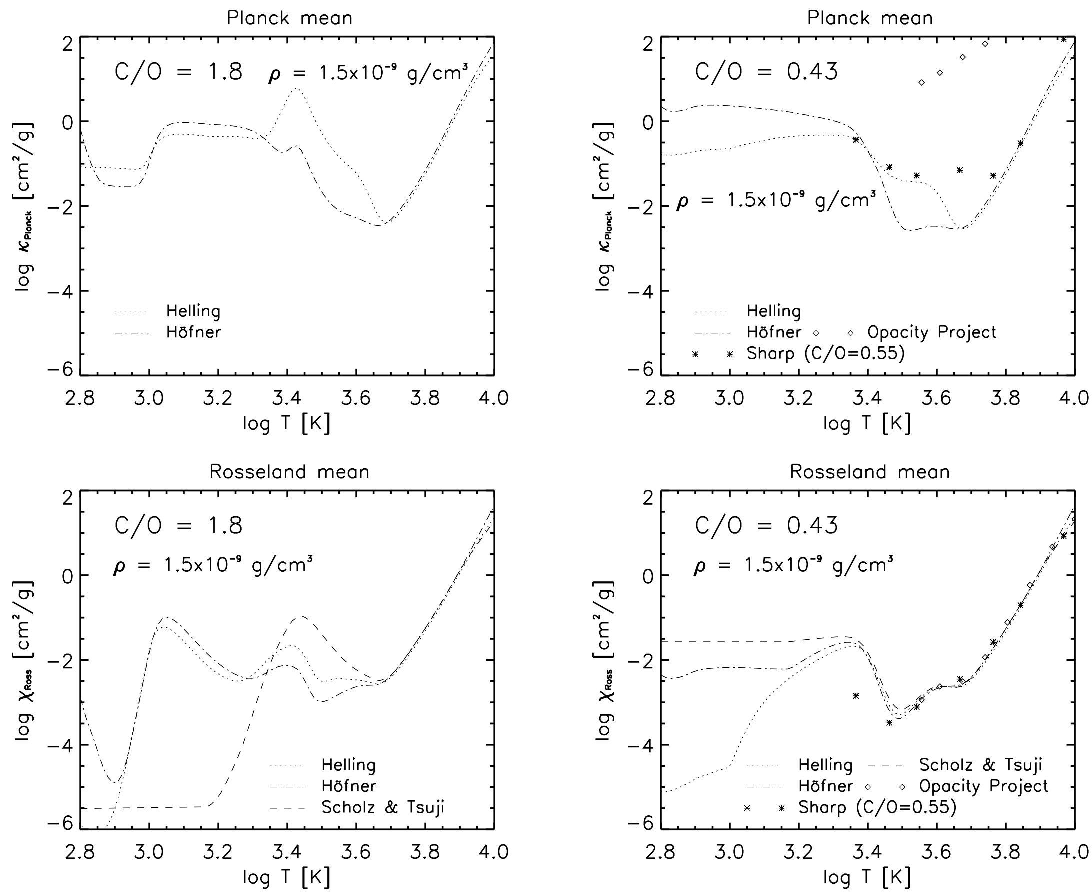

Figure 3.5: Comparison of mean gas opacities from different authors for $T \,\epsilon\, [630\mathrm{K}, 10\,000\mathrm{K}]$ and $\rho = 1.5\,10^{-9}\mathrm{g/cm^3}$: diamonds - Opacity Project, asterisks - Sharp (1992), dashed line - Scholz & Tsuji (1984), dash dot line - Höfner (1997), dotted line - this work.
Left: carbon-rich (C/O = 1.8) Right: oxygen-rich (C/O = 0.43)

The works **a)** – **e)** including some details about the opacity sources and elemental abundances used are summarized in Table 3.3.

The Rosseland mean and the Planck mean gas opacities shown in Fig. 3.5 agree well in the high temperature range ($T > 3500\,\mathrm{K}$). Only the high temperature Planck mean gas opacities from the Opacity Project (diamonds in the right panel, Fig. 3.5) show much higher values than all others. This is confirmed by Neuforge (1993) and Alexander & Ferguson (1994) who show the good agreement among the different compilations of Rosseland mean gas opacities for $T > 4000\,\mathrm{K}$. At lower temperatures larger deviations occur among the various workers. Also Alexander & Ferguson (1994) found severe deviations starting at $\approx 2500\,\mathrm{K}$ towards lower temperatures (see their Fig. 16b).

a) The Opacity Project (OP) was designed for mainly computing Rosseland mean and Planck mean gas opacities for temperatures higher than 3100K. Therefore, comparisons to mean gas opacities of the present work only make sense in the temperature range where continuum opacities are most important. Since this work includes considerably less continuum opacity sources and no atomic line opacity, the OP Planck mean gas opacities are considerably larger while the Rosseland mean compare very well because it is much less sensitive to strong absorption. This is depicted in Fig. 3.5.

b) Large deviations occur for the oxygen-rich Planck mean opacities from Sharp (1992) (asterisks in the right upper panel, Fig. 3.5) whereas the oxygen-rich Rosseland mean gas opacities compare well. These deviations occur in a range where also the Opacity Project shows large differences to the opacities computed in this work. Both sources have a large amount of atomic and ionic opacity species included. On the contrary, the oxygen-rich Rosseland mean gas opacities from Sharp (1992) are smaller at temperatures $T < 2800\,\mathrm{K}$. Also Alexander et al. (1994) noticed this effect and reasoned it by an underestimation of the contribution of water vapor to the Rosseland mean due to the use of an incomplete H_2O line list by Sharp (1992) (see Jørgensen 1994a for the importance of weak lines).

c) Comparison with Rosseland mean gas opacities from Scholz & Tsuji (1984) (dashed line, Fig. 3.5) shows a good agreement in the oxygen-rich case in the temperature range (1580K $< T <$10.000K) covered by their table. In the carbon-rich case large differences occur. The slightly different C/O ratio can only partly explain the large deviations in the carbon-rich case. One reason could be the additional opacity species SiH, MgH, and CaH used by them. SiH is as high abundant in the carbon-rich case as TiO is in the oxygen-rich case but the SiH particle density decreases by orders of magnitudes in the carbon-rich case where Si is mainly bound in SiO (see Fig. 2.3). The MgH particle density does not change with C/O (not shown in Fig. 2.3), and CaH is even less abundant than MgH. Therefore, if different molecular line species are the reason for the differences between our mean gas opacities and those from Scholz & Tsuji (1984), then it is most likely due to SiH as missing opacity source in our data. A further difference is that the Rosseland mean gas opacities from Scholz & Tsuji (1984) are computed by weighted reciprocal means of pre-computed straight mean gas opacities. Alexander et al. (1994) compares Rosseland mean gas opacities from Allard et al. (1994) which also were computed from pre-computed straight mean gas opacities (their Fig. 16a). There, only slight deviations occur at temperatures $T > 2500\,\mathrm{K}$. Therefore, the differences seen between the Rosseland mean gas opacities from Scholz & Tsuji (1984) and ours is likely caused by the missing SiH since it is a very high abundant species.

d) Comparison with Höfner (1997) shows almost identical Planck and Rosseland gas mean opacities for $T > 3000\,\mathrm{K}$, i.e. at high temperatures where molecular line opacities have no large influence on the total opacity. Although a good trend similarity can be observed from Fig. 3.5 at all temperatures, deviations are obvious and can not stem from different opacity species or different data included as they are the same (see Tab. 3.3). It is very likely that those differences in the mean opacities are due to differences in thermo-chemical data as such data are of crucial importance for the sensitive balance among the molecules in chemical equilibrium.

e) A very good agreement of the gas opacities of this work with the mean gas opacities from Ohnaka & Tsuji (1998) (asterisks and diamonds, Fig. 3.6) is found for oxygen-rich case. The good agreement is not surprising as the opacity data used by Ohnaka & Tsuji (1998) are basically the same as those used by Scholz & Tsuji (1992) but extended over a larger temperature range. The tendency of decreasing Rosseland

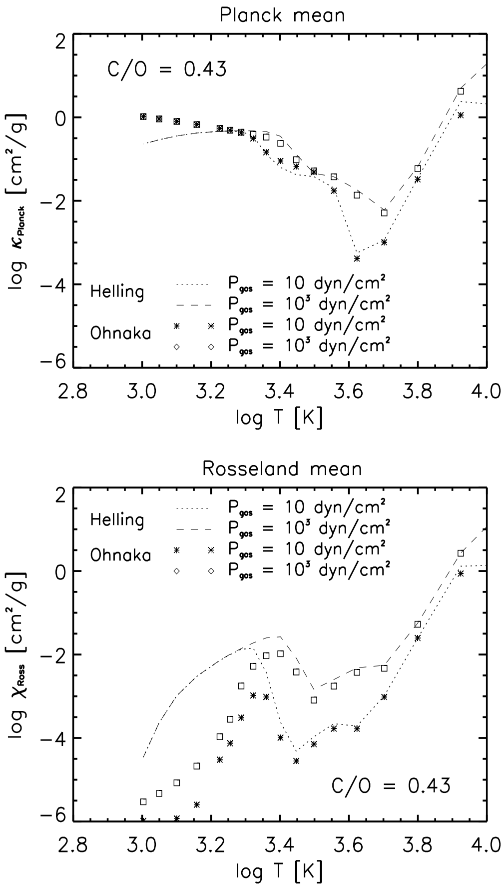

Figure 3.6: Comparison to mean gas opacities adopted from Ohnaka & Tsuji (1998) (squares and asterisks) for C/O = 0.43 for $T \epsilon [630\mathrm{K}, 10\,000\mathrm{K}]$, $P_{\mathrm{gas}} = 10\,\mathrm{dyn/cm}^2$ and $P_{\mathrm{gas}} = 10^3\,\mathrm{dyn/cm}^2$

mean gas opacities with decreasing temperature is nicely seen in both works as well as the increase of the Planck mean gas opacity towards low temperatures. The latter is due to the increase of the concentration of the molecular opacity species.

In summery, mean gas opacity computations are very much dependent on the data for the absorption coefficients and on the thermo-chemical data. Deviations may further be introduced by differences in the elemental abundances (see Fig. 3.4) and approximations made in the process of computation.

3.5 Comparison of mean dust and gas opacities

It is known from earlier theoretical works (e.g. Fleischer 1992) that the dust component can play an important role for the dynamics of a circumstellar envelope by its large capability of absorbing momentum and radiative energy. The basic cause of this influence is the increase of the total opacity by several orders of magnitude when dust formation occurs. Consequently, strong gas opacities might lower the importance of the dust, since the molecules gain influence in comparison to the dust. Therefore, the mean gas opacities shall be compared to the opacity of dust grains which might form in carbon-rich and oxygen-rich environments.

author	Line opacity	Continuum opacity	Scattering	elemental abundances
present work	CO, TiO, H_2O, SiO, CN, CH, C_2, C_3, HCN, C_2H_2	**f-f (et):** H, H^-, H_2^+, H_2^-, He, He^-, C, Mg, Si, Al **b-f (et):** H, H^-, He, C, Mg, Si	Thomson (e^-), Rayleigh: H, He	see Table 2.1
Höfner (1997)	CO, TiO, H_2O, SiO, CN, CH, C_2, C_3, HCN, C_2H_2	**f-f (et):** H, H^-, H_2^+, H_2^-, He, He^-, C, Mg, Si, Al **b-f (et):** H, H^-, He, C, Mg, Si	Thomson (e^-), Rayleigh: H, He	Andersen & Grevesse (1989) solar
Opacity Project [a] (Seaton et al. 1994)	H, He, C, N, O, Ne, Na, Mg, Al, Si, S, Ar, Ca, Cr, Mn, Fe, Ni and all ionization states of these atoms	**f-f (et):** H, He **b-f (et):** H^- **b-f (et):** H^-	Rayleigh: H, He	Andersen & Grevesse (1989) solar
Sharp (1992)	**et:** C_2, N_2, O_2, OH, CH, CN, CO, NO, MgH, AlO, SiO, NaH, SH, MgO, TiO, CO^+,N_2^+ **vb:** OH, CO, NO, SiO, HCl, HF, H_2O, CO_2 **cia:** H_2-H_2 H_2-He	**f-f (et):** H, H^-, He^-, C^-, N^-, Ne^-, Na^-, Cl^-, Ar^-, H_2^-, N_2^-, O_2^-, CO^-, H_2O^-, **b-f (et):** H, H^-, C^-, O^-, F^-, Si^-, S^-, Cl^-, OH, CH	Thomson (e^-), Rayleigh: H_2, C_2, O_2, CO, OH, SiO, H_2O, CO_2	solar
Scholz & Tsuji (1984)	CO, H_2O, TiO, OH, CN, CH, C_2, MgH, SiH, CaH, HCN, C_2H_2 **cia:** H_2-H_2	H, H^-, H_2^-, He^-, Mg, Si, Ca	Thomson (e^-), Rayleigh: H, H_2	Allen (1973) solar
Ohnaka & Tsuji (1998) (Aoki & Tsuji 1997)	CO, H_2O, TiO, OH, CN, CH, C_2, MgH, SiH, CaH, HCN, C_2H_2 **cia:** H_2-H_2	H, H^-, H_2^-, He^-, Mg, Si, Ca	Thomson (e^-), Rayleigh: H, H_2	Allen (1973) solar

Table 3.3: Opacity sources included in gas mean opacity computations by different authors et = electronic transitions (f-f = free-free transitions, b-f = bound-free transition), vb = vibrational transitions, cia = collision induced absorption.

[a] http://vizier.u-strasbg.fr/OP.html

3.5.1 Approach

According to Eqs.(3.20) and (3.21) the dust opacity can be calculated from the degree of condensation of a considered grain species, which in principle is a result of a detailed dust formation calculation by the moment method developed by Gail & Sedlmayr (1988) (see Chapter 4).

The dust absorption coefficient is computed from the equation

$$\kappa_{\mathrm{X}}^{\mathrm{d}}(r) = \pi\, Q'_{\mathrm{X}}(T) a_{0,\mathrm{X}}^3 (\epsilon_{\mathrm{el}}^0 - \epsilon_{\mathrm{el}}) n_{<\mathrm{H}>}, \tag{3.28}$$

ϵ_{el}^0 and ϵ_{el} indicating the initial and the actual elemental abundance in the gas phase, respectively, of the element responsible for the homomolecular grain formation (e.g. Si for silicate dust). X denotes the dust species (e.g. SiO for silicate dust). $n_{<\mathrm{H}>}(\epsilon_{\mathrm{el}}^0 - \epsilon_{\mathrm{el}})$ is the fraction of the element el having been consumed by grain formation.

The degree of condensation $f_{\mathrm{c}}^{\mathrm{X}}$ determines the remaining elemental abundances in the gas and hence, the amount of molecules formed in gas phase. It is defined for the various grain species by

$$f_{\mathrm{c}}^{\mathrm{carbon}} = \frac{\epsilon_{\mathrm{C}}^0 - \epsilon_{\mathrm{C}}}{\epsilon_{\mathrm{C}}^0 - \epsilon_{\mathrm{O}}^0} \qquad f_{\mathrm{c}}^{\mathrm{silicate}} = 1 - \frac{\epsilon_{\mathrm{Si}}}{\epsilon_{\mathrm{Si}}^0} \qquad f_{\mathrm{c}}^{\mathrm{iron}} = 1 - \frac{\epsilon_{\mathrm{Fe}}}{\epsilon_{\mathrm{Fe}}^0}, \tag{3.29}$$

which leads to equations for the actual elemental abundances ϵ_{el}. For SiO also the reduction of the available oxygen is taken into account. The gas opacities are calculated after having subtracted the amount of elements considered to be condensed into grains.

3.5.2 Dust opacity data

For the hypothetical radii a_0 of the different homogeneous dust species and for the mean extinction efficiency $Q'_{\mathrm{Planck}}(T)$ and $Q'_{\mathrm{Ross}}(T)$ the following values have been used:

amorphous carbon: $a_{0,\mathrm{C}} = 1.28\ 10^{-8}$cm (Lucy 1976)

$Q'_{\mathrm{Planck}}(T) = 6.7\,T$	(Gail & Sedlmayr 1985)	$*$
$Q'_{\mathrm{Ross}}(T) = 5.9\,T$	(Gail & Sedlmayr 1985)	$*$
$Q'_{\mathrm{Planck}}(T) = 4.4\,T$	(Winters et al. 1994)	$*$
$Q'_{\mathrm{Ross}}(T)/T$	(Preibisch et al. 1993)	$**$
$Q'_{\mathrm{Planck}}(T)/T$	(Preibisch et al. 1993)	$**$

silicates: $a_{0,\mathrm{SiO}} = 2.0218\ 10^{-8}$cm (Gail & Sedlmayr 1986)

$Q'_{\mathrm{Planck}}(T) = 1.17\,T^{1.12}$	(Gail & Sedlmayr 1986)	$*$
$Q'_{\mathrm{Ross}}(T)/T$	(David & Pegourie 1995) (P)	$**$
$Q'_{\mathrm{Planck}}(T)/T$	(David & Pegourie 1995) (P)	$**$
$Q'_{\mathrm{Ross}}(T)/T$	(Draine & Lee 1985) (DL)	$**$
$Q'_{\mathrm{Planck}}(T)/T$	(Draine & Lee 1985) (DL)	$**$

The silicate dust is approximated by condensed $(\mathrm{SiO})_{\mathrm{N}}$ and therefore, $a_{0,\mathrm{SiO}}$ is calculated for pure SiO.

iron: $a_{0,\mathrm{Fe}} = 1.4151\ 10^{-8}$cm (Gail & Sedlmayr 1986)

$Q'_{\mathrm{Pl}}(T) = 3.17\ 10^{-3}\,T^{1.994}$	(Gail & Sedlmayr 1986)	$*$

The extinction efficencies marked by ($*$) are fitted data as function of T, those marked by ($**$) are tables of mean extinction efficiencies (see references).

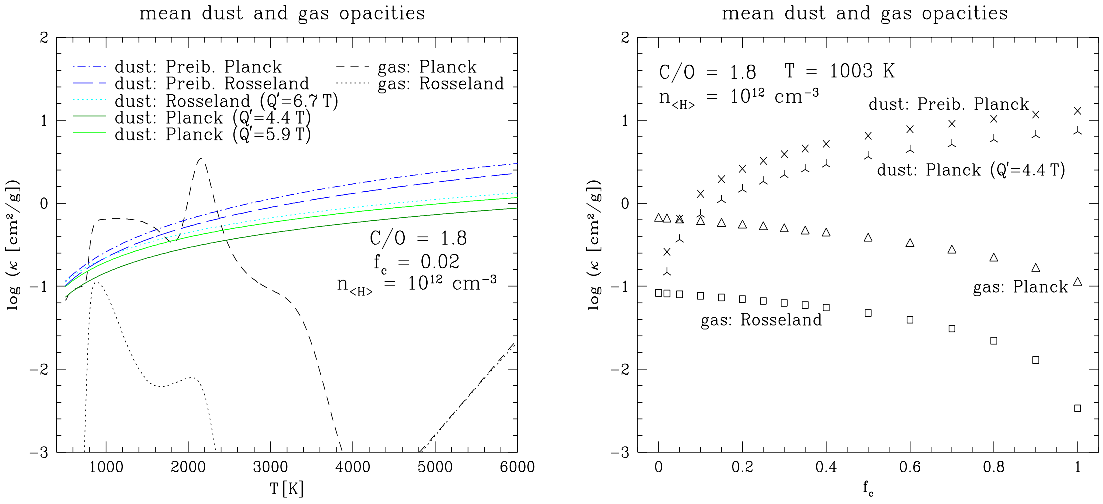

Figure 3.7: Comparison of mean dust and gas opacities for C/O=1.8. Left: Mean opacities as function of temperature T [K] for $f_c = 0.02$ and $n_{<\mathrm{H}>} = 10^{12}\mathrm{cm}^{-3}$. Right: Mean opacities as function of the degree of condensation f_c for $T = 1003$K and $n_{<\mathrm{H}>} = 10^{12}\mathrm{cm}^{-3}$.

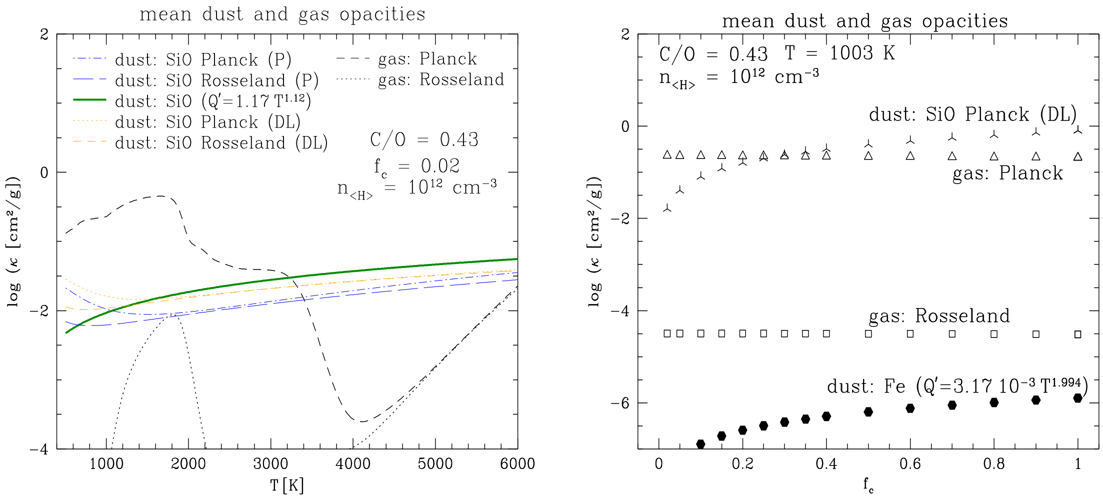

Figure 3.8: Comparison of mean dust and gas opacities for C/O=0.43. The abbreviations P and DL refere to David & Pegourie (1995) and Drain & Lee (1985), respectively. Note the different scaling of the log κ-axis. Left: Mean opacities as function of temperature T [K] for $f_c = 0.02$ and $n_{<\mathrm{H}>} = 10^{12}\mathrm{cm}^{-3}$. Right: Mean opacities as function of the degree of condensation f_c for $T = 1003$K and $n_{<\mathrm{H}>} = 10^{12}\mathrm{cm}^{-3}$.

3.5.3 Results & Discussion

The left panels of Figs. 3.7 (C/O=1.8) and 3.8 (C/O=0.43) compare mean dust opacities with Planck mean and the Rosseland mean gas opacities. The opacities are exemplarily shown as function of temperature for $f_c = 0.02$ and $n_{<H>} = 10^{12}\mathrm{cm}^{-3}$.[10]

The mean dust opacities for carbon grains are generaly much larger than those for grains possibly formed in oxygen-rich environments. The tabulated mean dust opacities $(**)$ are always larger than the fitted mean values $(*)$ for $T < 1000$K. For a given density and degree of condensation, the mean dust opacities vary much less with temperature than the mean gas opacities (left panels, Figs. 3.7, 3.8). The oxygen-rich Planck mean gas opacity takes over the oxygen-rich mean dust opacity at higher temperatures than the carbon-rich Planck mean gas opacity exceeds the carbon-rich mean dust opacity.

The right panels in Figs. 3.7 and 3.8 depict the mean gas opacities compared to the largest and smallest dust opacities exemplary for $T = 1003\,\mathrm{K}$ and $n_{<H>} = 10^{12}\mathrm{cm}^{-3}$ as function of the degree of condensation f_c. The figures indicate that the degree of condensation has to be large enough (for C/O=1.8 $f_c > 0.1$ and for C/O=0.43 $f_c > 0.3$ in the example shown) that $\chi^{\mathrm{d}} > \chi^{\mathrm{g}}$. For higher temperatures, the mean gas opacity will exceed the dust mean at a larger degree of condensation. For a given degree of condensation and decreasing density, the mean gas opacity will exceed the dust means at even lower temperatures (compare Figs. 3.2, 3.3).

In the case of effective dust formation ($f_c > 0.8$) the mean dust opacity can be 2 orders of magnitude larger than the Planck mean gas opacity in a carbon-rich environment. This difference is smaller for oxygen-rich gases ($\approx 1/2$ order of magnitude).

The figures show further that the mean gas opacities decrease and the mean dust opacities increase with increasing degree of condensation. The reason is that the material is consumed in grains with increasing degree of condensation and thereby depletes the gas phase. The depletion of the gas opacity species due to dust condensation is smaller in the oxygen-rich case since only one gas opacity source (SiO) is effected. Furthermore, Si is much less abundant than C and enough oxygen is left to be bound in TiO and CO and, therefore, the slope of the mean gas opacities in Fig. 3.3 is smaller than in Fig. 3.2.
Iron condensation has no influence on the mean gas opacities. The iron mean opacity is furthermore so small that every mean gas opacity exeeds it. Therefore, iron dust is negligible as a opacity source. In addition, John (1996) has shown that iron is also negligible as possible nucleation seed in M-stars.

3.6 Conclusion

Mean gas opacities have been presented which were calculated assuming LTE and chemical equilibrium with fixed elemental abundances. The gas was assummed to be static (i.e. line-shift was neglected) and only thermal and microturbulent line broadening were taken into account.

[10]Dust can only exist below a certain temperature $T \leq T_{\mathrm{cond}}$, hence, $\kappa^{\mathrm{dust}}(T) > 0$ for $T > T_{\mathrm{cond}}$ is an artifact of computing the dust opacity for a prescribed degree of condensation.

It has been illustrated that Planck mean gas opacities are larger than Rosseland mean gas opacities. Carbon-rich mean gas opacities often exceed oxygen-rich mean gas opacities.

Furthermore, oxygen-bearing opacity sources like TiO, SiO, and H_2O do influence the carbon-rich Planck mean gas opacities at temperatures where CO becomes less abundant. In contrast, carbon-bearing opacity sources like CH, CN, C_2, C_3, C_2H_2, and HCN do not significantly influence the opacity of an oxygen-rich gas because CH_4 will bind the free carbon at low temperatures.

Different elemental abundances cause a difference in the mean gas opacities of about one order of magnitude independent on the C/O ratio as shown by the comparison to LMC and SMC opacities.

Comparisons of different works have shown good agreement at high temperatures but substancial deviations at low temperatures. The main problems for all comparisons seem to lie in the difference of the used opacity and thermo-chemical data.

Mean dust opacities have been calculated and compare with the gas opacities.

> The mean dust opacities for carbonaceous grains are, depending on the degree of condensation, at most 2 magnitudes larger than the mean gas opacities; for oxygen-rich grains only 1/2 magnitude. Degrees of condensation of about 10% and 30% are required to make the dust opacity exceed the (Planck mean) gas opacity in the carbon-rich and oxygen-rich case, respectively. The iron dust opacity never exceeds even the Rosseland mean gas opacity. Therefore, iron dust is negligible as opacity species.

" ... phenomena tend to become more complex when studied."
Bengt Gustafsson, Nils Ryde 1996

Chapter 4

The role of molecular opacities in model atmospheres

A model of a stellar atmosphere and a circumstellar shell is composed of a system of coupled parabolic and hyperbolic differential, and integro-differential equations which have to be solved simultaneously in order to describe the close interaction between the hydrodynamics and the non-equilibrium processes like dust formation and radiative transfer. The system is closed by algebraic equations, which describe the material properties of the gas and the dust. These properties (e.g. the pressure or the opacity) are expressed in terms of the variables in the differential equations and, thus, introduce further non-linear couplings into the system.

4.1 Theoretical background - stellar atmospheres

The components which form the model of a stellar atmosphere and a circumstellar envelope include hydrodynamics, radiative transfer, the dust complex, and the chemistry. While the adopted equilibrium chemistry has already been discussed in Chapter 2, the respective theoretical background of the other model components will be shortly outlined in this section.

4.1.1 Hydrodynamics

The classical theory of hydrodynamics is applied to gas and the dust which are assumed to be co-moving and, therefore, are treated as a single continuous fluid. In other words, the drift velocity of the grains with respect to the gas is neglected in this work (for a discussion on this subject see Krüger 1997), i.e. position coupling between dust and gas is assumed. The fluid is assumed to be non-viscous[1] and non-conducting.

The basic hydrodynamic equations are solved in the fluid's (co-moving) frame, i.e. in the Lagrangian formulation. This allows to follow the individual paths of an ensemble of small fluid elements whose enclosed mass is constant.
The time derivative of a property x of a Lagrangian fluid element is described in terms of the *fluid-frame* time derivative Dx/Dt [2] which relates to the *fixed-frame* derivative

[1] However, an artificial viscosity is used to artificially broaden the shock fronts which otherwise would cause a discontinuity (cf. Sect. 4.1.5).

[2] also called Lagrangian, total, or substantial derivative

$\partial x/\partial t$ as

$$\frac{D\,x}{D\,t} = \frac{\partial x}{\partial t} + (\boldsymbol{u}\cdot\nabla)x \tag{4.1}$$

with $\boldsymbol{u}$ being the (hydrodynamic) fluid velocity and t the time.

The *equation of continuity* is

$$\frac{D\rho}{D\,t} + \rho\nabla\cdot\boldsymbol{u} = 0, \tag{4.2}$$

with ρ being the mass density of a fluid parcel. In the Lagrangian formulation, the equation of continuity is already intrinsically fulfilled as mass conservation is demanded (see Mihalas & Mihalas 1984). Instead, the equation describing the time development of the path of the fluid,

$$\frac{D\,\boldsymbol{R}}{D\,t} = \boldsymbol{u}, \tag{4.3}$$

enters into the model. $\boldsymbol{R}$ is the radial position of a certain fluid parcel. $\boldsymbol{R}(t)$ is the parcel's Lagrangian trajectory.

The *equation of motion* in the Lagrangian formulation is given by

$$\rho\,\frac{D\,\boldsymbol{u}}{D\,t} = -\nabla P_{\rm gas} + \boldsymbol{f}, \tag{4.4}$$

where $P_{\rm gas}$ is the (thermal) gas pressure, and $\boldsymbol{f} = \rho\,\boldsymbol{a}$ the external force per volume causing an acceleration $\boldsymbol{a}$ of the material. $\boldsymbol{a}$ is assumed to have only contributions from the inward directed local gravitational acceleration $\boldsymbol{g}$ and the outward directed radiative acceleration $\boldsymbol{a}_{\rm rad}$ such that

$$\boldsymbol{a} = \boldsymbol{a}_{\rm rad} - \boldsymbol{g} = -(1-\alpha)\boldsymbol{g}. \tag{4.5}$$

The radiative acceleration $\boldsymbol{a}_{\rm rad}$ is

$$\boldsymbol{a}_{\rm rad} = -\frac{\nabla P_{\rm rad}}{\rho} = \frac{4\pi}{c}\int_0^\infty \chi_\nu^{\rm tot}\,\boldsymbol{H}_\nu\,d\nu \tag{4.6}$$

with $\boldsymbol{H}_\nu$ being the Eddington flux [$\rm erg\,s^{-1}Hz^{-1}cm^{-2}$], $P_{\rm rad}$ the radiation pressure, and $\chi_\nu^{\rm tot}$ the total opacity of the gas and dust per mass [$\rm cm^2/g$].

Assuming spherical symmetry, the outlined system of three (space) dimensional equations (Eqs. 4.3, 4.4, 4.6) reduces to a system of differential equations with only one spatial coordinate. In this case, the local gravitational acceleration acting on a fluid parcel at radial distance r is

$$g = \frac{G\,M(r)}{r^2} = \frac{G(M_\star + M_{\rm s}(r))}{r^2} \tag{4.7}$$

where $M_{\rm s}(r) = \int_{R_\star}^{r} \rho(r')\,4\pi r'^2\,dr'$ is the mass contained in the circumstellar shell[3] and $M(r) = M_\star + M_{\rm s}(r)$ the enclosed mass within the radial distance r.

[3] $M_{\rm s}$ is negligible for hydrostatic computations but can amount to a considerable value of $0.1\ldots0.6 M_\odot$ for circumstellar shells (Sedlmayr & Winters 1997).

In the case of radiative equilibrium $4\pi H = L_\star/(4\pi\, r^2)$ holds ($H = \int H_\nu\, d\nu$), and $\alpha = a_{\rm rad}/g$ can be expressed by

$$\alpha = \frac{L_\star}{4\pi\, c\, G M(r)} \chi_{\rm H}. \tag{4.8}$$

$L_\star$ is the stellar luminosity, and G the gravitational constant. The flux weighted mean opacity $\chi_{\rm H}$ is defined as

$$\chi_{\rm H} = \frac{\int\limits_0^\infty \chi_\nu^{\rm tot}\, H_\nu\, d\nu}{\int\limits_0^\infty H_\nu\, d\nu}. \tag{4.9}$$

Inserting $H_\nu = -1/3\,(1/\chi_\nu^{\rm tot}\, \partial B_\nu/\partial T)(\partial T/\partial r)$, the diffusion approximation, in Eq. (4.9) leads to $\chi_{\rm H} = \chi_{\rm Ross}$ (see Eq. (3.25)). The gas pressure $P_{\rm gas}$ is determined from the thermal *equation of state* given by the *ideal gas law* for diluted gases,

$$P_{\rm gas} = \frac{\rho}{\mu\, m_{\rm H}}\, kT. \tag{4.10}$$

The mean molecular weight[4] $\mu = \mu(\rho, T)$ is defined as follows and can be calculated in good approximation from the most abundant gaseous species H, H_2, and He

$$\mu(\rho, T) = \frac{\sum_{\rm y=1}^{\rm N} n_{\rm y}(\rho, T) m_{\rm y}/m_{\rm H}}{\sum_{\rm y=1}^{\rm N} n_{\rm y}(\rho, T)} \tag{4.11}$$

$$\approx \frac{n_{\rm H} + 2n_{\rm H_2} + 4n_{\rm He}}{n_{\rm H} + n_{\rm H_2} + n_{\rm He}}. \tag{4.12}$$

$n_{\rm y}(\rho, T)$ and $m_{\rm y}$ are the particle number density and the particle mass, respectively. In all dynamical model computations described in this Chapter, the mean molecular weight is approximated to be constant such that $\mu = 1.26$ in Eq. (4.10).

For stationary situations $\partial/\partial t = 0$, and Eq. (4.2) can be integrated in the observers frame (Eulerian formulation) such that

$$4\,\pi\, r^2\, \rho(r)\, v(r) = \text{const} = \dot{M}, \tag{4.13}$$

with the integration constant $\dot{M}$ being the total mass transported through any spherical surface with radius r.

4.1.2 Radiative transfer

The radiative transfer equation which describes the interaction between a material and a photon gas can be derived in its most general form from the Boltzmann equation which describes the particle transport in kinetic theory (Mihalas 1978, Hubeny 1997).

[4]Not to confuse with the value $\mu' = \sum_{\rm i=1}^{\rm N} \epsilon_{\rm i} m_{\rm i}/m_{\rm H} \approx 1.4$ usually also named with μ. At moderate high temperatures where atomic hydrogen dominates the sum in Eq. (4.12) $\mu \approx 1.26$ (but $\mu \approx 2.2$ at lower temperatures where H_2 dominates)

For the context of this work, it is appropriate to consider the stationary (i.e. time-independent) radiative transfer equation as the hydrodynamic time scales are much larger than typical photon crossing times in the circumstellar shells of red giant stars (e.g. Winters 1994). Furthermore, the radiative transfer problem is solved assuming radiative equilibrium (RE) meaning that the total amount of the absorbed radiative energy is locally balanced by the total amount of emitted energy. This assumption is applied to all sites in the considered atmosphere including the sites of the shock fronts ("isothermal limit"). Consequently, the solution of the energy equation becomes obsolete. Assuming further local thermodynamical equilibrium (LTE), the emissivity can be expressed by the absorptivity (Kirchoff's law) and the condition of radiative equilibrium in LTE can be written as

$$\int \kappa_\nu J_\nu \, d\nu = \int \kappa_\nu B_\nu(T_{\rm RE}) \, d\nu. \tag{4.14}$$

J_ν is the mean intensity of the radiation field and $B_\nu(T_{\rm RE})$ the black body radiation field (Planck function) at the radiative temperature equilibrium $T_{\rm RE}$. Applying the Stefan-Boltzmann law to Eq. (4.14) and choosing appropriate mean opacities provides an expression for the radiative equilibrium temperature $T_{\rm RE}$ in LTE,

$$T_{\rm RE}^4 = \frac{\kappa_{\rm J}}{\kappa_{\rm Planck}} \frac{\pi}{\sigma} J, \tag{4.15}$$

with $J = \int J_\nu d\nu$. The (real) kinetic gas temperature $T_{\rm gas}$ is defined by the energy of the thermal (Brownian) motion of the gas particles equally distributed over all degrees of freedom. In the isothermal limit case the gas is assumed to relax instantaneous towards radiative equilibrium ($T_{\rm RE} = T_{\rm gas}$). Shock heating or adiabatic cooling due to expansion may lead to temporal departures of the kinetic gas temperature from the radiative equilibrium temperature (e.g. Woitke et al. 1996) but will be omitted here.

The radiative transfer problem is solved in grey approximation: **a**) In the time-dependent, hydrodynamic models the Unno-Kondo method is applied. **b**) In the hydrostatic models, which serve as initial value for the time-dependent models, the Lucy method is used.

a) The Unno-Kondo method is a generalized two-stream Eddington approximation in spherical symmetry with the separation angle[5] $\mu_{\rm r} = \cos\theta_{\rm r}$ which depends on the optical depth. Unno & Kondo (1976, 1977, Hashimoto 1995) have shown that in grey approximation the separation angle $\mu_{\rm r}$ can be calculated from

$$\frac{\partial \mu_{\rm r}^3}{\partial r} = \frac{\rho \chi_{\rm H}}{4} + \frac{3\mu_{\rm r}}{r} - \frac{5}{4} \rho \chi_{\rm H} \, {\mu_{\rm r}}^2 - 3 \frac{\mu_{\rm r}^3}{r} \tag{4.16}$$

with $\mu_{\rm r}(r_{\rm inner}) = 0$ at the inner boundary $r_{\rm inner}$.

Applying boundary conditions such that at the outer boundary ($r = R'$, R' outer boundary) any incident radiation is neglected, the desired expression for the temperature stratification is

$$T_{\rm RE}^4 = \tag{4.17}$$

$$\frac{\kappa_{\rm J}}{\kappa_{\rm Planck}} \frac{\pi}{\sigma} \frac{L_\star}{8\pi^2} \left[\frac{1}{(1+\mu_{\rm R'}) R'^2} + \frac{\mu_{\rm R'}}{R'^2} - \frac{\mu_{\rm r}}{r^2} + \frac{3}{2} \int_{\rm r}^{\rm R'} \left(\frac{\rho \chi_{\rm H}}{r'^2} + \frac{2\mu_{\rm r'}}{r'^3} \right) d\, r' \right].$$

[5] Usually, the angle $\cos\theta$ is called μ in lecture books. In order to indicate the difference to the mean molecular weight, $\mu_{\rm r}$ for $\cos\theta_{\rm r}$ is used.

Since RE is assumed, $4\pi r^2 H = const$ with respect to r at any instant of time. Because $4\pi r^2 H = L_\star/4\pi = R_\star^2 \sigma T_\star^4$ and for consistency $T_{\rm eq}(r = R_\star) = T_\star$ the implicit condition

$$\left\{ \frac{\kappa_{\rm J}}{\kappa_{\rm Planck}} \frac{r^2}{2} \left[\frac{1}{(1+\mu_{\rm R'})R'^2} + \frac{\mu_{\rm R'}}{R'^2} - \frac{\mu_{\rm r}}{r^2} + \frac{3}{2} \int_{\rm r}^{\rm R'} \left(\frac{\rho \chi_{\rm H}}{r'^2} + \frac{2\mu_{\rm r'}}{r'^3} \right) d\,r' \right] \right\}_{\rm r=R_\star} = 1 \tag{4.18}$$

needs to be fulfilled (cf. Eq. 4.17) which determines the current value of $R_\star$ (and $T_\star$).
b) The Lucy approximation (Lucy 1971, 1976) can be obtained from Eq.(4.17) by putting $R' = \infty$ and $\mu_{\rm r} = \mu_\star = \sqrt{(1 - R_\star^2/r^2)}$:

$$T_{\rm RE}^4 = \frac{\kappa_{\rm J}}{\kappa_{\rm Planck}} \frac{T_\star^4}{2} \left(W + \frac{3}{2} \tau_{\rm L} \right), \tag{4.19}$$

containing the radial dilution factor W,

$$W = \begin{cases} 1 & r \leq R_\star \\ 1 - \sqrt{1 - \left(\frac{R_\star}{r}\right)^2} & r > R_\star \end{cases} \tag{4.20}$$

and the Lucy optical depth $\tau_{\rm L}$,

$$\tau_{\rm L} = \int_r^\infty \left(\frac{R_\star}{r'} \right)^2 \rho \chi_{\rm H} \, d\,r'. \tag{4.21}$$

The implicit consistency condition Eq.(4.18) simplifies to

$$\frac{1}{2} \frac{\kappa_{\rm J}}{\kappa_{\rm Planck}} \left(1 + \frac{3}{2} \tau_{\rm L}(r = R_\star) \right) = 1 \tag{4.22}$$

which fixes again $R_\star$.

The opacities entering the equations are the intensity weighted mean $\kappa_{\rm J} = \int \kappa_\nu J_\nu d\nu / \int J_\nu d\nu$ (absorption mean), the Planck mean $\kappa_{\rm Planck}$ (Eqs. (3.22), (3.25)), and the flux weighted opacity $\chi_{\rm H}$ (Eq. (4.9)), respectively. The intensity weighted mean and the flux weighted mean opacity, $\kappa_{\rm J}$ and $\chi_{\rm H}$, can only be calculated when the frequency-dependent radiative transfer problem has been solved. In contrast, the Planck mean opacity (and also the Rosseland mean opacity) can be calculated as function of ρ and $T_{\rm gas}$ without knowing the solution for the radiative transfer. Therefore, any kind of pre-calculation of $\kappa_{\rm J}$ and $\chi_{\rm H}$ introduces errors in the optical depth scale, the temperature stratification, and in $\alpha = a_{\rm rad}/g$.

In the inner and more dense parts of the photosphere, the diffusion approximation holds and the flux weighted mean opacity can be approximated by the Rosseland mean opacity, $\chi_{\rm H} = \chi_{\rm Ross}$ (cf. Mihalas 1978). Furthermore, the mean intensity is approximately given by B_ν. Therefore, $\kappa_{\rm J} = \kappa_{\rm Planck}$ is a good approximation. The latter causes the cancellation of the first factor in Eqs. (4.17) and (4.19).

In the outer parts, however, where the density is very low, the gas becomes optically thin and the diffusion approximation is not valid. In addition, in such cool regions the effect of molecular absorption influences the temperature stratification substantially and the mean intensity J_ν can no longer be considers as that of a black body.

Nevertheless, with the available computer facilities, so far, no frequency-dependent radiative transfer, consistently coupled to the complex of hydrodynamics and dust formation, can be solved in an acceptable amount of CPU time. Therefore, mean molecular opacities are applied in this work. For a more realistic treatment of the radiative acceleration by molecules, $\chi_{\rm H} = \kappa_{\rm Planck}$ is assumed. This choice is reasonable as, in a moving medium, χ_ν would likely be continuously shifted to values with higher H_ν (see also Sect. 1.2, Sect. 3.1.1.1). For comparison, time-dependent models with $\chi_{\rm H} = \chi_{\rm Ross}$ have been computed which are correct in the dense, inner parts of the atmosphere.

4.1.3 Dust complex

Dust formation is a complex non-equilibrium process leading from single molecules, which are described by their atomic structure, to macroscopic (solid) particles, which can already be described by bulk characteristics. Beside growth processes like surface reactions and coagulation, also destructive processes like sputtering, shattering, or evaporation can influence the temporal evolution of the dust component.

Krüger (1992) has shown that coagulation of dust particles is negligible for typical relative velocities of the particles in circumstellar shells of late-type stars (also Krüger 1997) but dust evaporation might have a significant effect (Gauger et al. 1990).

The dust formation process can be considered as a two-step molecule-solid transition where 1.) small meta-stable clusters form from the gas phase (*nucleation*) and 2.) these seeds grow to macroscopic particles (*grain growth*). The nucleation (seed formation) is described by the modified classical nucleation theory (Gail & Sedlmayr 1984, see also Patzer 1998) based on results from chemical equilibrium calculations for the small molecules. The grain growth and evaporation are handled by the moment method developed by Gail & Sedlmayr (1988) and Gauger et al. (1990).

The domain of dust nucleation can in principle be approached from the chemical point of view, namely, a) by the chemical pathway approach, where the solid formation is a result of a sequence of chemical reactions along the most frequently passed reaction channel through the network (Goeres 1991, 1993), or b) by a computation of the whole chemical rate network leading under favorable conditions to more and more complex molecules (Frenklach & Feigelson 1989, Cherchneff et al. 1992, Allain 1996).

In the domain of dust nucleation, for clusters smaller than a critical size N_*, the individual structure of the particles (seeds) is important for the formation process[6] (Patzer et al. 1995, Köhler et al. 1996). N_* is defined by the equilibrium of evaporation and growth for a given temperature. Thereby, the rate of growth is approximately constant in temperature but the evaporation rate is exponentially increasing with temperature. Beyond the critical cluster, the particle preferentially grow by addition of further molecules. The formation of the critical cluster, and therefore the computation of the nucleation rate $J_*(r,t)$ can be treated as a stationary problem (Gail & Sedlmayr 1988, Gauger et al. 1990) if the growth time scales in the nucleation regime are small compared to the hydrodynamic time scales (and small compared to radiative processes if a complete radiative transfer is considered).

Well beyond the critical cluster, the grains can be characterized by the bulk properties of the grain material. The relevant grain properties in arbitrary moving media

[6] more correct: for the evaporation rate

can be described by the moments $K_{\rm i}(r,t)$ of the local size distribution function of the dust grains $f(r,N,t)$

$$K_{\rm i}(r,t) = \frac{1}{n_{<\rm H>}} \sum_{\rm N=N_{\it l}}^{\rm N_{max}} N^{{\rm i}/d} f(r,N,t), \qquad {\rm i}=0,1,2,3,\ldots \tag{4.23}$$

with $d=2,3$ being the spatial dimension of the cluster. N_l is the lower limit size for dust grains to be considered as macroscopic particles.

Important properties of the dust formed can be derived from the moments by the following identification:

$$n_{\rm d} = K_0\, n_{<\rm H>} \qquad \text{NUMBER OF DUST PARTICLES PER VOLUME,} \tag{4.24}$$
$$r_{\rm m} = a_0 \frac{K_1}{K_0} \qquad \text{MEAN PARTICLE RADIUS,} \tag{4.25}$$
$$f_c = \frac{K_3\, n_{<\rm H>}}{n_{\rm cond}} \qquad \text{DEGREE OF CONDENSATION,} \tag{4.26}$$

$n_{\rm cond}$ being the hypothetical atom number density of condensible material in the gas phase and a_0 is the hypothetical radius of the monomers forming the grain[7]. The grain radius a is defined by $a = a_0 N^{1/d}$.

The moment equations,

$$\frac{D\,K_0}{D\,t} = J_*(r,t) \tag{4.27}$$
$$\frac{D\,K_{\rm i}}{D\,t} = N_l^{\rm i/d} J_*(r,t) + \frac{\rm i}{\rm d}\frac{1}{\tau_{\rm gr}} K_{\rm i-1}, \qquad {\rm i}=1,2,3,\ldots \tag{4.28}$$

form a non-linear coupled system of equations which describes the time evolution of the dust. The transition from the critical cluster $N_*(\approx 10)$ to $N_l(\approx 1000)$ is again assumed to be a stationary process, therefore $J(r,N_*,t) = J(r,N_l,t) = J_*(r,t) = const(N)$, $J_*(r,t)$ being the stationary formation rate of critical clusters N_* (the "seeds") per hydrogen atom per unit volume at time t. $\tau_{\rm gr}$ is the time scale of the particle growth, $1/\tau_{\rm gr}$ denoting the rate of how many monomers N are accreted to a dust particle per unit time and unit surface. The nucleation rate $J_*(r,t)$ and the growth time scale $\tau_{\rm gr}$ are calculated as described in Fleischer (1994).

4.1.4 Initial values and boundary conditions

The system of coupled equations outlined in Sects. 4.1.1, 4.1.2, and 4.1.3 can only be solved if initial values as well as boundary conditions are specified.

The *initial values* are given by the hydrostatic case assuming $u=0$ (*hydrostatic equilibrium*) where the gradient of the total pressure $P_{\rm tot}$ balances the gravitational acceleration,

$$-\nabla P_{\rm tot} = \rho\, g, \tag{4.29}$$

[7] a_0 depends on the monomer species and is therefore different for dust formed in an oxygen-rich gas from that formed in a carbon-rich gas (see also Sect. 3.5.2).

with $P_{\rm tot} = P_{\rm gas}+P_{\rm rad}$. Turbulent pressure is neglected. The gas pressure is demanded to diminish at infinity. Furthermore, no dust shall be formed yet, therefore, $K_{\rm i} = 0$. The initial value of the luminosity at $t = 0$ is $L_0 = L_\star$.

The *inner boundary condition* for the radial position $R_{\rm inner}$ is prescribed by a piston approximation where the inner radial position varies sinusoidally in time,

$$R_{\rm inner} = R_{\rm inner,0} + \Delta u \, \frac{P}{2\,\pi} \, \sin\left(\frac{2\,\pi}{P} t\right), \tag{4.30}$$

where P is the piston period, $\Delta\,u$ the piston's amplitude, and $R_{\rm inner,0}$ is the inner radial position at time $t = 0$. Hence, the velocity u varies with the cosine of the time. The radiative flux $4\pi H$ through the inner boundary $R_{\rm inner}$ is assumed to be constant (see Eq. 4.17), which serves as inner boundary condition for the solution of the radiative transfer problem.

$$\frac{L_\star}{4\,\pi\,R^2_{\rm inner}} = \frac{L_0}{4\,\pi\,R^2_{\rm inner,0}} = const. \tag{4.31}$$

At the *outer boundary*, no condition is prescribed and free expansion can take place. Any incident radiation is neglected (see Sect. 4.1.2).

4.1.5 Numerical approach

The discretization of the differential equations in space is done by standard finite differences on a staggered mesh in the co-moving frame according to Richtmyer & Morton (1967). The time discretization is standard explicit Eulerian. The time step size is adjusted according to the hydrodynamic situation (for details see Fleischer 1994).

Artificial viscosity Strong shock waves can introduce discontinuities in the equation of motion. To make a numerical treatment of such physical situations still possible, an artificial viscosity in form of a viscous pressure gradient $\nabla\,P_{\rm visc}$ is introduced according to Tscharnuter & Winkler (1979) in Eq. (4.4),

$$P_{\rm visc} = -\frac{4}{3}\rho\mu_{\rm Q}\left(\frac{\partial u}{\partial r} - \frac{\mu_{\rm Q}}{2}\frac{u}{r}\right), \tag{4.32}$$

$\mu_{\rm Q}$ being the artificial viscosity. The assumed value in the model computations is $\mu_{\rm Q} = 2.0$. The viscous pressure gradient artificially broadens the shock fronts, so that the occurrence of discontinuities is suppressed and spatial derivatives can be computed in the usual way.

4.2 Hydrostatic model atmosphere – The initial model –

The system of integro-differential equations described in Sect. 4.1 forms an initial value problem. Consequently, the solution depends on the initial structure of the atmosphere and the circumstellar envelope which is assumed to be given by the static stratification (Sect. 4.1.4). A closer look on the static solution will therefore be taken in this section, which already provides some important clues to the time-dependent behavior to be presented in Sect. 4.3. Emphasis will be given to the influence of different opacity treatment and opacity approximations on the hydrostatic structure compared to photospheric non-grey models.

4.2.1 Influence of different opacity treatment on the structure of the initial models

Hydrostatic models were computed assuming $\kappa_{\rm J} = \kappa_{\rm Planck}$, $\chi_{\rm H} = \kappa_{\rm Planck}$ or $\chi_{\rm H} = \chi_{\rm Ross}$ or $\chi_{\rm H} = const$, respectively. The Planck mean and the Rosseland mean gas opacities have been calculated on the basis of the Copenhagen molecular opacity data (Chap. 2). Otherwise will be stated. Comparisons to the static models computed with constant and mean opacities used as inital models in e.g. in Fleischer (1994) and Winters (1994) are made (cf. Table 4.1).

	reference	$T_\star$	$L_0/L_\odot$	$M_\star/M_\odot$	log g	C/O
$\chi^{\rm g} = 2\times10^{-4}{\rm cm}^2/{\rm g}$	Bowen 1988	2800K	6×10^3	1	[-0.59]	1.8
Rosseland mean	Scholz & Tsuji 1984	2800K	6×10^3	1	[-0.59]	1.8
Rosseland mean	this work	2800K	6×10^3	1	[-0.59]	1.8
Planck mean	this work	2800K	6×10^3	1	[-0.59]	1.8
frequency-dependent	MARCS	2800K	[6×10^3]	1	-0.6	1.8
$\chi^{\rm g} = 2\times10^{-4}{\rm cm}^2/{\rm g}$	Bowen 1988	2800K	6×10^3	1	[-0.59]	0.43
Rosseland mean	Scholz & Tsuji 1984	2800K	6×10^3	1	[-0.59]	0.43
Rosseland mean	this work	2800K	6×10^3	1	[-0.59]	0.43
Planck mean	this work	2800K	6×10^3	1	[-0.59]	0.43
frequency-dependent	MARCS	2800K	[6×10^3]	1	-0.6	0.43

Table 4.1: Input parameter (numbers without brackets) for the hydrostatic model atmospheres computed with different gas opacity treatment. All models are computed with mean gas opacities except the MARCS[8] model which represents a full frequency-dependent model atmosphere including convective energy flux.

The term "constant opacity" indicates that a frequency, temperature and pressure-independent opacity value per mass, $\chi^{\rm g} = 2\times10^{-4}{\rm cm}^2/{\rm g}$ (Bowen 1988), is used.

The static models are computed by applying the Lucy approximation (Sect. 4.1.2) for the temperature determination. In the grey case, where $\kappa_{\rm J} = \kappa_{\rm Planck}$ is valid, this condition is equivalent to $\tau_{\rm L}(R_\star) = 2/3$ ([9]). The Lucy approximation causes a discontinuous derivative $\partial T/\partial r\big|_{{\rm R}_\star}$ because it distinguishes between a region $r < R_\star$

[8]Additional model input characteristics for the MARCS model are: number of sampling points ≈ 5300 for line opacities of C_2, C_3, CH, CN, HCN, C_2H_2, CO, TiO, H_2O, SiO.

[9]In frequency-dependent hydrostatic atmospheres the radius is often defined to be where $\tau_{\rm Ross} = 1$. See e.g. Baschek et al. (1991).

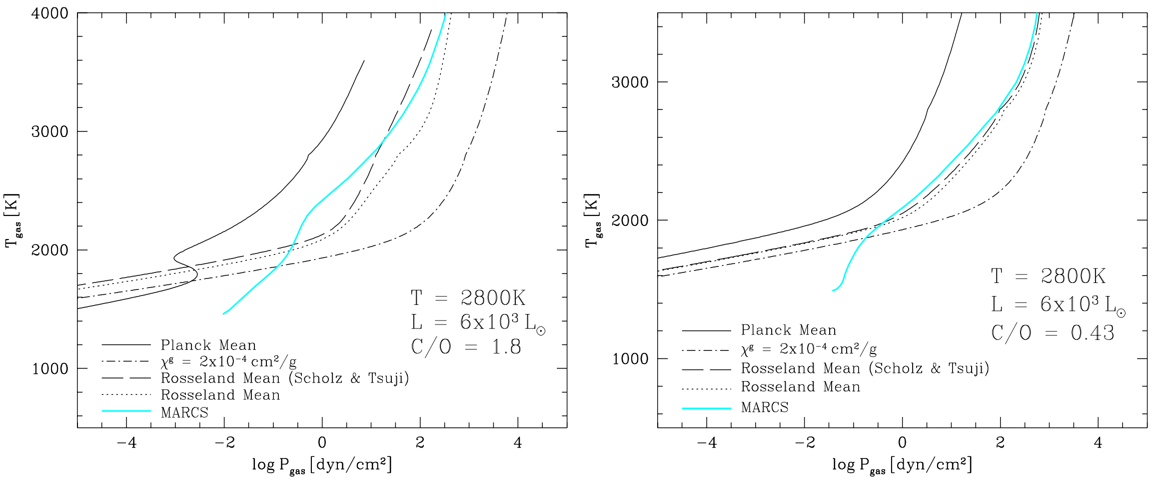

Figure 4.1: Differences in the $T - P_{\rm gas}$ structure between various hydrostatic initial models (left: C/O=1.8, right: C/O=0.43) computed with new Rosseland mean and Planck mean gas opacities, Rosseland mean gas opacities from Scholz & Tsuji (1984), a constant opacity per mass $\chi^{\rm g} = 2 \times 10^{-4}{\rm cm}^2/{\rm g}$ (Bowen 1988), and a non-grey MARCS model (cf. Table 4.1).

and a region $r > R_\star$ (Eq. 4.20). The innermost radial grid point is chosen to be $R_{\rm inner,0} = 0.91 R_\star(0)$ and a constant mean molecular weight $\mu = 1.26$ is assumed.

❑ **I.)** All models computed with different gas opacity approximations (Rosseland mean, Planck mean, constant opacity, Fig. 4.1) differ - for both C/O values - very strongly from the model calculated by solving the proper frequency-dependent radiative transfer problem (thick grey lines, Fig. 4.1). As already shown (e.g. Helling & Jørgensen 1998), models computed with the constant opacity (dash-dot lines, Fig. 4.1) deviate most. These models show temperature deviations at given pressure $\gtrapprox$ 800K in the inner regions (left panel of Fig. 4.1). Models computed with Rosseland mean gas opacities resemble the inner regions of the photosphere best which indicates that the diffusion approximation is a good approximation for those hot and very dense atmospheric regions. The Rosseland mean, however, is no good approximation for $\chi_{\rm H}$ in the outer atmospheric regions since the diffusion approximation is no longer valid. Due to the very complex frequency-dependence of the opacity of molecular gases (see Sect. 3.2.1), the averaging process involved in the calculation of the mean gas opacity values is crucial. Consequently, the differences between $\chi_{\rm Ross}$ and $\chi_{\rm H}$ (and between $\kappa_{\rm Planck}$ and $\kappa_{\rm J}$) are particularly strong in the outer, molecule-rich regions, where the strongest temperature differences between grey and frequency-dependent models occur. The surface cooling due to molecular lines is practically not present in grey models which causes too high temperatures in the surface layers. The only effect which decreases the temperature in the outer, optically thin layers of grey spherically symmetric atmospheres is the radial dilution (see Eqs. 4.19, 4.20) [10].

[10]The non-existing surface cooling in grey atmospheres can be nicely seen from plane-parallel model computations where the temperature decreases outwards - no matter which grey opacity is used - to a limiting value of $0.811\,T_{\rm eff}$. (Mihalas (1978), p. 71 ff.)

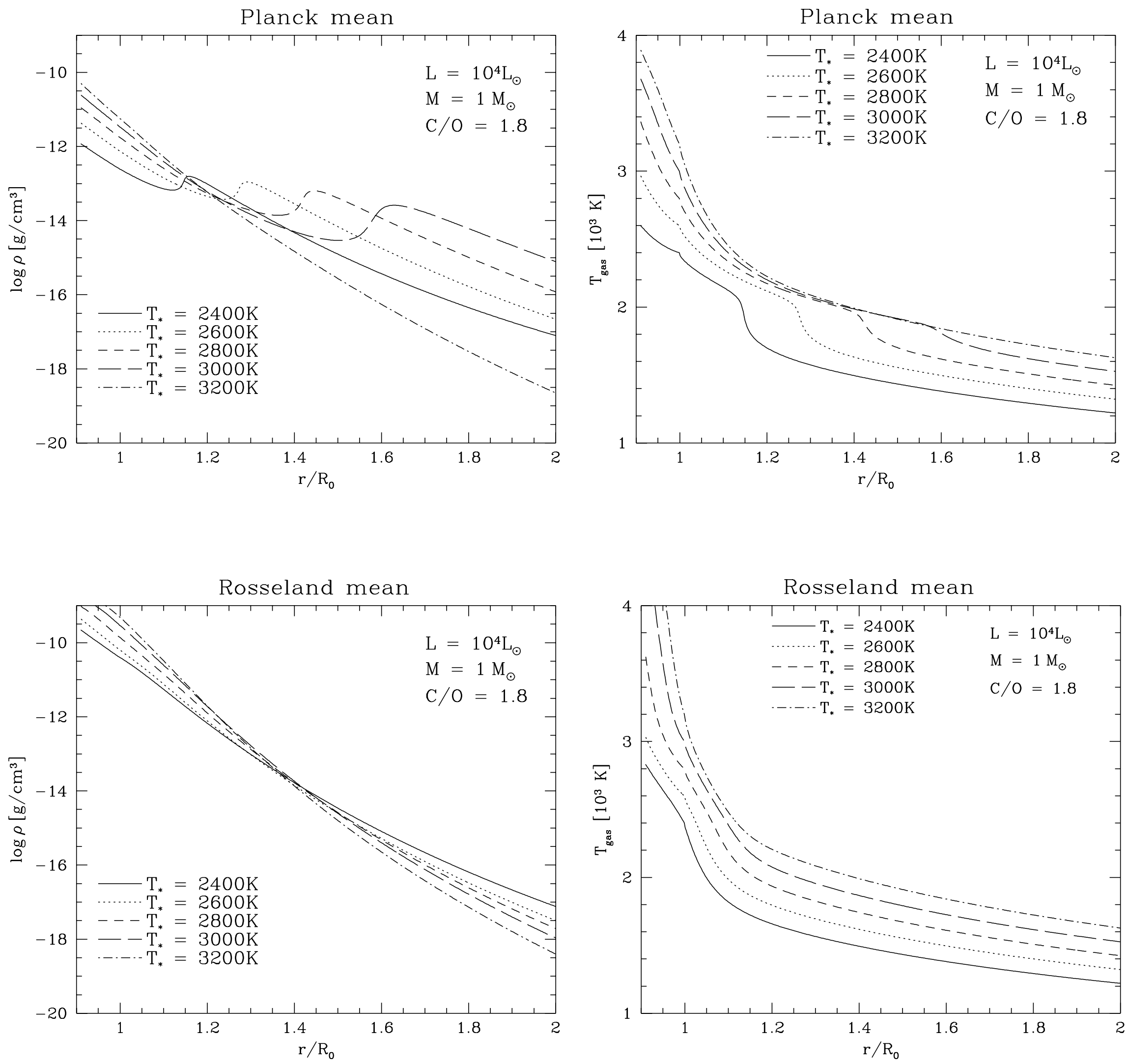

Figure 4.2: Density (left column) and gas temperature (right column) against radial distance in units of the initial radius R_0 of a sequence of hydrostatic models computed with Planck mean (upper row) and Rosseland mean gas opacities (lower row) (cf. Table 4.2).

Static models computed with Rosseland mean opacities from Scholz & Tsuji (1984, long dashed lines, Fig. 4.1) and with Rosseland mean opacities calculated in this work (dotted lines, Fig. 4.1) are similar in the oxygen-rich case but deviate considerably in the carbon-rich case at high temperatures $T_{\rm gas} \gtrapprox 2200$K.

From Fig. 3.5, one might note that, depending on the density, the oxygen-rich Rosseland mean gas opacities are similar for $T_{\rm gas} \gtrapprox 2500$K (right lower panel), but the carbon rich Rosseland mean gas opacities differ for $T_{\rm gas} \gtrapprox 2200$K (left lower panel). Keeping in mind that $T_{\rm gas} = T_{\rm RE}(r, \tau)$ and $\tau = \int \chi\rho\, dr$, these differences in the static model structure occur at similar temperatures where, however, the carbon-rich static models computed with the opacity data from Scholz & Tsuji (1984) and the models computed with opacity data from this work deviate from each other.

The static models computed with Planck mean gas opacities generally yield much lower densities than the frequency-dependent models do in the atmosphere because the Planck mean gas opacity is too high compared to $\chi_{\rm H}$ as it gives weight to strong lines. The Rosseland mean models, on the other hand, have higher densities than the frequency-dependent models in the atmosphere as its opacity is too low in comparison. The density at $r = R_\star$ of Rosseland and Planck mean opacity models differ by almost 2 orders of magnitude.
The density differences between the models shown in Fig. 4.1 are a consequence of the evaluation of the optical depth $\tau_{\rm L}$: large values of χ require small values of ρ, if the same optical depth is considered – and vice versa.

The most striking features of the static models with Planck mean opacities are the local pressure inversion which can occur in the outer regions of static carbon-rich models. No pressure inversion were found in the oxygen-rich case.

	$T_\star$	$L_0/L_\odot$	$M_\star/M_\odot$	C/O	R_0	log g
Planck mean	2400K	10^4	1	1.8	[$4.02\,10^{13}$cm]	[-1.09]
(this work)	2600K	10^4	1	1.8	[$3.42\,10^{13}$cm]	[-0.93]
	2800K	10^4	1	1.8	[$2.95\,10^{13}$cm]	[-0.82]
	3000K	10^4	1	1.8	[$2.57\,10^{13}$cm]	[-0.70]
	3200K	10^4	1	1.8	[$2.26\,10^{13}$cm]	[-0.59]
Rosseland mean	2400K	10^4	1	1.8	[$4.02\,10^{13}$cm]	[-1.09]
(this work)	2600K	10^4	1	1.8	[$3.42\,10^{13}$cm]	[-0.93]
	2800K	10^4	1	1.8	[$2.95\,10^{13}$cm]	[-0.82]
	3000K	10^4	1	1.8	[$2.57\,10^{13}$cm]	[-0.70]
	3200K	10^4	1	1.8	[$2.26\,10^{13}$cm]	[-0.59]

Table 4.2: Input parameter (numbers without brakes) for the investigated sequence of grey hydrostatic model atmospheres.

❑ **II.)** A closer look at the sequence of hydrostatic model structures with varying stellar temperature (Fig. 4.2) shows that the overall density range of the models computed with Rosseland mean gas opacities is smaller than the range of models computed with Planck mean gas opacities. The different slopes of the $\rho(r)$-curves correspond to different surface gravities of the models (see Table 4.2). The variations in the slopes, i.e. the different density ranges, are related to the occurrence of the pressure inversions in the Planck mean opacity models (appearing as density inversion in Fig. 4.2) which disappear with increasing stellar temperature. In the sequence of

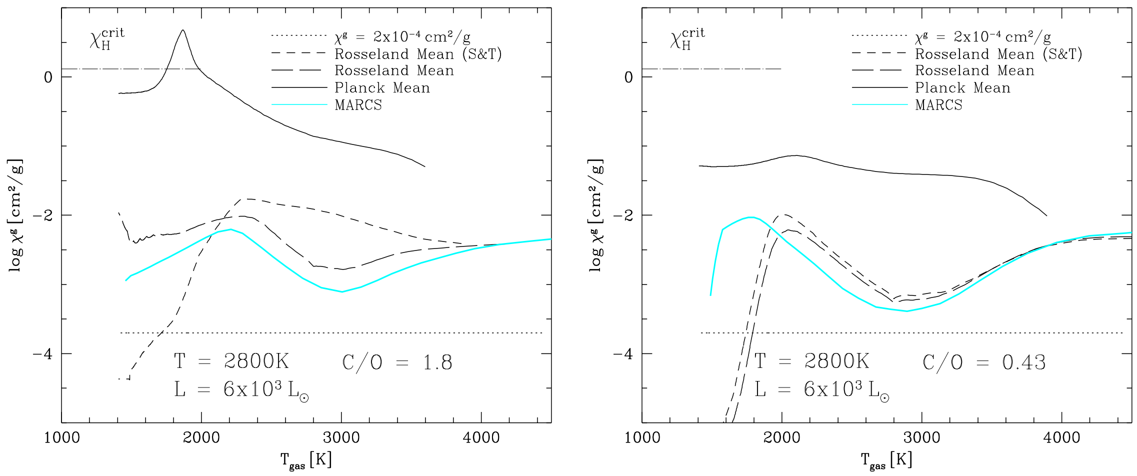

Figure 4.3: Carbon-rich (left) and oxygen-rich (right) mean opacities for an exemplary model in comparison to the critical flux weighted mean opacity.

Planck mean opacity models shown in Fig. 4.2 pressure inversions are only found for $T_\star \leq 3000\mathrm{K}$ ($L_\star = 10^4 L_\odot$, $M_\star = 1\,M_\odot$).

The occurrence of pressure inversions might have some implications on the possibility of dust formation in circumstellar envelopes:

- The strongest "levitation" (a density enhancement) of the outer static atmosphere due to molecular absorption is found for models in a particular range of the stellar temperature of $2800\,\mathrm{K} < T_\star < 3000\mathrm{K}$. For these models, densities as large as $10^{-15}\mathrm{g/cm^3}$ occur at distances of $r \approx 2\,R_\star$, even in the static case.

- The locally increased density causes a local increase of the optical depth which, in turn, causes an increase of the temperature within the corresponding layer. This molecular backwarming might prevent the nucleation in those regions which is the first step on the path of dust formation.

4.2.2 Discussion

The gas pressure inversions in Planck mean gas opacity models are caused by strong local opacities such that a local outwards increasing gas pressure P_{gas}, i.e. a positive gas pressure gradientoccurs.

In hydrostatic equilibrium $\rho g(1-\alpha) = -\nabla P_{\mathrm{gas}}$ is valid. Therefore, the occurrence of pressure inversions is directly related to α:

$$\alpha < 1 \quad \Rightarrow \quad \frac{\partial P_{\mathrm{gas}}}{\partial r} < 0 \quad \text{no gas pressure inversion} \tag{4.33}$$

$$\alpha > 1 \quad \Rightarrow \quad \frac{\partial P_{\mathrm{gas}}}{\partial r} > 0 \quad \text{gas pressure inversion,} \tag{4.34}$$

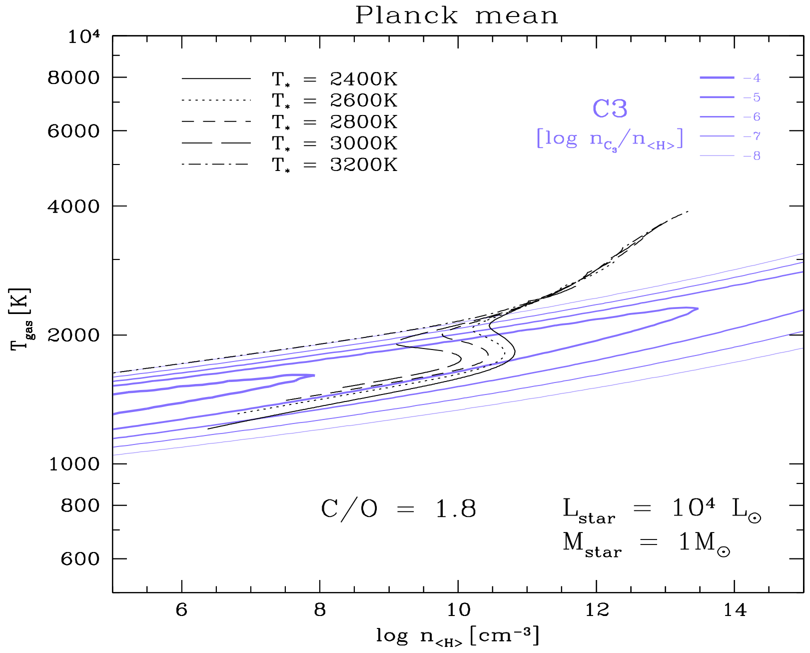

Figure 4.4: The $T_{\rm gas} - n_{<\rm H>}$ structures of the Planck mean model sequence listed in Table 4.2. Additionally, a contour plot of the C_3 logarithmic concentration relative to hydrogen is depicted.

and a critical mean opacity value $\chi_{\rm H}^{\rm crit}$, corresponding to $\alpha = 1$ (cf. Eq. 4.8), is given by

$$\chi_{\rm H}^{\rm crit} = \frac{4\pi c\, G\, M}{L_\star} \approx \frac{4\pi c\, G\, M_\star}{L_\star}. \tag{4.35}$$

A typical value for $M_\star = 1\,M_\odot$ and $L_\star = 6 \times 10^3 L_\odot$ is $\chi_{\rm H}^{\rm crit} = 2.17$ cm^2/g ([11]). If at some r the mean opacity exceeds $\chi_{\rm H}^{\rm crit}$, the gas pressure must increase in order to counterbalance the strong local radiative acceleration and to maintain the hydrostatic equilibrium.

Figure 4.3 shows different mean opacities compared to the critical flux weighted mean for a static model with $T_\star = 2800$K, $L_\star = 6 \times 10^3 L_\odot$, and $M_\star = 1\,M_\odot$. The oxygen-rich Planck mean gas opacities (right panel) never exceed $\chi_{\rm H}^{\rm crit}$, and therefore, no pressure inversions occur in this models. The same is valid for all Rosseland mean opacity models. Only the carbon-rich Planck mean opacities exceed the critical opacity value in some atmospheric zones (left panel). It is clear from Eq. (4.35) that pressure inversions will occur easier for higher luminosities.

The number densities of three of the molecules which are mainly responsible for the strong increase of the opacity are shown in the Figs. 4.4 and 4.5 in comparison to the atmospheric structure of the Planck mean model sequence listed in Table 4.2. Comparing the course of these static models with the contour lines indicates that

[11] For the used values of the natural constants see Appendix Table A.1.

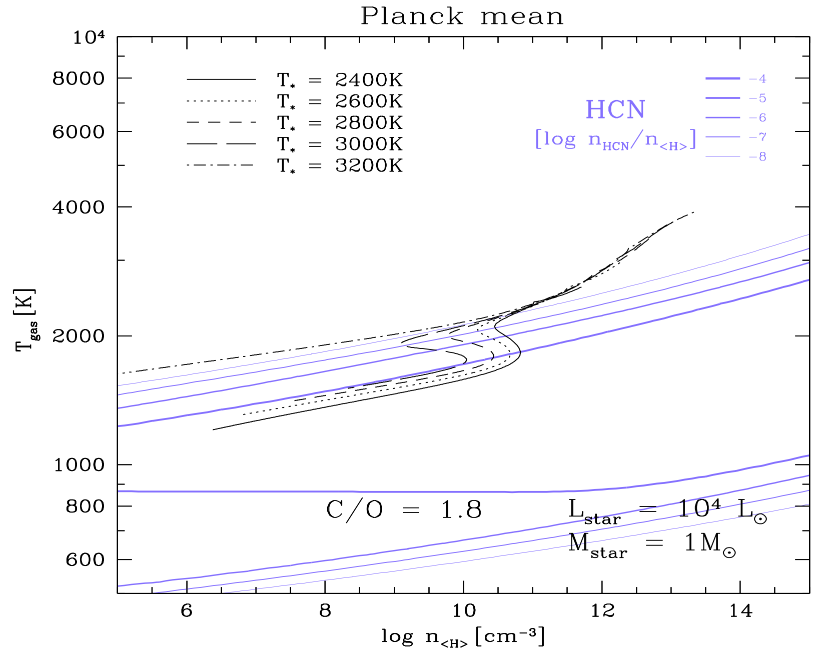

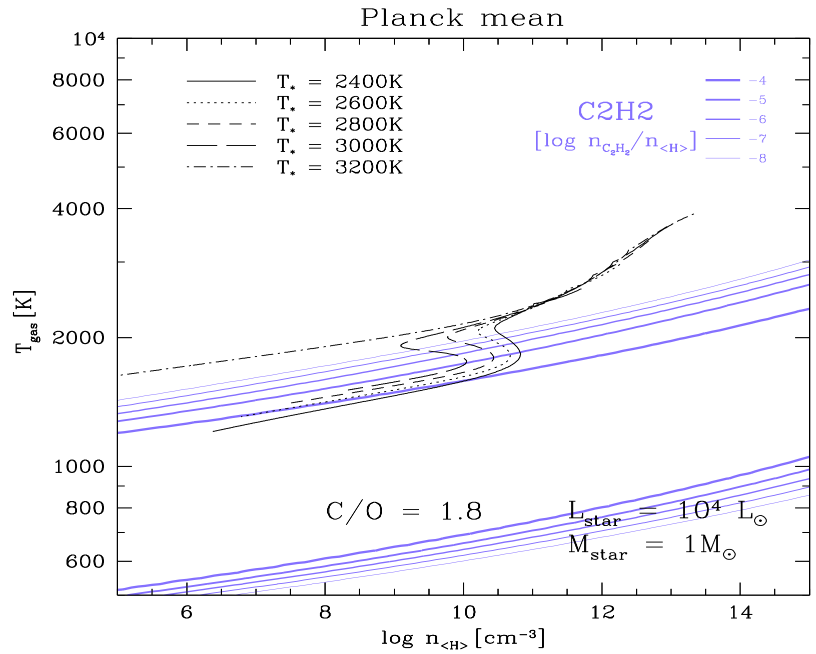

Figure 4.5: The $T_{\mathrm{gas}} - n_{<\mathrm{H}>}$ structures of the Planck mean model sequence listed in Table 4.2. Additionally, contour plots of the HCN (upper panel) and C_2H_2 (lower panel) logarithmic concentration relative to hydrogen are depicted.

the sites of the pressure inversions coincide well with the sites of maximum C_3-concentration, but not with the HCN- or C_2H_2- concentrations. In the case of C_3 (Fig. 4.4), the pressure inversions do coincide with the increase of $n_{C_3}/n_{<H>}$ towards its maximum value of about 10^{-4}. Note that also the "end" of the pressure inversions at low temperatures coincide with smaller C_3-concentrations. This is not the case for HCN and C_2H_2, and in addition, the number densities are roughly one order of magnitude smaller compared to C_3. Other opacity sources like CH or C_2 have even smaller particle densities in the region of the model sequence across the $(T, n_{<H>})$ plane.

Jørgensen & Johnson (1992) investigated the radiative acceleration, $a_{\rm rad}$, in evolved AGB stars. They showed that for stars of similar stellar parameters as in Fig. 4.3, $a_{\rm rad}$ is larger for carbon-rich than for oxygen-rich models if $C/O > 1.35$ due to the increased amount of polyatomic molecules (C_2H_2, C_3, HCN). They conclude that M-type stars will always have small $a_{\rm rad}/g$. The same can be concluded from our investigations.

If the gravitational acceleration inwards equals the radiation acceleration outwards, the so-called Eddington limit is reached: $\alpha = a_{\rm rad}/g = 1$. The fact that positive pressure gradients can occur in hydrostatic model atmospheres indicates that $\alpha > 1$ does not necessarily mean an outflow of atmospheric material as long as the system is able to compensate the increasing radiative acceleration.

However, two important questions arise from these results: 1) Are pressure inversions in static atmospheres an artifact of the implied hydrostatic equilibrium? 2) Are pressure inversions stable solutions or rather unstable?

The following arguments indicate that local pressure inversions can be stable against perturbations and that they are very likely not an artifact of hydrostatic equilibrium:

- In dynamical computations, to be shown in Sect. 4.3, gas pressure inversions persist even if the atmosphere is perturbed by a piston acting at the inner boundary.

- In pressure inversions, also the direction of total local acceleration is reversed. Therefore, the criteria for a Rayleigh-Taylor instability [12] are not fulfilled (see the stability analysis by Wentzel 1970).

In fact, similar inversions have been observed in the inner parts of non-grey hydrogen-deficient hydrostatic model computations (Asplund et al. 1996) but also in the inner regions of non-grey metal-poor hydrostatic model atmospheres with solar hydrogen abundance (Helling 1996, e.g. Figs. 6.2., 6.22.). In all these models, the positive pressure gradient stabilizes the atmosphere which locally exceeds $\alpha = 1$. Asplund et al. (1996) explain the occurrence of gas pressure inversion in their models by the high continuum opacity and the occurring density inversion by a decrease of the molecular

[12] Rayleigh-Taylor instabilities occur if a medium 1 with a density ρ_1 is supported by a medium 2 with a density ρ_2 in a gravitational field ($\rho_1 > \rho_2$), or equivalently, when a heavy medium is accelerated by a light medium. Rayleigh-Taylor instabilities are known from a wide range of astrophysical phenomena and/or objects, e.g. accretion onto compact objects, supernova explosions or shock waves interacting with interstellar clouds (see for instance Jun et al. 1995 or Jun et al. 1996).

weight, both in the He ionization zone. The density inversion in our models is a direct consequence of the gas pressure inversion as we assume a constant molecular weight.

> Therefore, the occurrence of *local* gas pressure inversions does not violate the global assumption of hydrostatic equilibrium, since the locally increased gas pressure is stabilized by surrounding material with smaller opacity, and the gas pressure vanishes at infinity as demanded for physical reasons (see Sect. 4.1.4).

Achmad et al. (1997) reach the same conclusion regarding the stability of gas pressure inversions for stationary model computations of line-driven winds of supergiants.

Jørgensen & Johnson (1992) argued, however, that according to the presently available opacity data frequency-dependent cool star model atmospheres can not produce $\alpha > 1$. They state that a serious problem is the quality of the absorption coefficients and the neglect of practically unknown absorption coefficients from abundant molecules like C_2H and C_3H. Furthermore, it was assumed - like in every static model computation - that the line center frequencies are constant at every depth in the atmosphere. Jørgensen & Johnson (1992) concluded that in a dynamic atmosphere the value of the integral in Eq. (4.6) would be larger because large χ_ν would continuously be shifted to neighboring higher values of H_ν. Hence, $a_{\rm rad}$ is larger in a dynamical atmosphere than in a static atmosphere, because large absorption coefficients may be combined with high flux values. Such a behavior can approximately be simulated by using Planck mean gas opacities instead of Rosseland mean gas opacities as it is done in this work (see Sect. 1.2, Sect. 3.1.1.1).

Furthermore, Jørgensen & Johnson (1992) calculated models with artificially increased molecular absorption (factor of 5 to 7) where they found that the maximum α increases from 0.15 to larger than 1 for models with $T_{\rm eff} = 2500{\rm K}\ldots2800{\rm K}$, $\log g = -1.0$, and C/O=2.0. For a model $T_{\rm eff} = 3100{\rm K}$, $\log g = -0.5$, and C/O=2.0 a factor of 10 would be needed to increase α to values larger than 1.

The intention of this work is not to argue for a mean opacity treatment as an adequate substitution of detailed radiative transfer calculations. Instead, Planck means can simulate the increase of $a_{\rm rad}$ due to strong molecular absorption, and we can learn much about the influence of molecules on the atmospheric structure from such models. Models calculated with Planck mean gas opacities are therefore considered as an **upper limit** for such effects. In contrast, models computed with Rosseland mean gas opacities, which are by their nature smaller than Planck means, are considered as the **lower limit** for the molecular influence on the thermodynamic and hydrodynamic structure.

4.3 Molecular opacities in time-dependent, hydrodynamic model atmospheres

The photospheric and the inner atmospheric regions of late type stars are too hot for grain nucleation to take place but cold enough that a wide variety of molecules can be present in contrast to hotter stars where atoms and ions determine the chemical situation. The gas composing the atmosphere and the circumstellar envelope is the reservoir of molecular species for possible dust formation. The species involved in the dust formation process differ for different element compositions of the gas (see Table 4.3). In addition, the species important for dust formation can generally differ from those which determine the thermodynamic and hydrodynamic structure of those atmospheric regions where no dust is present. Species, which do not serve as dust condensate but as gas opacity source, are closely correlated to the dust formation process by their capability of blocking the outgoing radiation, causing a backwarming and determining the local temperature or being even the cause for damping of outwards propagating shock waves, as will be shown later.

To which extent molecular absorption may influence the thermodynamic and the hydrodynamic structure, and thereby may modify the amount of dust formed in circumstellar shells of cool star, shall be investigated in the following. Further, the question will be discussed whether pressure inversion regions caused by very large molecular absorption are an artefact of the requirement of the hydrostatic equilibrium, as it might seem possible from the results of Sect. 4.2, or if they persist also in a freely moving medium and even under pulsational disturbances.

	Molecular species in different chemical compositions determining in models of circumstellar dust shells	
	the atmospheric structure	the dust formation
C/O> 1	CO, CH, CN, C_2, C_3, HCN, C_2H_2, H_2, H_2^-, H_2^+	C_N, C_2H, C_2H_2, PAHs [a]
C/O< 1	CO, TiO, SiO, H_2O, H_2, H_2^-, H_2^+	seeds [b]: TiO_2 mantle [b]: $Al_6Si_2O_{13}$, Al_2SiO_5, Al_2O_3, $MgSiO_3$, $MgSiO_3$, Fe_3O_4, Fe_2O_3, FeO, Mg_2SiO_5,SiO_2, TiO_2, $MgSO_4$, MgS, SiS_2

Table 4.3: Molecular species determining the atmospheric structure and those which are important for dust formation

[a] Goeres (1993)
[b] Jeong et al. (1999)

The transport coefficients enter the system of equations (Sect. 4.1) in the equation of motion via the *radiative acceleration* ($\alpha \sim \chi_H$) and in the temperature equation in the *optical depth* ($\tau \sim \rho\chi_H$) since the models studied here are computed in the grey approximation. Although the grey approximation is a severe assumption compared to an ideally time-dependent model which includes the solution of the frequency dependent radiative transfer problem for atoms, ions, molecules, and dust, the molecule's influence can still be investigated with special regard to the velocity field and the density structure of the circumstellar shell. In addition, the influence of the molecular opacity on the dust component can be studied since the dust growth depends on the local density.

The time-dependent hydrodynamic models were computed using the CHILD[13] code introduced by Fleischer (1994) applying the Unno-Kondo method (Sect. 4.1.2) for the temperature determination (Winters et al. 1997). The code was extended as described in the previous chapters. It was further assumed that $\kappa_{\mathrm{J}} = \kappa_{\mathrm{Planck}}$, $\chi_{\mathrm{H}} = \kappa_{\mathrm{Planck}}$ or $\chi_{\mathrm{H}} = \chi_{\mathrm{Ross}}$ or $\chi_{\mathrm{H}} = const$, respectively. The Planck and the Rosseland mean gas opacities have been calculated on the basis of the Copenhagen molecular opacity data (Chap. 2). The dust mean gas opacities are the same for all models, namely the Rosseland mean dust opacity given in Gail & Sedlmayr (1985).

[13] Conventional Hydrodynamic Including Lacking Dust

4.3.1 The radial structure of time-dependent model atmospheres with strong molecular opacities

The hydrodynamic and the thermodynamic structure of a time-dependent carbon-rich model computed with Planck mean gas opacities will be discussed in the following aiming on a comparative study to time-dependent models of circumstellar, dust-dominated envelopes with a weaker molecular opacity component as presented by Fleischer et al. (1992).

Figure 4.6 depicts the radial structure of the exemplarily chosen hydrodynamic wind model with

$$
\begin{array}{llll}
\mathrm{T}_\star & = 3000\mathrm{K} & R_{\mathrm{inner}} & = 0.91\,R_0 \\
\mathrm{M}_\star & = 1\,\mathrm{M}_\odot & \Delta u & = 2\mathrm{km/s} \\
\mathrm{L}_\star & = 10^4\mathrm{L}_\odot & P & = 650\mathrm{d} \\
\mathrm{C/O} & = 1.8 & &
\end{array}
$$

for four instants of time, each at a full period. The quantities are plotted as function of the radial position R in units of the initial stellar radius R_0 (the stellar radius of the initial hydrostatic model).

The different panels of Figure 4.6 (top-down) are organized as follows:

1$^{\mathrm{st}}$ panels	left axis	local velocity u in km/s (solid)
		escape velocity[14] u_{esc} in km/s (dash-dot)
		isothermal sound velocity [15] u_{cs} in km/s (dotted)
	right axis	gas temperature T_{gas} in 10^3K (dashed)
2$^{\mathrm{nd}}$ panels	left axis	logarithmic gas density ρ in g/cm^3 (solid)
	right axis	degree of condensation f_c in % (dashed)
		(amount of condensible material actually condensed into grains, 1 is maximum, 0 is minimum)
3$^{\mathrm{rd}}$ panels	left axis	logarithmic nucleation rate J_* relative to the total hydrogen abundance $n_{<\mathrm{H}>}$ in 1/s (solid)
		(number of dust grains formed per second and per H-atom)
	right axis	logarithmic number of dust grains per H-atom $n_{\mathrm{d}}/n_{<\mathrm{H}>}$ (dashed)
4$^{\mathrm{th}}$ panels	left axis	local radiative acceleration relative to the local gravitational acceleration α^{tot} (solid) = α^{g} (dotted) + α^{d} (dashed)
	right axis	logarithmic optical depth τ (dash-dot)

[14] The term *escape velocity* u_{esc} originates from consideration of a free falling particle in a gravitational field. The original definition does not include interactions between particles as pressure gradients indicate. Therefore, the classical escape velocity calculated from $1/2\,m\,u^2 = G\,m\,M/r$ should rather be considered as only an upper limit of the velocity a parcel containing a mass m has to reach in order to escape the gravitational field of the star.

[15] Note, the isothermal *sound velocity* $u_{\mathrm{cs}} = \sqrt{(\partial p/\partial \rho)|_{T=const}}$ originates from a different hydrodynamic concept, namely, the stationary case of hydrodynamics where $u(r) = u_{\mathrm{cs}}(r)$ indicates a critical (singular) point of the wind equation beyond which the mass is only accelerated.

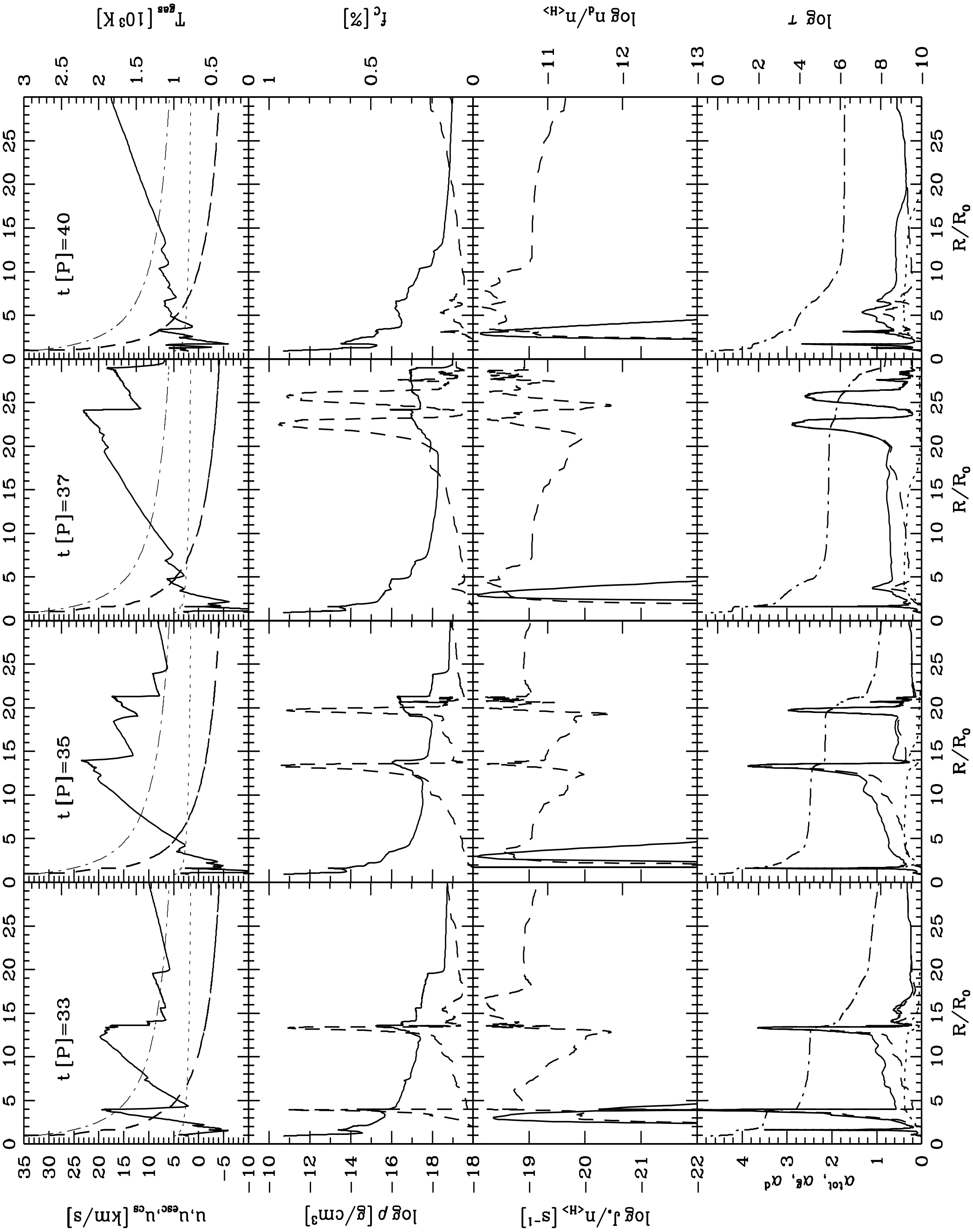

Figure 4.6: A carbon-rich time-dependent model computed with Planck mean gas opacities. Shown are four different instants of time: periods 33, 35, 37, 40. The **model parameters** are: $T_\star = 3000$K, $M_\star = 1M_\odot$, $L_\star = 10^4 L_\odot$, C/O = 1.8, $R_{\rm inner} = 0.91\,R_0$, $\Delta u = 2$km/s, $P = 650$d.

The radial structure can generally be distinguished into two regions: an dust-free inner region, where dust nucleation has not yet taken place, and a dust dominated, radiatively accelerated wind region. In the inner region, a density inversion occurs at $R \approx 2\,R_0$ where the molecular opacities cause $\alpha^{\rm tot} > 1$. Shock waves generated by stellar pulsation levitate the atmosphere at some larger distances. The inner region below $\approx 2.5\,R_0$, the molecular domain, will be discussed in more detail in Sect. 4.3.1.1. In this section, we will concentrate at the outer circumstellar shell regions:

The most striking features in the wind region of a typical time-dependent model including dust formation are the strong shocks running through the atmosphere with velocity "jumps" of up to $\Delta u \approx 20\,{\rm km/s}$ (Fig. 4.6). Distinct layers, which contain large amounts of dust, can form in the wake of these shocks.

Dust nucleation and growth: The figure shows the dust formation event occurring from time to time in the model (see also Sect. 4.3.3). Dust nucleation starts at $\approx 2.5\ldots4.5\,R_0$ where the temperature is low enough. Therefore, the nucleation rate $J_*/n_{<\rm H>}$ approaches a maximum of $\approx 2.5\,10^{-19}\ldots10^{-18}\,{\rm s}^{-1}$ (solid line, 3$^{\rm rd}$ panels), and consequently, the number of dust particles per hydrogen atom $n_{\rm d}/n_{<\rm H>}$ increases (dashed line, 3$^{\rm rd}$ panels). The degree of condensation f_c approaches almost 90% already at $\approx 4\,R_0$ in period 33 (dashed line, 2$^{\rm nd}$ panel, 1$^{\rm st}$ column). The out-going shock ($\approx 4\,R_0$, period 33) compresses the gas and therefore, an efficient dust growth takes place. Not at every full period a dust layer forms in this model as can be seen by comparing periods 33, 35, 37, and 40, although the temperature is low enough that nucleation could take place.
At periods 37 and 40 one observes the formation of small dust layers at $\approx 4\ldots6\,R_0$ with a smaller degree of condensation ($\approx 10\%\ldots20\%$). The last panels in Fig. 4.6 shows that such a degree of condensation of $\approx 20\%$ is already enough to cause $\alpha^{\rm tot} > 1$ at small radial distances but outside the molecular domain resulting in small disturbances of the velocity field.

Dust enhanced shocks: The increasing amount of dust causes an increasing dust opacity (dashed line, lowest panels), therefore an increasing total radiative acceleration $\alpha^{\rm tot}$ (solid line, lowest panels). Since the grains are closely momentum coupled to the gas, the sudden increase of the radiative acceleration at $R \approx 4\,R_0$ (period 33) amplifies the acceleration of the gas such that the shock wave is gaining strength and increases in amplitude (compare periods 33 and 35). The result is an increasing compression ratio of the shock which supports further dust growth. Therefore, the coupled system of dust formation, shock propagation and gas compression is self-amplifying. In the wake of the shocks the density gradient is small which prohibits the steepening of subsequent waves.

Propagating shocks & shell cannibalism: Regarding Fig. 4.6 as four subsequent instances of time (periods 33, 35, 37, 40) gives a picture of the shocks and the dust shells traveling outwards. In the first column (period 33), a dust layer at about $3.5\,R_0$ has just developed. Another shell at $R \approx 13\,R_0$ in period 33 ($R \approx 22\,R_0$ in period 35) has formed at an earlier instant of time. The shock at $R \approx 21\,R_0$ in period 35 was originally correlated to the dust shell at $R \approx 22\,R_0$ and now divides into two different parts: one moving further outwards with a smaller amplitude and another one occurring as a reflected wave. The outwards moving part occurs at $R \approx 29\,R_0$ in period 37 at larger distance from the star than the dust shell, therefore, dust shell and shock are now de-coupled. In the 3rd column of Fig. 4.6 (period 37) the instant of time is shown where the subsequent shock which developed at period 33 has merged at about $24\,R_0$ with the reflected wave.

The dust layer which developed in period 33 travels faster than the elder one, which is located at $\approx 26\,R_0$ in period 37, because the efficiency of the dust opacity regarding the radiative acceleration decreases with increasing radii. These two dust shells merge and appear to move outwards together (compare period 40).

Dust and gas opacity fractions: The radiative acceleration (full line, last panels) is directly proportional to the total flux weighted mean opacity (see Eq. (4.8)) and one can evaluate the relative contribution of molecules and dust.
Molecules (dotted line, last panels) are the main opacity source in regions close to the photosphere up to about $\approx 2\,R_0$ (molecular domain) whereas dust (dashed line, last panels) totally dominates the radiative acceleration in the dust layers (dust domain). Between the dust layers, molecules provide an opacity background in addition to the dust whose actual contribution depends on the amount of condensed material. Beyond $r \gtrsim 15\,R_0$, the relative contribution of molecules to the total radiative acceleration becomes negligible (compare last panels Fig. 4.6).
The occurrence of strong opacity features is traceable by the course of the optical depth τ (dash-dot line, last panels). At each time and at every site where a strong opacity source is present in the atmosphere, the optical depth strongly decreases.

4.3.1.1 Comparison to the initial static model

Figures 4.7 and 4.8 depict 10 instants of time of the *inner region* of the wind model discussed before (in black), together with the initial static model (in grey).

The different panels of Figs. 4.7 and 4.8 (top-down) are organized as follows. All quantities are plotted as function of the radial position R in units of the initial stellar radius R_0.

1st panels	both axes	gas temperature T_{gas} in 10^3K (solid)
2nd panels	left axis	logarithmic gas density ρ in g/cm^3 (solid)
	right axis	local velocity u in km/s (solid)
		isothermal sound velocity u_{cs} in km/s (dotted)
3rd panels	left axis	logarithmic total opacity χ^{tot} in cm^2/g (solid)
	right axis	logarithmic gas opacity χ^{g} in cm^2/g (dotted)
		logarithmic dust opacity χ^{d} in cm^2/g (dashed)

The time series depicted in Figs. 4.7 and 4.8 shows that the passing shocks at $R \lesssim 1.8\,R_0$ cause a modulation of the density-temperature structure which varies around that of the corresponding initial hydrostatic model. Here, the pressure gradient is large enough to dominate the equation of motion such that shocks occur only as small disturbances of the system. Further out at $R \gtrsim 2\,R_0$, the shocks levitate the atmosphere providing a larger density than the hydrostatic model at every time. The enhanced density leads to favorable conditions for the dust growth.

Only at full and half piston period (periods 43, 43.5, 44) the temperature structure of the time-dependent model resembles the initial static temperature structure

fairly well because at these times the stellar radius approximately coincides with R_0. Further differences are caused by the backwarming effect: the blocking of outgoing radiation by a layer of strong molecular absorption leads to a subsequent heating of the material at smaller radii. The time-dependent model has a higher density at those radial distances which causes a stronger backwarming as a consequence of a larger $\rho\chi^{\rm tot}$ (see Eq. (4.17)).
The density structure at periods 43, 43.5, 44 is, since $R_\star \approx R_0$, very similar to the static model up to about $1.1\,R_0$ until the first shock compresses and sweeps up the gas. The density of the dynamic model is larger than the density of the static model when the piston moves outwards (periods 43.15, 43.3, 43.4, Fig. 4.7) unless some mechanism causes a density inversion. Subsequently, the stellar radius is larger and therefore the time-dependent model is hotter at the same radial position compared to the static model.

While the piston moves back to its rest position (periods 43.7, 43.9, 43.95, Fig. 4.8), matter falls inwards and the density decreases below that of the initial model unless shocks or some other mechanism cause a net-outward movement. As the stellar radius becomes smaller, the temperature decreases below that of the static model.

At rest position of the piston (period 43, 44), a density inversion develops in the innermost regions of the dynamic model. At these instants of time, the opacity peaks of the dynamic and the static model occur at similar radial position with similar hight. Also here, differences in the strength of the total opacity occur if shock waves alter the density structure.

4.3.1.2 The very inner radial structure of time-dependent hydrodynamic model atmospheres with a strong molecular opacities

Investigations of the initial hydrostatic models (Sect. 4.2) have shown that strong molecular absorption can forces a physical system to stabilize its state by locally increasing the gas pressure. The interplay between such strong molecular absorption and small scale pulsations of the order of 1 km/s will therefore be investigated in this subsection.

In the Figures 4.7 and 4.8, 10 successive snap shots of the inner region ($R < 2.5\,R_0$) are shown in order to illustrate the on-going physical processes in the molecule dominated region of a time-dependent model atmosphere. The time sequence shown in Figs. 4.7 and 4.8 starts with Fig. 4.7 at full period (43) where the velocity of the piston is maximum.

A general feature of the inner atmospheric regions of time-dependent carbon-rich models is a large gas opacity peak at $R = 1.5 \ldots 2\,R_0$ (lower panels) which results from strong local molecular absorption. The arising radiative acceleration is strong enough to cause an acceleration of the gas in period 43 (left column, Fig. 4.7) at $R = 1.6\,R_0$ resulting in a new outwards traveling wave. This wave has been formed at earlier times and has already increased its amplitude to about 6 km/s. It runs into the pressure inversion region with larger densities at $\approx 1.7\,R_0$; also a result of the strong opacity. 0.15 periods later (period 43.15) the wave has become a shock and is partly transmitted through this dense region. The transmitted part of the shock ($\approx 2\,R_0$, period 43.3) increased its amplitude due to the large negative density gradient beyond $1.8\,R_0$. It travels further out in the atmosphere until it strengthens

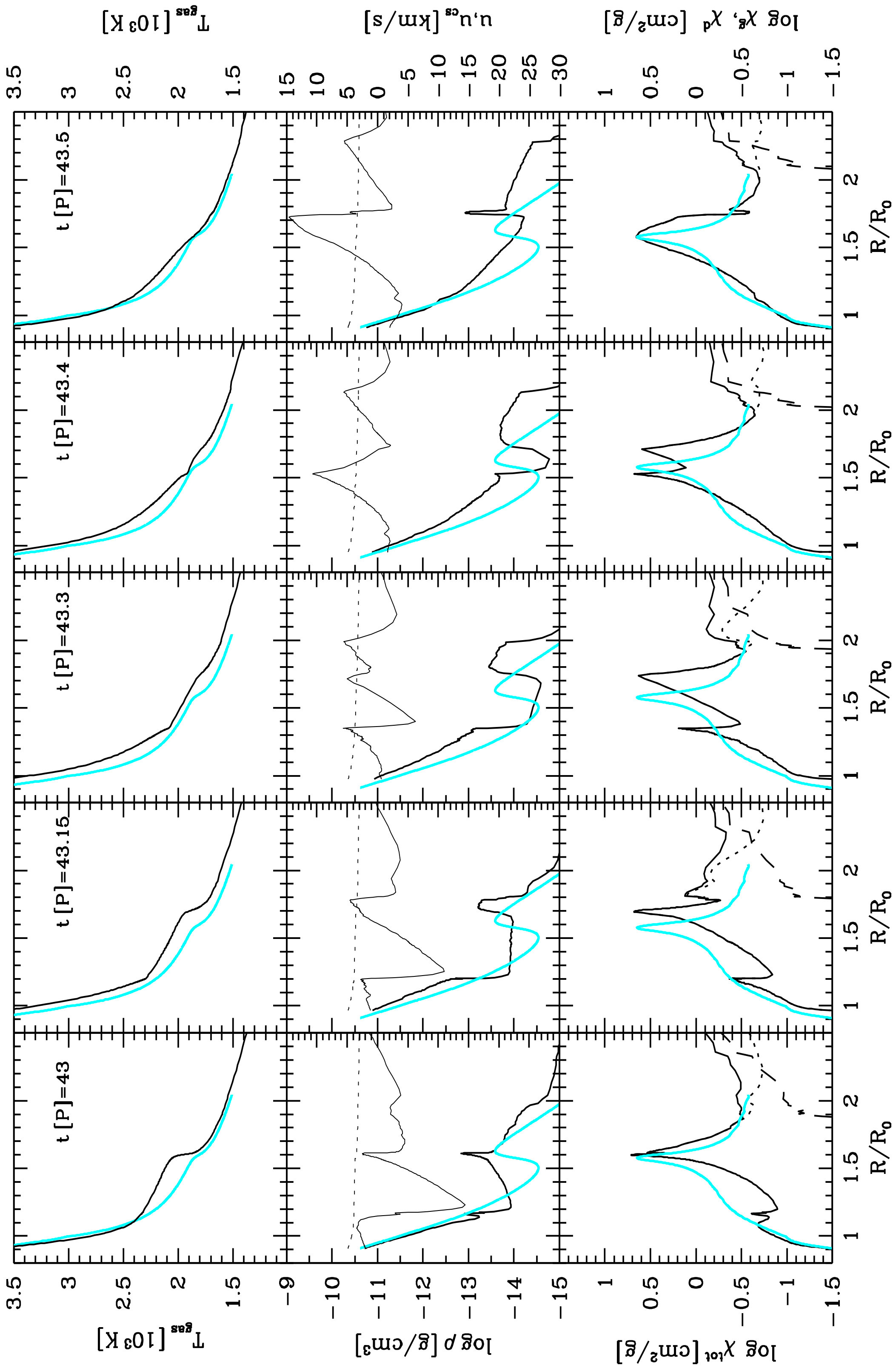

Figure 4.7: Very inner radial structure of a carbon-rich time-dependent model computed with Planck mean gas opacities. The **model parameters** are: $T_\star$ = 3000K, $M_\star = 1M_\odot$, $L_\star = 10^4 L_\odot$, C/O = 1.8, $R_{\text{inner}} = 0.91\,R_0$, Δu = 2km/s, P = 650d (cf. Fig. 4.6).

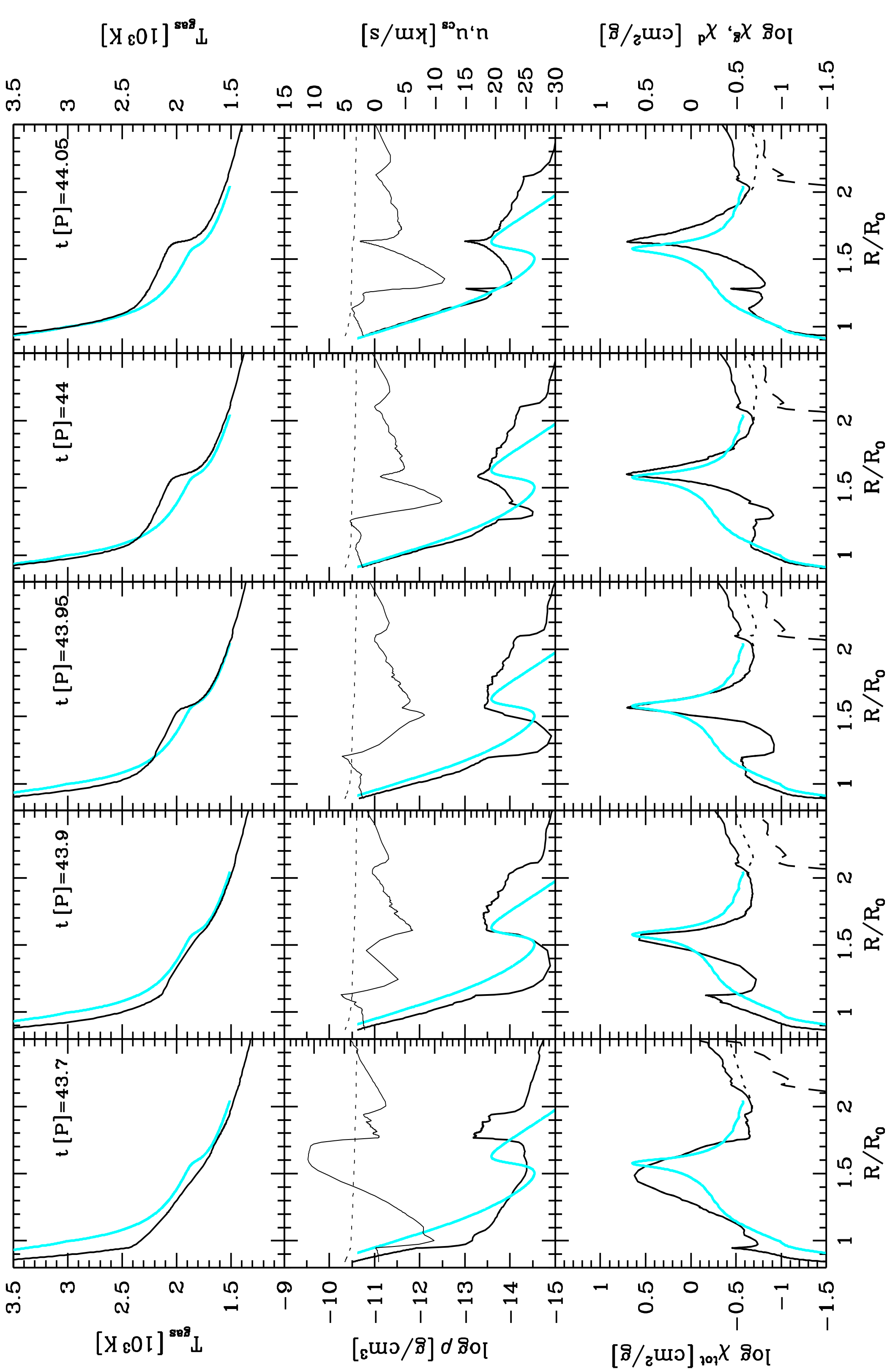

Figure 4.8: Fig. 4.7 continued

by radiative pressure on dust which will happen at a radial position $> 2.5\,R_0$. In addition, a reflected wave occurs at about $1.7\,R_0$ (partial wave reflection) traveling as wave backwards to the star.

A new shock front has developed as a result of the interior pulsation. The wave, introduced by the piston, steepens while running down the almost exponential photospheric density gradient (compare $R < 1.5\,R_0$ in periods 43, 43.15, and 43.3). In period 43.4, this shock has overrun the reflected wave which developed in period 43.3 at $1.7\,R_0$. The photospheric gas which was passed by this shock is left with high density as can be seen from a comparison of periods 43.15, 43.3, 43.4, and 43.5 with the density of the initial static model (in grey).

The new shock, at $\approx 1.55\,R_0$ in period 43.4, has levitated the gas and the temperature is low enough that the gas enters the domain of strong molecular absorption ($\approx$ 1750K... $\approx$ 2000K) resulting in the new opacity peak at similar radial position.

The negative sign of the hydrodynamic velocity u (middle row) indicates that gas also falls back towards the star in the inner regions of the atmosphere (e.g. at $R = 1.75\,R_0$, period 43.5). Therefore, the very sharp density peak at $R \approx 1.72\,R_0$ in period 43.5 results from a collision of infalling material with material being accelerated outwards. Note that THIS density peak cannot result from any strong absorption because the strongest absorption is located elsewhere, but it can, however, cause the increase of the opacity. Shock transmission and partial wave reflection occur again at periods 43.7 and 43.9. Thereby, the gas moves outwards and the density peak broadens to a plateau with outwards decreasing slope causing an acceleration of the transmitted shock (period 43.7).

The hydrodynamic and the shock velocities[16] are clearly supersonic in periods 43.5 and 43.7 as shown by a comparison with the velocity of sound (dotted lines, middle rows, Figs. 4.7, 4.8). Now, in period 43.9 no strong shocks with velocities greater than the sound velocity are present in the depicted radial interval and the gas flow is mainly subsonic. Still, a region of high density occurs, between $1.6\,R_0$ and $2.1\,R_0$ in period 43.9. Strong radiative acceleration by molecules causes the formation of this density inverted layer also in time-dependent models. The density inversion is present at every instant of time and is altered depending on the strength of the propagating shocks. In turn, the positive density gradient damps and partially reflects the shock waves when they enter into this region.

In period 43.95 a small wave with an amplitude of about 2 km/s occurs at $R \approx 1.58\,R_0$ corresponding to the large opacity peak at the same radial distance. This new wave is NOT caused by the stellar pulsation but is a result of radiation pressure on molecules. The wave's amplitude increases to about 4 km/s in period 44. At the same time, infalling matter moves towards the star causing a tiny density peak at $R \approx 1.4\,R_0$ (period 44). The material forms an accretion shock. The gas is compressed while moving upward the density gradient as can be seen from period 44.05 (compare with period 43). The increased density peak at about $1.3\,R_0$ is the reason for the new opacity peak at the same radial position. It seems that a mutual interaction between both takes place as it is very difficult to separate cause from effect.

The existence of strong molecular absorption in the innermost regions of pulsating atmospheres is also visible from the course of the temperature gradient which shows

[16]The shock velocity is approximately given by the difference between the pre-shock and the post-shock velocities.

the effect of backwarming appearing as steps in the temperature.

In this section, the influence of strong molecular absorption on the structure of time-dependent models of circumstellar shells has been outlined in the frame of upper limit consideration since the exemplary model which has been discussed was calculated applying Planck mean gas opacities. The effect of different strength of molecular absorption will be considered in the next section.

4.3.2 Comparison to hydrodynamic models with weak molecular opacities

In this section, time-dependent models of circumstellar shells are compared for which different treatments of the gas opacities have been applied. In particular, Planck models are discussed in contrast to models calculated with Rosseland means and with a constant gas opacity value. The two latter cases serve as the lower limit for the influence molecular absorption can have on the structure of a circumstellar shell.

4.3.2.1 Time-dependent Planck mean and Rosseland mean gas opacity models

Figure 4.9, which is arranged like Fig. 4.6 (Sect. 4.3.1), shows two models for the following set of parameters (model E in Fleischer et al. 1992):

$$\begin{array}{llll} \mathrm{T}_\star & = 2600\mathrm{K} & R_{\mathrm{inner}} & = 0.91\,R_0 \\ \mathrm{M}_\star & = 1\,\mathrm{M}_\odot & \Delta u & = 2\mathrm{km/s} \\ \mathrm{L}_\star & = 10^4\mathrm{L}_\odot & P & = 650\mathrm{d} \\ \mathrm{C/O} & = 1.8 & & \end{array}$$

The models, of which one is computed with Planck mean gas opacities (left column) and one with Rosseland mean gas opacities (right column), are depicted at the same instant of time at half piston period.

A first glance on Fig. 4.9 shows that in both models shocks and well seperated dust shells develop (1^{st} and 2^{nd} panels) but that dust formation is more efficient in the model computed with Rosseland mean gas opacities (3^{rd} panels) since the gas density is larger. In both models, an inner region below $2\,R_0$ exists where no dust is present. As soon as the temperature is low enough, dust can form and it dominates the total opacity and therefore the radiative acceleration in both models (4^{th} panels).

The inner, photospheric density structure ($R < 2\,R_0$) of the Planck model exhibits a density inversion which does not exist in the model computed with Rosseland mean gas opacities (2^{nd} panels, solid line in Fig. 4.9). Because of the monotonically decreasing density without an inversion in the inner regions, shock waves propagate outwards more easily in the Rosseland model (1^{st} row, solid line).

Dust nucleation takes place in almost the same radial zone in both models (3^{rd} panels, solid line) and consequently, the number of dust particles steeply increases at about $2\,R_0$ (3^{rd} panels, dashed line). However, an inspection of the 2^{nd} and 3^{rd} panels in Fig. 4.9 shows that the dust growth has a larger efficiency in the Rosseland model according to the the larger number of shells formed.

In the model computed with Planck mean gas opacities the dust growth sets in at a slightly larger radial distance ($R \approx 3\,R_0$, 2^{nd} panels) than the nucleation ($R \approx 2\,R_0$,

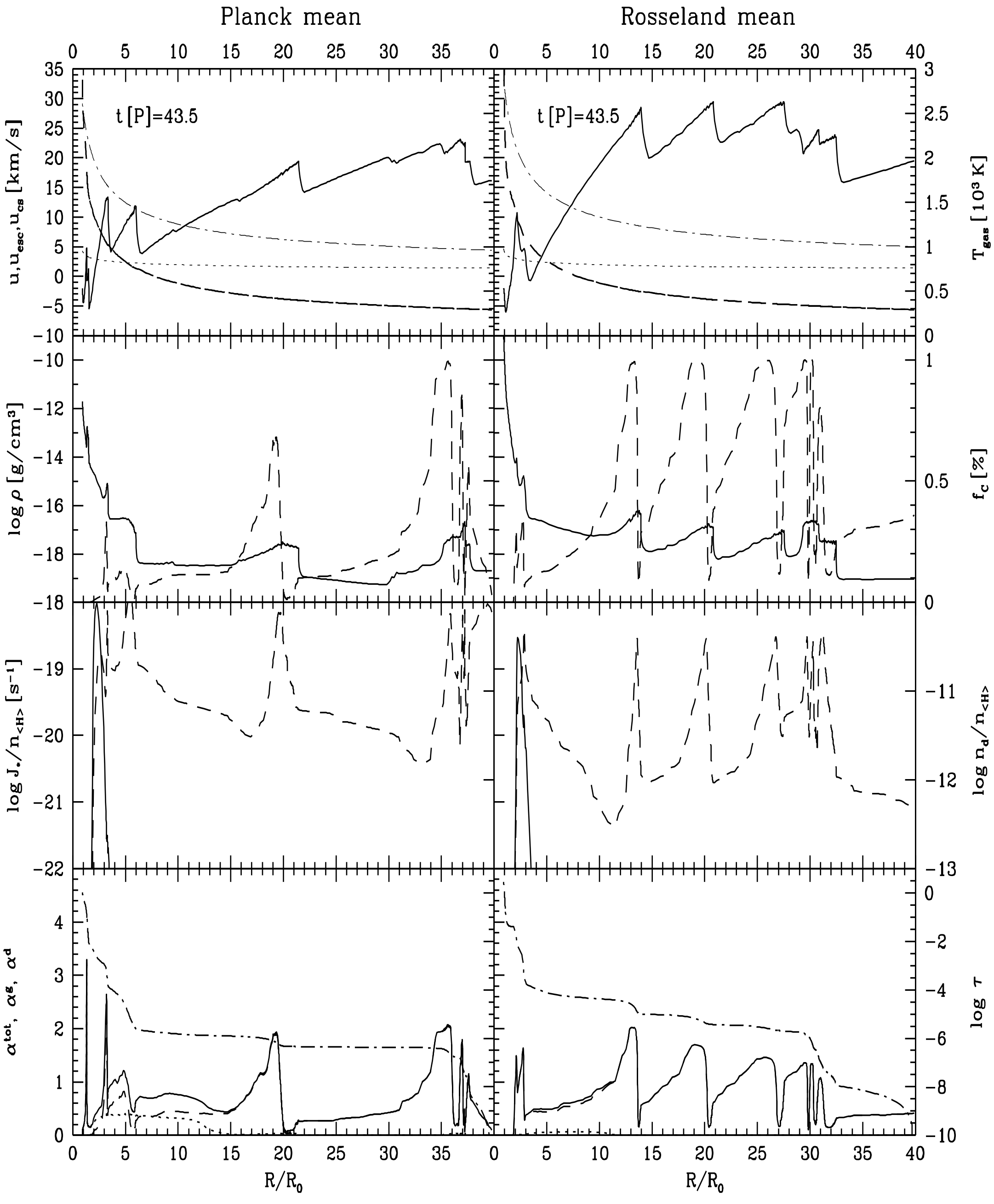

Figure 4.9: Comparison of carbon-rich time-dependent models computed with Planck mean (left column) and Rosseland mean (right column) gas opacities. The **model parameters** are: $T_\star = 2600$K, $M_\star = 1M_\odot$, $L_\star = 10^4 L_\odot$, C/O = 1.8, $R_{\rm inner} = 0.91\,R_0$, $\Delta u = 2$km/s, $P = 650$d.

3$^{\text{rd}}$ panels) in contrast to the Rosseland model. The newly formed dust introduces in both cases a perturbation into the velocity field. This leads either to an increase of the amplitude of a shock wave which originates from the interior pulsation or to an additional velocity peak purely caused by radiation pressure on dust.

In general, a model computed with Planck mean gas opacities exhibits an atmosphere which is less dense than a Rosseland mean model (see also Sect. 4.2) causing a less efficient dust growth. Therefore, the degree of condensation is almost always smaller than in a model computed with Rosseland mean gas opacities. Only at large distances ($R \approx 30\,R_0$) the dust particles in the wake of a shock had enough time that the degree of condensation can reach almost 100%. In the models computed with Rosseland mean opacities, the degree of condensation reaches 100% already at $\approx 10\,R_0$.

In the Planck model, nucleation takes place at almost every instant of time because the previous dust shells are not so opaque to cause a backwarming strong enough to inhibit further dust nucleation. Therefore, dust is formed more continuously and the dust shells are not as well seperated as in the Rosseland models.

Inspecting the total radiative acceleration α^{tot} (4$^{\text{th}}$ panels, solid line) shows the dominance of the dust (dashed line) at $R > 2\,R_0$ in both models. The molecular opacity (dotted line) contributes to the total radiative acceleration only in the case of Planck mean gas opacities below $15\,R_0$ where it dominates below $2\,R_0$. The molecular opacity can contribute as much as the dust opacity between the dust shells (e.g. $R = 5\ldots12\,R_0$). In contrast, the Rosseland mean gas opacity is almost negligible compared to the total radiative acceleration in the same radial range (see small difference between dashed and solid curve, right column, lower panel).

It is interesting to note that the slope and magnitude of the radiative acceleration α^{tot} are very similar in both models at those sites where dust shells occur. This indicates that, once dust is formed, the processes which are responsible for the hydrodynamic and thermodynamic structure of a circumstellar shell are de-coupled from the gas and act therefore on a similar way in both models: radiation pressure on dust accelerates the gas by transfer of momentum by friction and thereby introduces strong shocks into the velocity field. The gas plays only the role of a passive component of the system if dust has formed in large amounts, or at large radial distances where the molecular opacity sources are present in only very small amounts.

The reason for the smaller hydrodynamic and the smaller shock velocity in a model computed with Planck mean gas opacities might be found from a closer comparative look at the inner regions of the models which will follow in the next section.

4.3.2.1.1 Inner radial structures Detailed results regarding the very inner regions of a time-dependent model computed with Planck mean gas opacities have been described in Sect. 4.3.1.2. Here, a comparison of the inner regions between the Planck model and the Rosseland model is depicted in Fig. 4.10 (arranged like Fig. 4.7).

The first difference between the Planck (two left columns) and the Rosseland (two right columns) model to be noticed is the occurrence of a backwarming at small radial distances due to stronger molecular absorption in the case of the Planck model. The temperature structures differ by $\approx 350\,$K below $1.5\,R_0$ but are comparable at $R > 1.5\,R_0$ until dust forms. Consequently, the temperature at the site of dust nucleation ($\approx 2\ldots3\,R_0$) is not affected and, therefore, nucleation sets in at almost

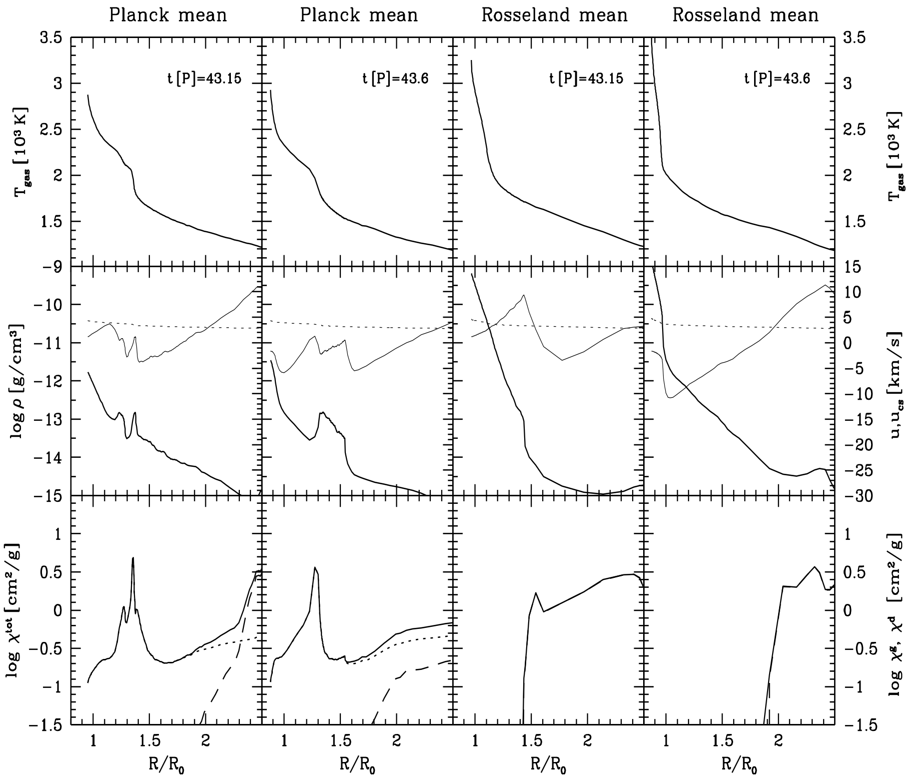

Figure 4.10: Comparison of the very inner regions of carbon-rich time-dependent models computed with Planck mean (two left columns) and Rosseland mean (two right columns) gas opacities. The **model parameters** are: $T_\star = 2600$K, $M_\star = 1M_\odot$, $L_\star = 10^4 L_\odot$, C/O = 1.8, $R_{\rm inner} = 0.91\,R_0$, $\Delta u = 2$km/s, $P = 650$d

the same radial distance from the star (Fig. 4.9, compare also Sect. 4.3.3).

Large differences between the models computed with Planck mean gas opacities and Rosseland mean gas opacities can be observed from the inner density and velocity structures. The reason for the different dynamical behavior is the different strength of the molecular absorption which reaches a maximum value of $\chi^{\rm g}/\rho \approx 6\,{\rm cm}^2/{\rm g}$ for the Planck mean gas opacities in contrast to $\chi^{\rm g}/\rho \approx 10^{-2}\,{\rm cm}^2/{\rm g}$ for Rosseland mean gas opacities. As it has already been described (Sect. 4.3.1.2), such a strong molecular absorption can introduce a perturbation into the velocity field and, even more important for the propagation of strong shocks, it can cause a density inversion in the inner regions. The result is a damping of the waves produced by the interior pulsation since these waves have to pass through a small region of increasing density. In contrast, the waves can increase the amplitude by moving outwards along the almost exponential, undisturbed density gradient in the Rosseland model and rapidly steepen into strong shock. Their amplitudes increase even more if dust formation takes place (last row, two left panels).

In the Planck model, the shocks are damped and only slightly increase their amplitude when running down the density gradient OUTSIDE the density inversion. If they are strong enough, they can pass through and enter the dust formation window (Gail & Sedlmayr 1998). Then, they continue traveling outwards, coupled to the dust shell, with an increased amplitude due to radiative pressure on dust. Thus, the amplitude of shocks occurring in a Planck model will be generally smaller than in a Rosseland model for the same stellar parameters.

4.3.2.2 Time-dependent Planck mean gas opacity models and models with a constant gas opacity

Figure 4.11, which is arranged like Fig. 4.6 (Sect. 4.3.1), compares Planck mean (left column) and constant opacity (right column) models with

$T_\star$	$= 3000\mathrm{K}$	R_{inner}	$= 0.91\,R_0$
$M_\star$	$= 1\ M_\odot$	Δu	$= 2\mathrm{km/s}$
$L_\star$	$= 10^4 L_\odot$	P	$= 650\mathrm{d}$
C/O	$= 1.8$		

at the same full piston period. The constant opacity is choosen to be $\chi^{\mathrm{g}}/\rho = 2 \times 10^{-4}\,\mathrm{cm}^2/\mathrm{g}$ according to Bowen (1988).

One may notice that the left column of Fig. 4.11 depicts a later instant of time of the model already shown in Sect. 4.3.1 (Fig. 4.6) when the merged dust shells already left the depicted radial range.

Strong shocks amplified by radiation pressure on dust (e.g. at $R = 3\,R_0$ and $R = 7\,R_0$, right column) and distinct dust shells with more than 90% carbon condensed into grains are typical for models with the small molecular opacity. In contrast, dust growth is not very efficient ($f_\mathrm{c} \lesssim 40\%$, dashed line, 2$^{\mathrm{nd}}$ panels) in the model with a strong molecular opacity due to the lower density as it has already been pointed out in Sect. 4.3.2.

Again, an inner region below $2\,R_0$ is present where no dust has formed in both cases at any time. Here, the Planck model exhibits a larger peak of radiative acceleration due to strong molecular absorption resulting in a density inversion (solid line, 2$^{\mathrm{nd}}$ panels, left column). The molecular opacity significantly contributes up to $\approx 18\,R_0$ to the total radiative acceleration in the Planck model, whereas no "visible" contribution occurs in the model with a constant gas opacity. The radiative acceleration in the small gas opacity model is caused purely by dust (4$^{\mathrm{th}}$ panels, solid, dotted, and dashed lines).

The waves generated by the internal pulsation are not damped in the model with a constant gas opacity and can therefore propagate easier outwards than in the Planck model, until the first dust shell forms. As the shocks are stronger and the densities higher, more material is compressed and dust can grow more easily than in the Planck model although in both models nucleation sets in at almost the same radial distance.

The effective dust formation in the model with a constant gas opacity causes a strong backwarming as can be seen from the step in the temperature at $R = 3\,R_0$ (1$^{\mathrm{st}}$ panels, right column, dashed line, Fig. 4.11). A similar effect can be observed for the Planck model at $R = 1.5\,R_0$ (see also Fig. 4.12) where the strongly absorbing gas is the cause of the backwarming effect (1$^{\mathrm{st}}$ panels, left column, dashed line).

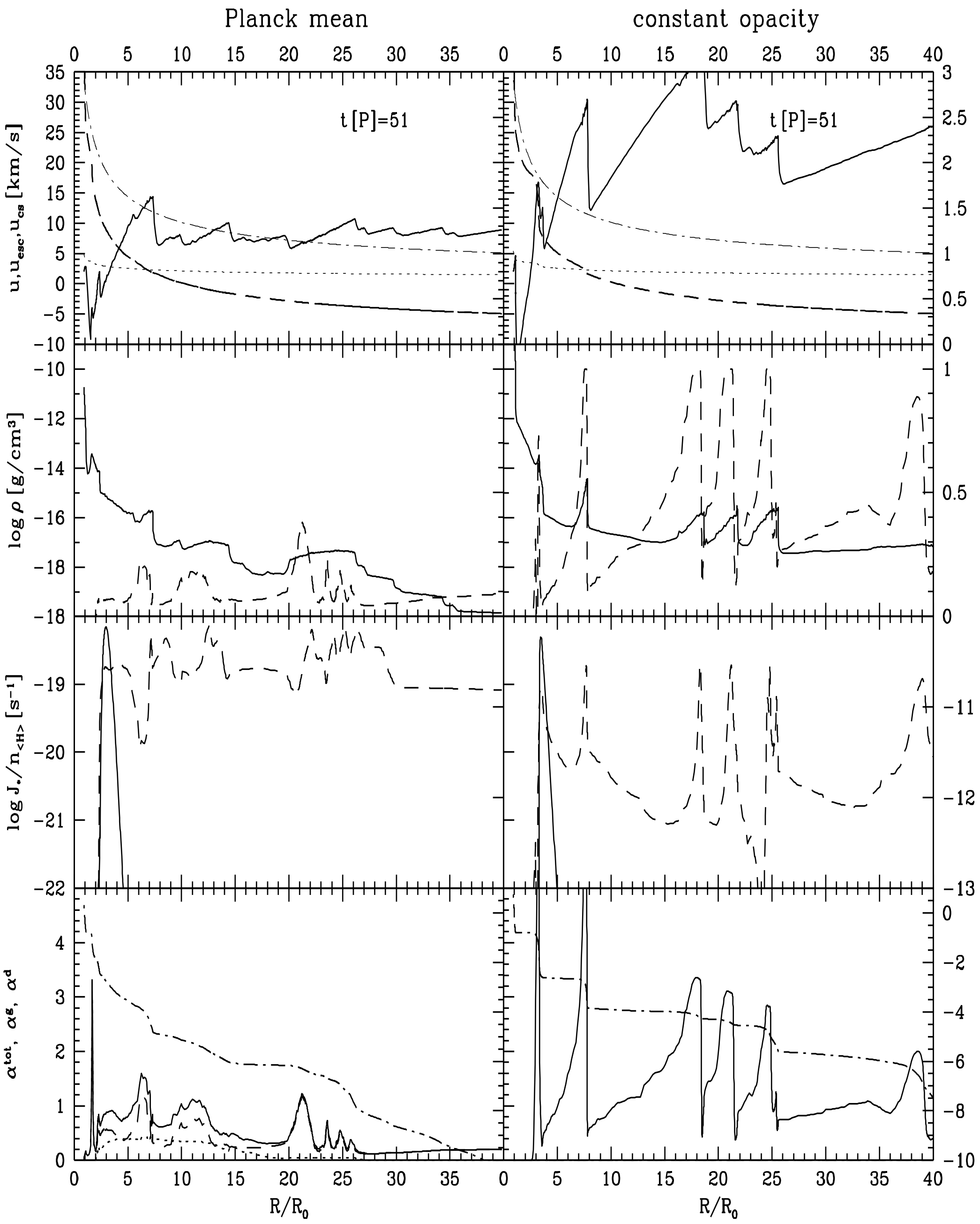

Figure 4.11: Comparison of carbon-rich time-dependent models computed with Planck mean gas opacities (left column) and with a constant gas opacity (right column). The **model parameters** are: $T_\star = 3000$K, $M_\star = 1M_\odot$, $L_\star = 10^4 L_\odot$, C/O = 1.8, $R_{\rm inner} = 0.91\,R_0$, $\Delta u = 2$km/s, $P = 650$d.

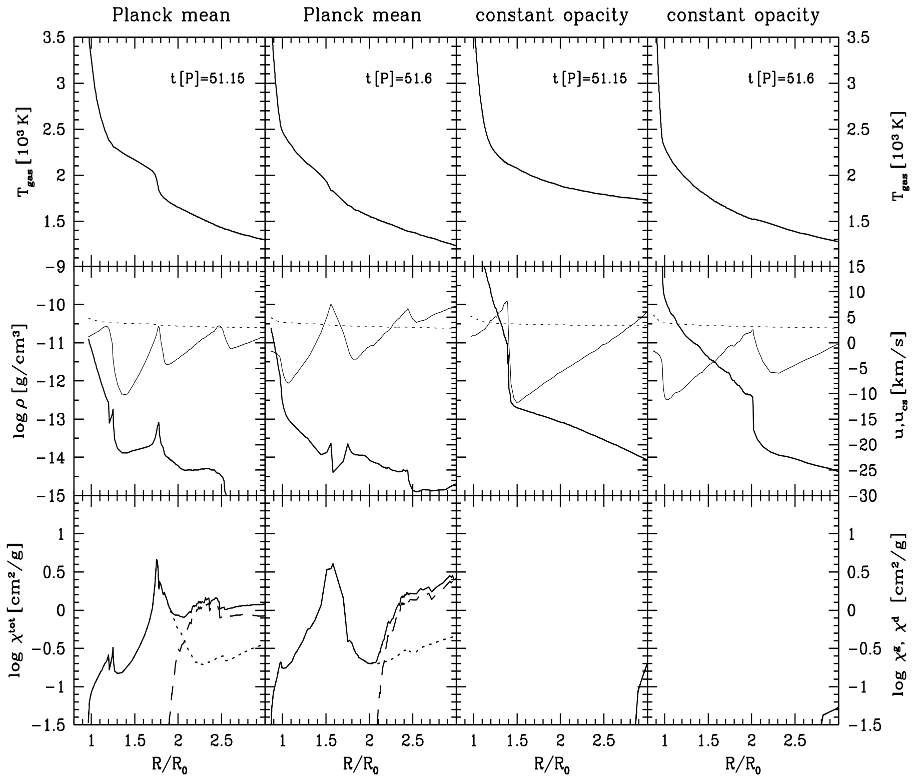

Figure 4.12: Comparison of the very inner regions of carbon-rich time-dependent models computed with Planck mean gas opacities (two left columns) and with a constant gas opacity (two right columns). The **model parameters** are: $T_\star = 3000\text{K}$, $M_\star = 1M_\odot$, $L_\star = 10^4 L_\odot$, $C/O = 1.8$, $R_{\text{inner}} = 0.91\,R_0$, $\Delta u = 2\text{km/s}$, $P = 650\text{d}$

4.3.2.2.1 Inner radial structures Figure 4.12 shows an enlargement of the inner region of the same models discussed before but at different instants of time.

The temperature structures of both models differ largely at period 51.15 where the Planck model shows a temperature step due to backwarming by molecules at $R < 2\,R_0$. The model with a constant gas opacity exhibits also the backwarming effect but due to dust which has just formed outside of the depicted radial range leading to a general temperature raise in the inner regions at period 51.15 (compare also dashed line at $R = 3\,R_0$ in Fig. 4.11, right column, 1$^{\text{st}}$ panel).

The inner density and velocity structures in the Planck model exhibits a much more complicated behavior than the model with a constant gas opacity. The main difference lies again in the occurrence of an additional force due to radiation pressure on molecules in the Planck model. In the model with a constant gas opacity, radiation pressure on molecules is negligible and, therefore, the inner regions are controlled by the interior pulsation and the pressure gradient. Such models exhibit clearly a shock structures and a step-like density structure (e.g. $R = 1.4\,R_0$ in the 3$^{\text{rd}}$ column, $R = 2\,R_0$ in the 4$^{\text{th}}$ column).

The comparative studies of the Planck models with the Rosseland and the constant opacity models shown in this section has illustrated, that the hydrodynamic structures of the models becomes more complex in the inner radial regions as the gas opacity increases. Consequences for the dust formation and observational quantities like mass loss, dust-to-gas ratio, and outflow velocity will be outlined in the next sections.

4.3.3 Gas opacities influencing dust formation

The time-dependent treatment of the dust formation process allows for a consistent calculation of the dust properties and the grain size distribution function of the emerging dust component (cf. Dominik et al. 1989, Gauger et al. 1990). Since each fluid element moving through the circumstellar shell has its own history, different dust properties will characterize different fluid elements.

Figure 4.13 depicts mean dust properties as function of the radial distance in a Planck and in a Rosseland model at the same instant of time. Figure 4.14 is similar to Fig. 4.13, but compares mean dust properties in a Planck model and a model with constant gas opacity for different stellar parameters than in Fig. 4.13.

Nucleation (solid lines, upper panels, Figs. 4.13, 4.14), which is the pre-condition for dust formation, is slightly less effective in models computed with Planck mean gas opacities than in models with a smaller gas opacity as can be concluded from the larger nucleation rate in the Planck models, which is a permanent feature of these models. If effective dust formation would take place, the nucleation rate could not reach its maximum since considerable amounts of the dust forming material would be consumed during the growth process. The radial zone where nucleation takes place is slightly more extended in the Planck mean models and nucleation sets in at smaller radii than in models with a smaller gas opacity.

Independent of the stellar temperature, the models computed with Planck mean gas opacities have a lower degree of condensation than models with a weaker gas opacity and otherwise equal stellar parameters (compare dashed lines, upper panels). In Planck models, effective dust growth is suppressed due to smaller densities, and consequently, more particles of small sizes are formed in the Planck models (compare dashed and solid line, lower panels). The characteristic shell structure of the circumstellar envelope occurs for all the gas opacities studied.

The mean grain radius $\langle r \rangle$ has several maxima and a very pronounced one at small radii in all the models. Its occurrence at radii smaller than where nucleation sets in indicates that some of the grains remain in these dense regions of the atmosphere and, therefore, continue to grow. This especially occurs in Planck models since no strong shocks have developed at such small radial distances.

The mean grain radius reaches values of $\approx 0.3\mu$m in the Planck model shown in Fig. 4.13 and $\approx 0.24\mu$m in the model in Fig. 4.14. In contrast, both models with smaller gas opacities (right column) show smaller mean grain radii in these inner regions. The opposite occurs at large radial distances. The comparison of the Planck models to the models with smaller gas opacities shows that the mean grain size is smaller in the Planck case at $R > 3\,R_0$ due to the smaller overall density in the shell (see also Fig. 4.15).

All models have in common that the shells contain dust grains of different sizes at different sites in the shell. The mean particle radius is smallest at the outer (steep) edge of the shells (compare the minima of $\langle r \rangle$ with f_c) and reaches its maximum at somewhat smaller radial distances somewhat off the maximum degree of condensation as result of the increased gas density in the post-shock region. The grains do not

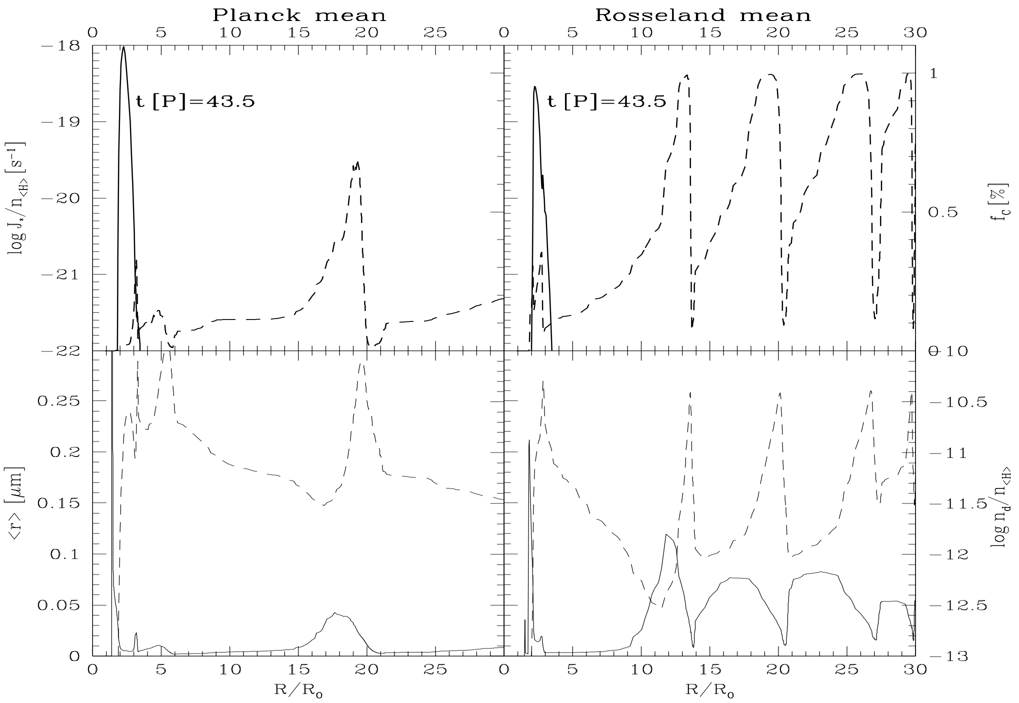

Figure 4.13: Dust properties for carbon-rich models computed with Planck (left column) and with Rosseland mean (right column) gas opacities at one instant of time. The **model parameters** are: $T_\star = 2600$K, $M_\star = 1M_\odot$, $L_\star = 10^4 L_\odot$, C/O = 1.8, $R_{\rm inner} = 0.91\,R_0$, $\Delta u = 2$km/s, $P = 650$d

have enough time to grow effectively at the edge of the dust shell, therefore, many small particles are formed there (compare minimum of $n_{\rm d}/n_{\rm <H>}$ and f_c). In contrast, the material in the wake of the shock moves less fast and remains longer in the compression region and, therefore, can grow to larger grain size. If the density drops, the mean particle radius decreases at comparable radial positions. This can be seen by comparing e.g. the maximum grain size radius at $R \approx 17\,R_0$ in Fig. 4.14 (solid line, left column, 2$^{\rm nd}$ panel) and the decreasing density enhancement in Fig. 4.11 at $R \approx 17\,R_0$ (solid line, left column, 2$^{\rm nd}$ panel).

Fig. 4.15 shows time averaged grain size distribution functions of a model computed with Planck mean gas opacities (left panel) and a model computed with a constant gas opacity (right panel). The average was taken over 10 periods in time steps of 0.01 periods at $R \approx 40\,R_0$ (compare Sects. 4.3.1, 4.3.2.2).

The grain size distributions indicate that the maximum particle size is smaller in the Planck model ($a_{\rm max} \approx 0.4\,\mu$m) than in the model with a smaller gas opacity component ($a_{\rm max} \approx 0.1\,\mu$m $\ldots 7\,\mu$m), the reason being again the smaller density in the Planck model. In addition, more small particles with $a \leq 0.01\,\mu$m are formed in the Planck model. The bulge of the particles in the model with a small gas opacity has radii $a \leq 0.07\,\mu$m (right panel, Fig. 4.15) and grains with $a \geq 0.3\,\mu$m are less abundant in these models (up to 6 orders of magnitude).

Since the the conditions for dust growth have been favorable less often in the Planck models than in the models with smaller gas opacities, the grain size distribution of the Planck models is less uniform than in the model with the smaller gas opacity. Therefore, the Planck grain size distribution exhibits therefore the charac-

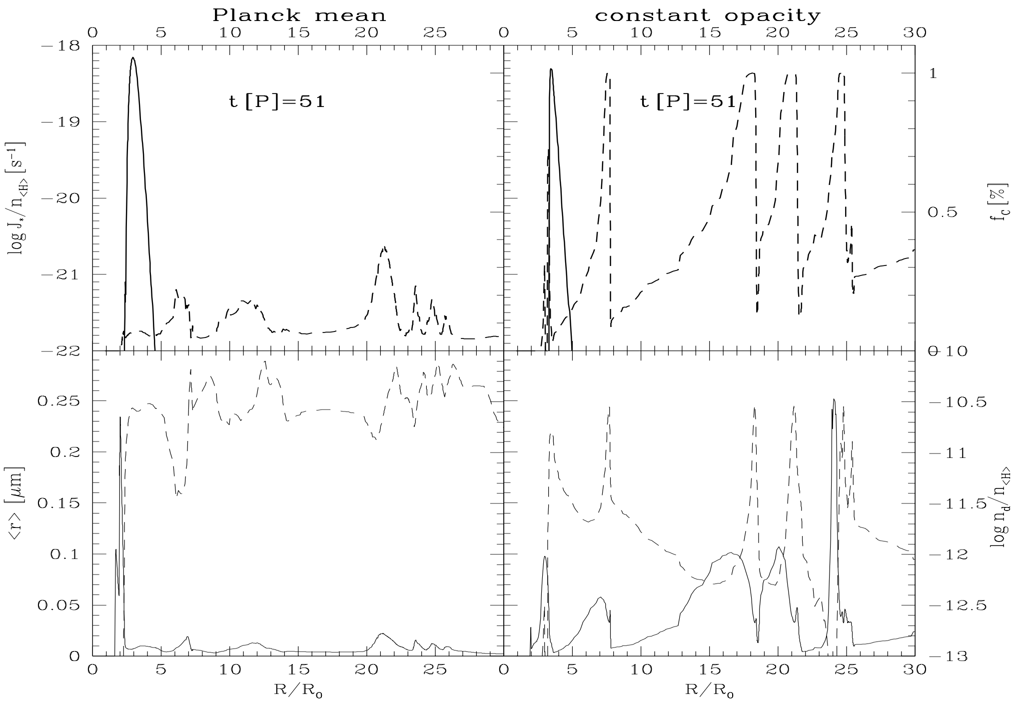

Figure 4.14: Dust properties for carbon-rich models computed with Planck mean (left column) and with a constant (right column) gas opacity. The **model parameters** are: $T_\star = 3000$K, $M_\star = 1M_\odot$, $L_\star = 10^4 L_\odot$, C/O = 1.8, $R_{\rm inner} = 0.91\,R_0$, $\Delta u = 2$km/s, $P = 650$d

teristic dust formation events during the a mass element's time evolution. The mean grain size distribution of different fluid elements can be very different and exhibit, for example, a multiple-peaked shape since one fluid element can meet favorable nucleation and growth conditions several times during its evolution (cf. Winters et al. 1999).

The fluid elements contain information about their history since dust, once formed, is very resistant against evaporation. Only a temperature increase of about 500 K with respect to the dust formation temperature would lead to dust evaporation (Winters 1997). A possible increase of the temperature behind the shocks due to backwarming will in the first place affect the gas temperature but not the dust temperature.

The averaged size distribution functions shown in Fig. 4.15 provide information about the size distribution of dust particles expelled into the ISM by the star, and it can be concluded that, beside a large amount of small particles, also a small amount of large particles will be injected into the ISM. The size of the particles depends therefore indirectly on the opacity of the gas.

4.3.4 Gas opacities influencing the wind properties

In view of the previous considerations, results and discussions, it is not surprising that wind properties like the mass loss rate $\langle \dot{M} \rangle$, the outflow velocity $\langle v_\infty \rangle$, and the dust-to-gas ratio $\langle \rho_{\rm dust}/\rho_{\rm gas} \rangle$ are quite sensitive to the gas opacity treatment. This sensitivity is much larger regarding the gas opacities than regarding the dust opacities as the differences between the mean gas opacities are much larger than between the

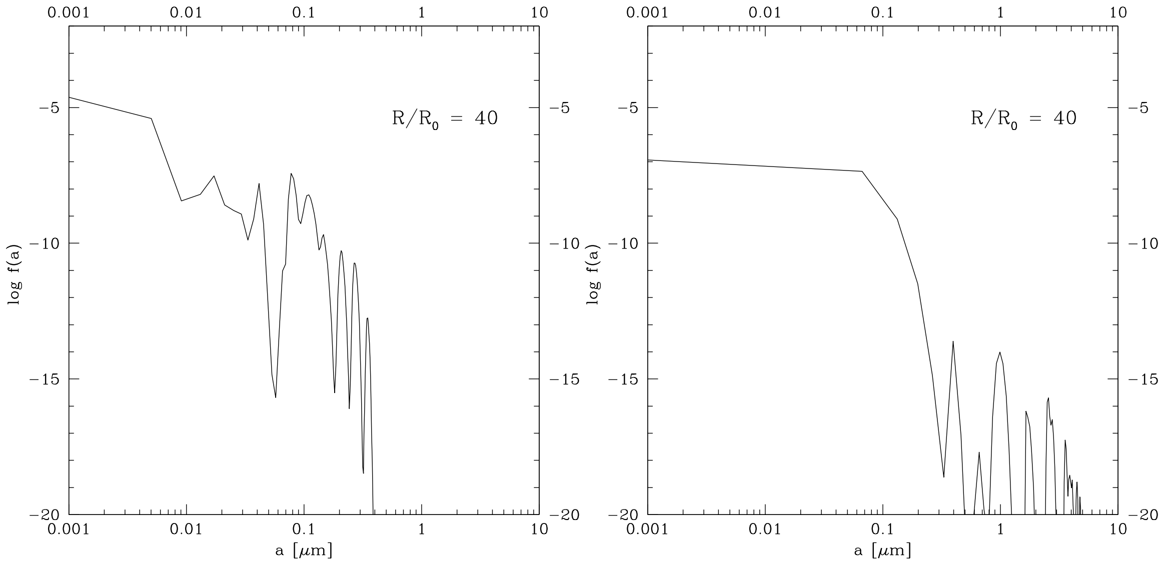

Figure 4.15: Time averaged grain size distribution functions in units of a_0 (hypothetical grain radius) at $R \approx 40\,R_0$ for a Planck model (left) and a model with constant gas opacity (right). The **model parameters** are: $T_\star$ = 3000K, $M_\star$ = 1$M_\odot$, $L_\star$ = $10^4 L_\odot$, C/O = 1.8, $R_{\rm inner} = 0.91\,R_0$, Δu = 2km/s, P = 650d.

dust opacities (see Figs. 3.7, 3.8).

Models computed with Planck mean gas opacities show a larger density scale hight than comparable models computed with Rosseland mean opacities (or constant opacity). The lower density (at similar optical depth) is a consequence of the higher opacity in the Planck model. The lower gas density has a direct impact on the dust growth processes whereas the temperature controls the rate of seed nucleation. Consequently, smaller dust particles are expected to be observable in this case.

Since the dust growth is less efficient in the Planck models, the average dust-to-gas ratios $\langle \rho_{\rm dust}/\rho_{\rm gas}\rangle$ are consequently smaller compared to models with Rosseland means or constant opacities (Table 4.4). Also, the average outflow velocity $\langle v_\infty \rangle$ is smallest in the Planck models since less dust is present and acceleration by radiation pressure is less efficient. The lower gas density is responsible for the small mass loss rates $\langle \dot{M} \rangle$ in the Planck models.

4.3.5 Molecular layers in time-dependent models

Molecules are present in the gas phase if the temperature is not too high ($\lesssim$ 3000 K) and if they are not consumed into solids at low temperatures ($\lesssim$ 1000 K). Furthermore, the amount of molecules present also depends on the density of the gas which is influenced by pulsation leading to subsequent shocks which compress and levitate the gas.

An analysis of the gas is performed by re-computing the chemical composition of the gas (see Chap. 1) on top of the time-dependent model output taking into account the depletion of the gas phase due to dust formation (Figs. 4.16, 4.17).

a) carbon-rich composition

Molecules appear to be present in distinct layers as it can be seen from Fig. 4.16

Stellar Parameter						Pulsation Parameter		Results				
χ^{g} [cm^2/g]	$T_\star$ [K]	$L_\star$ [$L_\odot$]	$M_\star$ [$M_\odot$]	C/O	ϵ_{el}	P [d]	Δu [km/s]	g [cm/s^2]	R_0 [$R_\odot$]	$\langle \dot{M} \rangle$ [$M_\odot$/yr]	$\langle v_\infty \rangle$ [km/s]	$\langle \rho_{\mathrm{dust}}/\rho_{\mathrm{gas}} \rangle$
$\chi^{\mathrm{g}}_{\mathrm{const}} = 2 \times 10^{-4}$	2600	10^4	1	1.8	solar	650	2	0.113	492	$9.4\,10^{-6}$	31.9	$4.1\,10^{-3}$
$\chi^{\mathrm{g}}_{\mathrm{Ross}}$	2600	10^4	1	1.8	solar	650	2	0.113	492	$2.5\,10^{-6}$	21.4	$2.1\,10^{-3}$
$\chi^{\mathrm{g}}_{\mathrm{Planck}}$	2600	10^4	1	1.8	solar	650	2	0.113	492	$3.8\,10^{-7}$	18.0	$1.2\,10^{-3}$
$\chi^{\mathrm{g}}_{\mathrm{Ross}}$	2600	$6\,10^3$	1	1.8	solar	650	2	0.188	381	$6.5\,10^{-7}$	22.0	$2.5\,10^{-3}$
$\chi^{\mathrm{g}}_{\mathrm{const}} = 2 \times 10^{-4}$	2800	10^4	1	1.8	solar	650	2	0.152	424	$7.4\,10^{-6}$	31.9	$2.8\,10^{-3}$
$\chi^{\mathrm{g}}_{\mathrm{Ross}}$	2800	10^4	1	1.8	solar	650	2	0.152	424	$1.9\,10^{-6}$	23.3	$2.6\,10^{-3}$
$\chi^{\mathrm{g}}_{\mathrm{Planck}}$	2800	10^4	1	1.8	solar	650	2	0.152	424	[a]	[a]	[a]
$\chi^{\mathrm{g}}_{\mathrm{const}} = 2 \times 10^{-4}$	3000	10^4	1	1.8	solar	650	2	0.200	369	$4.1\,10^{-6}$	25.3	$2.3\,10^{-3}$
$\chi^{\mathrm{g}}_{\mathrm{Ross}}$	3000	10^4	1	1.8	solar	650	2	0.200	369	[a]	[a]	[a]
$\chi^{\mathrm{g}}_{\mathrm{Planck}}$	3000	10^4	1	1.8	solar	650	2	0.200	369	$4.6\,10^{-8}$	10.2	$4.9\,10^{-4}$
$\chi^{\mathrm{g}}_{\mathrm{const}} = 2 \times 10^{-4}$	3200	10^4	1	1.8	solar	650	2	0.259	314	$8.2\,10^{-7}$	27.7	$2.4\,10^{-3}$
$\chi^{\mathrm{g}}_{\mathrm{Ross}}$	3200	10^4	1	1.8	solar	650	2	0.259	314	[a]	[a]	[a]
$\chi^{\mathrm{g}}_{\mathrm{Planck}}$	3200	10^4	1	1.8	solar	650	2	0.259	314	$8.3\,10^{-8}$	12.6	$6.5\,10^{-4}$
$\chi^{\mathrm{g}}_{\mathrm{Planck}}$	3000	10^4	1	0.43	solar	650	2	0.152	424	[n]	[n]	0

Table 4.4: Hydrodynamic model sequences computed with various mean gas opacities. Results for $\dot{M}$, v_∞, and $\rho_{\mathrm{dust}}/\rho_{\mathrm{gas}}$ are mean values of time means at several radial distances.

[a] For this stellar parameters, the model could not be calculated for numerical reasons.

[n] negligible

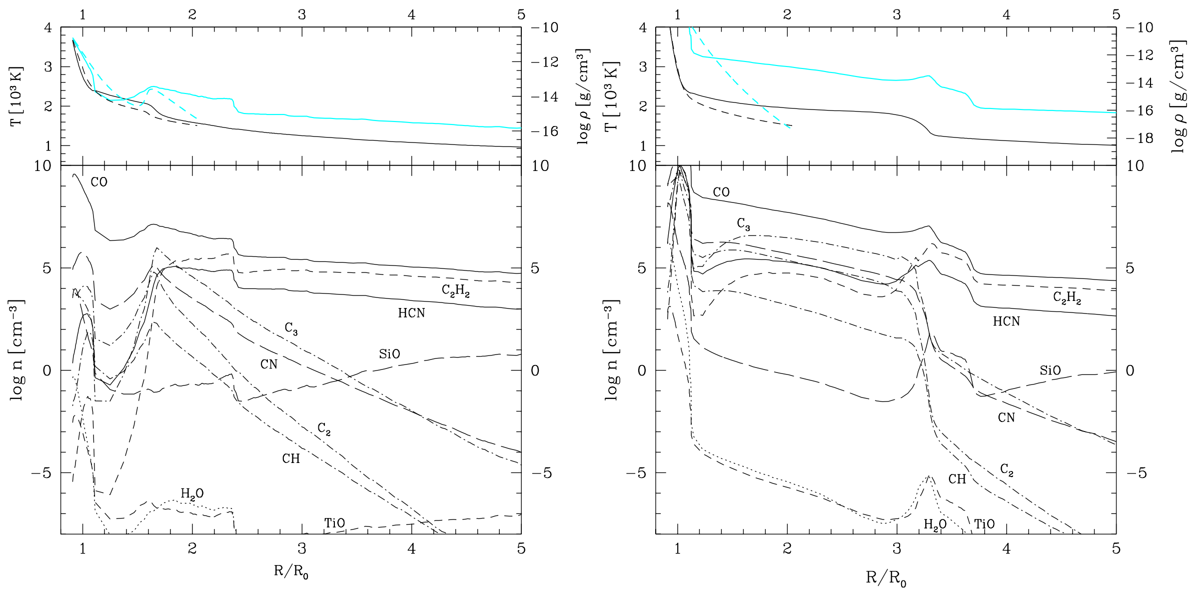

Figure 4.16: Number densities of the molecules included as line opacity species in time-dependent models with a strong molecular opacity component ($\chi^{\rm g} = \chi^{\rm g}_{\rm Planck}$, left) and in a model with a negligible molecular opacity ($\chi^{\rm g}/\rho = 2 \times 10^{-4}{\rm cm}^2/{\rm g}$, right). The top panels show the temperatures (full black) and the density structures (full grey) of the time-dependent models. In addition, the density structure of the static model (dashed grey) is depicted for comparison. The **model parameters** are: $T_\star = 3000$K, $M_\star = 1M_\odot$, $L_\star = 10^4 L_\odot$, C/O = 1.8, $R_{\rm inner} = 0.91\,R_0$, $\Delta u = 2$km/s, $P = 650$d.

which depicts the results for two carbon-rich time-dependent models computed with different gas opacities and similar stellar parameters (see Sect. 4.3.2.2). The innermost molecular layer (region of enhanced molecular particle density $n_{\rm y}$) at about $1 \ldots 1.2\,R_0$ in both models is a result of the outwards decreasing temperature and density and occurs already in the static models. In contrast to the static case, there exists a second molecular layer at $1.5 \ldots 3\,R_0$ in the time-dependent models caused by the outwards slowly decreasing or even re-increasing density in combination with decreasing temperature. The course of the density is a result of the levitation caused by the subsequent shock waves due to the pulsation of the star. In addition, the occurrence of a pressure inversion in the Planck model causes locally increasing molecular densities in the time-dependent model AND in the static model. The local density enhancement due to the pressure inversion leads to an increased optical depth which causes a backwarming of those layers closer to the star (Eq. 4.17) of about ≈ 200 K in the Planck model (left column, Fig. 4.16). In the constant opacity model, the dust opacity is responsible for another backwarming of ≈ 400 K (right column, Fig. 4.16) and leads to a warming of the molecular layer between $R \approx 3.3 \ldots 3.6\,R_0$, in contrast to the Planck model.

Since the shocks are damped in the Planck models due to the pressure inversion (left column, Fig. 4.16), the atmosphere is less levitated and the density is already so small that the number densities of the di-atomic opacity sources and C_3 decrease faster than in the model with the constant gas opacity (right column, Fig. 4.16). The number densities of CH, CN, C_2, and C_3 (also TiO, H_2O) reach a second maximum in the pressure inverted region ($R \approx 1.9\,R_0$). A similar behavior can be observed for

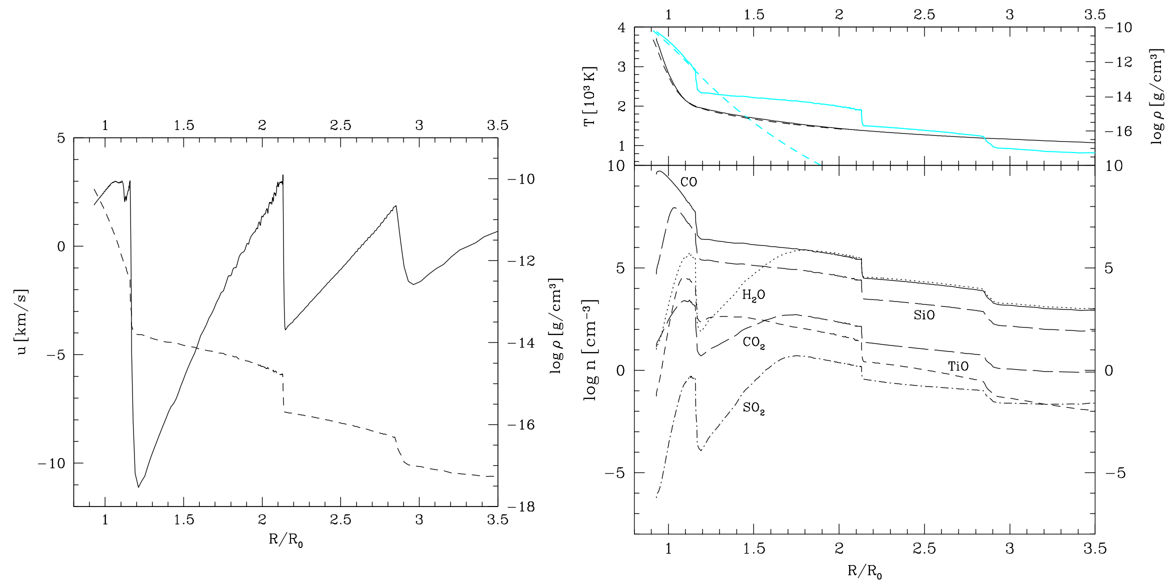

Figure 4.17: Dense molecular layers in a time-dependent oxygen-rich model. The left figure depicts an oxygen-rich hydrodynamic model structure, whereas in the right figure the density and temperature structures (top panel) are shown for comparison together with the molecular number densities $n_{\rm y}$. The **model parameters** are: $T_\star$ = 2800K, $M_\star = 1M_\odot$, $L_\star = 10^4 L_\odot$, C/O = 0.43, $R_{\rm inner} = 0.91\,R_0$, Δu = 2km/s, P = 650d, $\chi^{\rm g} = \chi^{\rm g}_{\rm Planck}$.

C_2H_2 and HCN (also SiO), and in addition, these molecules remain quit abundant at large radial distances but finally decrease at $R \approx 20\,R_0$, almost independent of the gas opacity (not depicted in Fig. 4.16).

The levitation of the gas by shock waves, which compress the material and cause a subsequent effective dust growth at $\approx 3\,R_0$, is more effective in the model with a constant gas opacity and leads to the second maximum of the number densities of CH, C_3, C_2H_2, and HCN in such models (right column, Fig. 4.16). While CH and C_3 (also CN, C_2) decrease at about $3.2\,R_0$, C_2H_2 and HCN undergo a third additional increase of their number densities which can also be observed for SiO, TiO, and H_2O. Since this peak coincides with a dust formation region, the dust further compresses the gas in the wake of the shock due to momentum absorption from the radiation field and momentum transfer to the gas by frictional coupling.

The oxygen bearing molecules gain importance at low temperatures and densities in a carbon-rich situation. Therefore, such molecules cannot be neglected as opacity sources. SiO and TiO are the most abundant opacity sources if dust formation is effective ($> 15\,R_0$, not depicted in Fig. 4.16).

As previously has been pointed out, the density of a Planck model is smaller than in a model calculated with a constant gas opacity at comparable optical depth. Consequently, the column densities of the gas and the total particle numbers are smaller in the Planck model (compare Table 4.5).

b) oxygen-rich composition

The study of a dust-free oxygen-rich model computed with Planck mean gas opacity tables for C/O=0.43 exhibits a more transparent picture of the distribution of molecules in such an atmosphere. Dust formation, growth and evaporation is treated

	Column density [cm^{-2}]				**Total particle number**				
	C/O =1.8 [a]		C/O = 0.43 [b]		C/O =1.8 [a]		C/O = 0.43 [b]		
	$\chi^{g}_{\rm Planck}$	$\chi^{g}_{\rm const}$	$\chi^{g}_{\rm Planck}$		$\chi^{g}_{\rm Planck}$	$\chi^{g}_{\rm const}$	$\chi^{g}_{\rm Planck}$		
molecule	dynamic model	dynamic model	initial model	dynamic model	dynamic model	dynamic model	initial model	dynamic model	molecule
CO	$6.3\,10^{21}$	$8.4\,10^{24}$	$1.2\,10^{22}$	$1.2\,10^{22}$	$5.3\,10^{49}$	$6.4\,10^{52}$	$1.3\,10^{50}$	$1.3\,10^{50}$	CO
TiO	$5.1\,10^{12}$	$1.6\,10^{15}$	$6.7\,10^{16}$	$8.7\,10^{16}$	$1.7\,10^{43}$	$1.2\,10^{43}$	$9.2\,10^{44}$	$1.2\,10^{45}$	TiO
SiO	$2.0\,10^{16}$	$1.2\,10^{20}$	$1.6\,10^{20}$	$2.0\,10^{20}$	$1.2\,10^{46}$	$8.9\,10^{47}$	$1.9\,10^{48}$	$2.5\,10^{48}$	SiO
H_2O	$3.9\,10^{11}$	$1.5\,10^{18}$	$5.3\,10^{17}$	$1.1\,10^{19}$	$2.8\,10^{39}$	$1.0\,10^{46}$	$7.4\,10^{45}$	$3.8\,10^{47}$	H_2O
CH	$1.4\,10^{16}$	$5.7\,10^{21}$	–	–	$1.2\,10^{44}$	$4.6\,10^{49}$	–	–	CH
CN	$2.0\,10^{18}$	$3.4\,10^{22}$	–	–	$2.4\,10^{46}$	$2.8\,10^{50}$	–	–	CN
C_2	$1.9\,10^{17}$	$9.4\,10^{21}$	–	–	$3.7\,10^{45}$	$8.0\,10^{49}$	–	–	C_2
C_3	$3.0\,10^{18}$	$6.9\,10^{21}$	–	–	$7.7\,10^{46}$	$6.4\,10^{49}$	–	–	C_3
HCN	$1.9\,10^{18}$	$1.7\,10^{22}$	–	–	$9.3\,10^{49}$	$1.5\,10^{50}$	–	–	HCN
C_2H_2	$9.2\,10^{18}$	$1.2\,10^{22}$	–	–	$1.0\,10^{48}$	$1.1\,10^{50}$	–	–	C_2H_2
CO_2	–	–	$5.7\,10^{15}$	$1.5\,10^{16}$	–	–	$7.7\,10^{43}$	$3.5\,10^{44}$	CO_2
SO_2	–	–	$5.7\,10^{11}$	$6.1\,10^{13}$	–	–	$8.4\,10^{39}$	$2.4\,10^{42}$	SO_2

Table 4.5: Column densities ($\rho^{\rm col}_{\rm y} = \int_{r_1}^{r_2} n_{\rm y}\, dr$) and total particle numbers ($N_{\rm y} = 4\pi \int_{r_1}^{r_2} r^2 n_{\rm y}\, dr$) for two carbon-rich models[a] with different molecular opacities and one oxygen-rich model. The radial range considered is $R/R_0 = 0.93 \ldots 4.2$ for the oxygen-rich models[b] and $R/R_0 = 0.91 \ldots 21.35$ in the carbon-rich models. – = negligible

Model parameters:

[a] $T_\star = 3000$K, $M_\star = 1M_\odot$, $L_\star = 10^4 L_\odot$, C/O = 1.8, $R_{\rm inner} = 0.91\,R_0$, $\Delta u = 2$km/s, $P = 650$d

[b] $T_\star = 2800$K, $M_\star = 1M_\odot$, $L_\star = 10^4 L_\odot$, C/O = 0.43, $R_{\rm inner} = 0.91\,R_0$, $\Delta u = 2$km/s, $P = 650$d

by means of the moment method developed by Gail & Sedlmayr (1988) and Gauger et al. (1990), which here is applied to homogeneous formation of SiO-dust.

The oxygen-rich model shown in Fig. 4.17 does not provide suitable conditions for dust formation since the (grey) gas temperature is too high for SiO nucleation to take place (Jeong et al. 1999). In Fig. 4.17 (left column) the velocity and the density structures are depicted showing that the atmosphere is not very extended. In other words, the mass loss is very low ($< 10^{-11} M_\odot$/yr). Since radiation pressure on molecules also fails to accelerate the gas substantially (the radiative acceleration by molecules is less than 0.3 times the gravitational deceleration everywhere in this model), no further disturbances are introduced into the velocity field and the model exhibits a rather simple saw-tooth-like velocity structure and a step-wise decreasing density profile. Due to the propagating shocks caused by the pulsation, a considerable time-dependent levitation of the atmosphere is achieved, i.e. the density is much larger than in the initial hydrostatic model (see top panel, right column, Fig. 4.17).

Similar to the carbon-rich models, different layers of high molecular number densities occur. A first maximum is situated at about $1 \ldots 1.2\,R_0$ which is typical for static models (compare dashed grey line and solid grey line in the top right panel). The outwards traveling shocks levitate the atmosphere and provide a density enhancement, causing a second maximum of molecular densities, compared to the static model atmospheres. The increasing number density of polyatomic molecules (e.g. H_2O, CO_2, SO_2) in layers above the photosphere is a (natural) result of time-dependent models. Again, the occurrence of such molecular layers at radial distances of $1.6 \ldots 2.1\,R_0$ is caused by the sensitivity of those molecules against changes of the gas density.

The column densities and the total numbers of molecules included as line opacity sources and for CO_2 and SO_2 for the carbon-rich and an oxygen-rich models are listed in Table 4.5. In the oxygen-rich case, the column densities and total particle numbers are also listed for the initial hydrostatic model. Both values are different compared to those obtained from the time-dependent model for the poly-atomic molecules (H_2O, CO_2, SO_2) in contrast to the di-atomic molecules (CO, TiO, SiO) which reveal only a single maxima or a monotonically decreasing number density with increasing radius. Therefore, the deviation of the column densities and the total particle numbers are relatively small, namely, $\approx 24\%$ for SiO and TiO, and negligible for CO. In contrast, the total numbers of CO_2, H_2O, and SO_2 have increased in comparison to the static model by a factor of ≈ 4.5, ≈ 51, and ≈ 290, respectively.

Since the gas density is higher in models with small gas opacities, the total particle numbers and the column densities of the molecules are larger than in models with large gas opacities as can be observed from Table 4.5 or from the carbon-rich models shown before.

4.3.6 Discussion

The influence of the gas opacity on time-dependent models for the outer atmospheres of AGB stars has been studied in the framework of upper and lower limit considerations. Models computed with Planck mean gas opacities illustrate the maximum effect whereas models with Rosseland mean or constant gas opacities illustrate the minimum effect that the gas opacity can have on the structure and the dynamics of a circumstellar shell and therefore on the dust formation. The study of both limit cases has confirmed the basic picture of pulsation induced, dust driven winds where the gas close to the star is levitated by shock waves which facilitates dust formation at larger distances. The forming dust is accelerated by radiation pressure due to its large opacity, transfers momentum to the gas by friction and introduces perturbations into the velocity field (exterior κ-mechanism, Fleischer et al. 1995) driving a massive stellar wind. The models computed with new Rosseland mean gas opacities (Chap. 2) lead to similar results as obtained by Fleischer et al. (1992). Fleischer et al. (1995) already pointed out that no qualitative differences in the hydrodynamic behavior should be expected between models computed with a constant gas opacity and Rosseland mean gas opacities. The work presented here shows, however, that substantial deviations from these earlier works occur if a larger gas opacity (Planck mean) is considered.

Planck mean gas opacity models: Planck mean gas opacities are larger than Rosseland mean gas opacities by up to 3 orders of magnitude. Consequently, the densities in the models calculated with large gas opacities (Planck mean) are much smaller at the same optical depth τ. Loidl et al. (1999) discussed synthetic spectra of the near IR which have been calculated on top of different time-dependent models using different gas opacities (Höfner et al. 1998). The spectrum calculated on the bases of a model with a smaller gas opacity (i.e. models with Rosseland mean or constant gas opacity) exhibits molecular features which are unrealistically saturated throughout the near IR wavelength region due to the large density. Only Planck models lead to synthetic spectra which are qualitatively comparable with the observations. A similar tendency has been noticed in this work by comparing the molecular column densities with the values derived from recent ISO observations regarding the discussion of the existence of "warm molecular layers".

Pressure inversions: The models with Planck mean gas opacities exhibit pressure inverted regions due to $\alpha^{\rm tot} > 1$ as a consequence of locally large gas opacities at small radii where dust is not yet present. The formation of pressure inversions has already been discussed for the initial hydrostatic case (Sect. 4.2) where the coinciding increase of the C_3 concentration was pointed out. The importance of C_3 arises from its sensitive dependence on the gas density as indicated by its narrow peaked number density (Chap. 1, see also Loidl et al. 1999). The occurrence of pressure inversions in the time-dependent models at $R \lesssim 2\,R_0$ proves that the positive pressure gradient in the initial models is not an artifact of the demand of the hydrostatic equilibrium, but is rather a consequence of the physical situation encountered in the system. Pressure inversions can also occur in layers where dust is formed independent of the gas opacity (consult the models in Fleischer et al. 1992, 1993, 1994, Winters et al. 1997, Höfner et al. 1997). In such models, the local increase of the density with increasing distance from the star is a result of the strong dust opacity, which causes a compression of the material just behind the shock front.
The pressure inversions caused by large gas opacities damp the propagating shocks if their amplitudes are sufficiently small. Traveling waves are partly reflected and partly transmitted, i.e. they tunnel (see Mihalas & Mihalas 1984) through the dense layer and continue to propagate outwards with a reduced amplitude after the pressure inverted region. Shocks may also divide into two waves of almost similar strength: one continues to travel outwards, one travels backwards which will merge with the subsequent shock (see Fig. 4.6, periods 35, 37). Partial wave reflection can also be observed from the model series described in Fleischer et al. (1992), Winters et al. (1994), and Fleischer et al. (1995).
Fleischer (1994) investigated the (cut-off) frequency which a wave must exceed in order to propagate freely through the atmosphere, and he pointed out, that the time scale imposed on the medium by the propagating wave has to be smaller than the time scale on which the properties of the medium (e.g. density) change. Furthermore, Mihalas & Mihalas (1984) discuss that if waves encounter a semi-infinite region in a non-isothermal atmosphere in which they are evanenced, they can be totally reflected with no transmission of energy beyond the point of reflection. If the evanenced layer is finite, some fraction of the incident wave energy may leak through the region by tunneling, and the wave continues to propagate with reduced amplitude on the other side of the barrier.

Observational quantities & wind properties: The molecular opacities have a considerable influence on the dust complex, resulting in smaller mass loss rates, smaller outflow velocities, and smaller dust-to-gas-ratios in Planck models. Similar results for these wind properties have been obtained by Höfner et al. (1998). In addition, since dust growth is less effective if the density is smaller, more smaller dust particles are formed. Consequently, the particles injected into the ISM would be larger if the gas opacity is small. However, the size of the particles is not unique, but multiple-peaked size distributions can occur, as discussed by Winters et al. (1999). These peaks result from different dust formation events during the history of the different gas parcels moving though the circumstellar shell. Small amounts of large particles can be injected into the ISM, too.

Chemical dust blocking: In turn, dust formation may change the gas opacity since the molecules which are consumed by dust formation can be depleted. If, for instance, all carbon is consumed by dust formation, no molecules containing carbon can be present in the gas phase (except CO). A *chemical dust blocking* takes places, similar to the *chemical CO blocking* which consumes all oxygen in a carbon-rich gas in CO and all carbon in an oxygen-rich gas. This effect has not be taken into account during the pre-computation of the mean opacity tables in this work, since the degree of condensation, and thereby the depletion of the gas phase, are a result of the time-dependent models but the tables are used as input data. However, the molecular opacities are mainly important in the inner dust-free region and here, and in all places where the dust growth is not efficient, the opacity tables are correct.

C/O ratio: Considering an increased C/O ratio, the gas opacity would increase in a carbon-rich gas and the overall gas density would decrease in the model (cf. Höfner et al. 1998). But since, at the same time, the number densities of the carbon-bearing molecules would increase relative to the other molecules with increasing CO ratio, the dust growth should be supported (cf. Fleischer 1994). An increase of the C/O ratio, according to the classical models of circumstellar envelopes (Fleischer et al. 1992, Höfner et al. 1997), causes an increase of the degree of condensation, and an increase of the outflow velocity but also a decrease of the mass loss rate. Fleischer (1994) pointed out that this correlation is not obvious and has to be taken with care. Höfner et al. (1998) reject such a correlation and conclude from the lower gas density in their initial hydrostatic models that a higher C/O ratio causes a smaller gas density and thereby a smaller degree of condensation. A closer inspection of their Table 1[17] indicates, however, that a pure increase of the C/O ratio by otherwise constant model parameters leads to an increase of the mass loss rate. It seems possible to conclude that the increased degree of condensation due to the increased carbon abundance is responsible for the changing properties of these models.
Therefore, a sensitive balance exists between i) the increasing particle densities of the molecular opacity species by an increasing carbon abundance and the consequently decreasing gas density due to the increased molecular opacity, and on the other side, ii) the better conditions for dust formation by the increasing particle density of the condensation species with increasing C/O ratio. It seems not plausible that point i) dominate the hydrodynamic situation in the time-dependent models as suggested by Höfner et al. (1998).

Multiperiodicity: The phenomenon of multiperiodicity occurs if the piston period divided by the eigenperiod of the system, which is a characteristic period of the system induced by the dust, yields an integer value (cf. Fleischer et al. 1995). Winters et al. (1993a) has demonstrated that multiperiodicity is also reflected in the light curves of the models. Since the gas opacity has an indirect but nevertheless important influence on the dust complex, it influences the multiperiodic behavior of the dust shell. For instance, if less dust is formed in models with large gas opacities, such models tend to be rather semiregular or even chaotic.

[17]Compare model P10C14U4 with model P10C18U4, and model P13C12U4 with model P13C14U4 in Table 1 in Höfner et al. (1998).

Numerics: It is interesting to notice that for some combination of stellar parameters and treatments of gas opacity no solution of the considered equations could be obtained while the corresponding model with a constant gas opacity seem to exist always (Table 4.4). Also the initial static model exists for any of the opacity approximations. For some physical reasons, models with Rosseland mean opacities provide numerical problems for large stellar temperature probably because of the less efficient dust formation and the diminishing gas opacity at low temperatures. In contrast, the Planck models provide a physical solution at such higher stellar temperatures (e.g. $T_\star = 3200\,\mathrm{K}$, see Table 4.4). Hence, the gas opacity does not only influence the hydrodynamical structure of the model, and thereby the dust complex, but also the applicability of the models.

Warm & dense molecular layers: CO_2 and SO_2, in addition to H_2O, are discussed in the literature (e.g. Tsuji et al. 1997, Justtanont et al. 1996, Ryde et al. 1999, Yamamura et al. 1998) to form "warm molecular layers". The introduction of such artificial, quasi-static layers on top of the photosphere was considered as necessary to explain the observed spectra. Similar problems have been recognized for carbon-stars by Yamamura et al. (1998) for C_2H_2 and HCN. Here, the identification of molecular hotbands has been proposed in order to overcome the discrepancies between hydrostatic models and observations.

Table 4.6 lists several physical and chemical quantities, which have been deduced from recent ISO SWS observations by different workers. These observations led several authors to the conclusion that additional warm and dense gas layers must exist in the outer atmospheres of AGB stars. Beside the column densities and the total particle numbers, also the excitation temperatures of the molecules are listed. In the case of absorption features, this excitation temperature $T_{\rm exc}$ reflects the rotational temperature of the lower vibrational state, and of the upper vibrational state in case of an emission feature. These excitation temperatures are not alway equal to the gas kinetic temperature since non-LTE calculations show that depending on the gas density, the level populations may substantially differ from LTE (Woitke et al. 1996). However, is it beyond the scope of this work to discuss this point in more detail.

A cautious comparison of the magnitudes of the column densities and total particle numbers might serve as a first guide to see whether levitation by shock waves may explain the nature of the "warm molecular layers". The best agreement with the observations is achieved for the column densities of H_2O, $N_{\rm obs} \approx 0.6 \ldots 2.7\,N_{\rm calc}$, in the oxygen-rich case ($N_{\rm calc}$ calculated column density (Table 4.5), $N_{\rm obs}$ observed column density (Table 4.6)) and for C_2H_2, $N_{\rm obs} \approx 0.11\,N_{\rm calc}$, in the carbon-rich case, both from the models computed with Planck mean gas opacities. The deviations become larger for CO_2, CO, and SO_2, respectively, although tendencial agreement may also be recognized for these molecules. Effects of non-equilibrium chemistry are expected for SO_2 and CO_2 (e.g. Ryde et al. 1999, Yamamura et al. 1998). Authors like Yamamura et al. (1998) and Justtanont et al. (1996) estimate an error of a factor of two for the total number and column densities deduced from the observations, but still, this is not enough to bring the theoretical results in a better agreement with the observational derived quantities. This might not be surprising since the models discussed here have not been designed to fit any of the observations but rather to study the physical effects possibly responsible for the occurrence of molecular layers. However, the location of the second, non-photospheric molecular layer at $\approx 2\,R_0$

molecule	band [μm]	object	$T_{\rm exc}$ [K]	**Column density** [cm^{-2}]	**Total particle number**	R [R_*]	references	molecule
CO	4.6 [e]	SW Vir	2160	$1.0\,10^{20}$	–	2	Tsuji et al. (1997)	CO
	4.6 [a]	NML Cyg	300	$1.0\,10^{19}$	–	–	Justanount et al. (1996)	
H_2O	2.7 [a]	β Peg	1250	$7.0\,10^{18}$	–	2	Tsuji et al. (1997)	H_2O
	2.7 [a]	30g Her	1250	$2.0\,10^{19}$	–	2	Tsuji et al. (1997)	
	2.7 [a]	SW Vir	1250	$3.0\,10^{19}$	–	2	Tsuji et al. (1997)	
	2.7 [a]	NML Cyg	500	$2.0\,10^{19}$	–	–	Justanount et al. (1996)	
	6.2 [a]	NML Cyg	100	$2.0\,10^{19}$	–	–	Justanount et al. (1996)	
SO_2	7.3 [a]	UX Cyg	600	–	$7.5\,10^{46}$	1.8	Yamamura et al. (1999)	SO_2
	7.3 [e]	o Cet	600	–	$3.0\,10^{46}$	4.6	&	
	7.3 [a],[e]	T Cep	600	–	$1.4\ldots6.8\,10^{47}$	$4\ldots5.8$	de Jong et al. (1999)	
CO_2	4.2 [a]	SW Vir	1250	$1.2\,10^{17}$	–	2	Tsuji et al. (1997)	CO_2
	4.2 [a]	S Vir	1250	$1.5\,10^{18}$	–	2	Tsuji et al. (1997)	
	4.2 [a]	RT Vir	1000	$3\,10^{17}$	–	2	Tsuji et al. (1997)	
	4.2 [a]	NML Cyg	250	$2.0\,10^{18}$	–	–	Justanount et al. (1996)	
	$13.5\ldots16.2$ [a],[e]	(O-rich AGB)	650 – 1250	–	–	–	Justanount et al. (1998)	
	13.9 [e]	R Crt	650	–	$3.5\,10^{46}$ [*]	a few	Ryde et al. (1999)	
	13.9 [e]	R Dor	650	–	$4.8\,10^{45}$ [*]	a few	Ryde et al. (1999)	
	15.0 [e]	R Crt	160	–	$1.2\,10^{45}$ [*]	several 100	Ryde et al. (1999)	
	15.0 [e]	R Dor	150	–	$9.7\,10^{43}$ [*]	several 100	Ryde et al. (1999)	
	15.0 [a],[e]	R Cas	150	–	$5.9\,10^{44}$ [*]	several 100	Ryde et al. (1999)	
	$13.5\ldots16.2$ [e]	(O-rich AGB)	700	–	$\approx 1.0\,10^{46}$	a few	Cami et al. (1999)	
	15.0 [a],[e]	(O-rich AGB)	(different)	–	–	a few	Cami et al. (1999)	
HCN	$2.7\ldots4.2$ [a]	S Sct, V Aql, R Scl	–	–	–	–	Yamamura el al. (1998)	HCN
C_2H_2	$2.7\ldots4.2$ [a]	S Sct, V Aql, R Scl	–	–	–	–	Yamamura el al. (1998)	C_2H_2
	13.8 [a]	S Sct, V Aql, R Scl	1200 ± 300	$1.0\,10^{18}$	–	–	Yamamura el al. (1998)	

Table 4.6: Observed molecular bands and derived quantities regarding "warm molecular layers". The sample contains various O-rich AGB stars including Miras, semi-regular variables and one supergiant (NML Cyg). S Sct, V Aql, and R Scl are bright carbon-rich stars. The excitation temperature $T_{\rm exc}$ is deduced from the shape (i.e. the rotational fine-structure) of the bands by the authors cited. – = not stated, [*] = total number of molecules in the excited vibrational state, [a] appearance in absorption, [b] appearance in emission.

and the fact that those molecules which have been detected by observations infact occur in the time-dependent models in a layered structure shows that the levitation of matter by shocks may indeed be an important part of the explanation of the excess absorption and emission ascribed to the formation of *dense molecular layers*. The formation of dust shells reinforces the levitation of the gas by amplifying the shocks. Due to its large opacity the dust is accelerated by the radiation field, which result in a further compression of the gas. Hence, the formation of dense molecular layers by levitation must not alway be caused by the stellar pulsation, but can also be a consequence of the dust induced shock waves. The second effect implied by the dust is the backwarming of the underlying, dense molecular layers ascribed to occurrence of *warm molecular layers*. The backwarming is causally connected to a strong increase of the optical depth at considerable distance from the star, e.g. by dust formation. Thus, the formation of a new dust layer close to the star may provide both, a considerable increase of the molecular densities and a considerable warming of the layers below the new dust shell.

Proposition: It is proposed that molecular layers are located below dust shells at small radial distances. If this is true, it should be possible to observe an increase and a broadening of the molecular emission features when the star fades in the optical as a consequence of the formation of a new dust layer. The newly formed dust would cause a levitation of the atmosphere and a dense molecular layer would result. The dust will block the outgoing optical radiation and will imply a backwarming on the dense molecular layer below. Hence, the gas temperature in the molecular layer would increase accompanied by an increase of the rotational temperature which would result in a broadening of the vibrational bands.

4.4 Conclusions

This work has shown that molecular opacities have a strong influence on the structure and the dynamics of the winds of AGB stars. First, the molecules determine the overall density-level of the stellar atmosphere by their strong opacity, which forms the footpoint for any stellar outflow. Second, the molecular opacity can substantially modify the dust complex due to the coupled nature of the considered physical system.

Different approaches of treating the molecular opacity (Planck means, Rosseland means, constant value) can result in differences of up to 3 orders of magnitude. The use of Planck means (i.e. large opacities) leads to lower mass loss rates, lower outflow velocities, and lower dust-to-gas ratios in comparison to time-dependent models using Rosseland mean or constant opacities.

The hydrodynamic structure is roughly separated into two distinct regions: a region dominated by molecules at small radial positions (*molecular domain*) and a region dominated by dust at larger radii, $R > 2 \ldots 3\,R_0$, (*dust domain*).

> Large gas opacities in the *molecular domain* can result in a radiative acceleration which exceeds the gravitational deceleration ($\alpha^{\rm tot} > 1$). As a consequence, a pressure inverted zone and an additional mechanism to produce waves (shocks) are introduced.

Pressure inversions are not an artifact of the static equation of motion but remain and even re-occur in case of time-dependent models where perturbations due to waves are present. In spite of the local increase of the gas pressure in the inverted region, the gas pressure decreases globally in all models. Therefore, the physical demand of a vanishing pressure as outer boundary condition at infinity is not violated and the physical relevance of the models is not affected by the occurrence of local pressure inversions.

Pressure inversions caused by strong molecular opacities do occur in a particular *temperature window* at small radial positions where the temperature is still large compared to the temperatures in the circumstellar dust shell. Therefore, the inversions exist in a region which is strongly affected by strong shocks propagating outwards and by levitation of the atmosphere.

Models with a strong molecular opacity component exhibit a much smaller density resulting in less efficient dust formation and smaller mass loss rates and, therefore, might appear more alike optical carbon stars which are not totally obscured by dust. Therefore, stars which are observed with only intermediate amounts of dust in the circumstellar shell are possibly hindered to form more dust by a strongly absorbing gas which causes smaller densities. Such stars would, in addition, blow off dust particles of smaller sizes than those stars with lots of dust.

The decreasing outflow velocity and mass loss rate with increasing gas opacity underlines the importance of dust for the mass loss mechanism. Although the molecular opacity has an indirect influence the dust growth by lowering the density, it will very likely not be responsible for the wind generation in cool stars itself.

> Molecules will rather provide the chemical background as well as they will influence the amount of material available for dust formation than they will directly affect the mass loss mechanism in AGB stars.

The dust, in turn, influences the abundances of the molecular opacity sources by depleting the gas if dust is formed (*chemical dust blocking*) or by enriching the gas if temperatures become large enough for dust evaporation. This effect will influence different molecules depending on whether homomolecular or heteromolecular dust formation takes place.

In time-dependent models, shock waves levitate the atmosphere providing larger molecular densities at larger radial distances compared to static models. It can be concluded from the analysis of the abundances of mainly the involved molecular line opacity species that levitation possibly provides a natural explanation for the occurrence of molecular layers above the photosphere. In addition, if dust is formed efficiently, the backwarming could be responsible for an increase of the temperature in the molecular layers close to the star.

> Shock waves are responsible for the formation of *dense molecular layers* whereas backwarming by dust is responsible for an additional *warming* of the molecular layers.

Pure *dense molecular layers* are expected to occur in an atmosphere where no dust formation takes place, whereas *warm molecular layers* may occur in objects with effective dust formation. The levitation is a consequence of shock waves occurring in these models, which can be generated by pulsation, by radiative pressure on newly formed dust or by radiation pressure on molecules.

"Ich bin der festen Überzeugung, daß die Natur viel einfacher ist, als wir denken."
Erwin Sedlmayr, July 1998

Chapter 5

Summary & Outlook

This thesis has explored the role of molecular opacities in the atmospheres and the circumstellar dust shells of AGB stars. The investigations have been performed in the framework of time-dependent model calculations which are based on a self-consistent treatment of hydrodynamics, chemistry, radiative transfer, and dust formation, growth and evaporation. The radiative transfer problem has been solved in the grey approximation. Models computed with Planck mean gas opacities illustrate the maximum effect whereas models with Rosseland mean or constant gas opacities illustrate the minimum effect gas opacities can have on the structure and the dynamics of a circumstellar shell and therefore on the dust formation.

New Planck and Rosseland mean gas opacity tables have been calculated for temperatures $T \epsilon$ [500K, 10 000K], total hydrogen densities $n_{<\mathrm{H}>}\ \epsilon\ [10^5\mathrm{cm}^{-3}, 10^{15}\ \mathrm{cm}^{-3}]$ and various elemental abundances including the molecular line opacity for CO, TiO, SiO, H_2O, CH, CN, C_2, C_3, HCN, and C_2H_2 beside several continuum sources. Both mean opacities are very similar at high temperature where continuum absorption and scattering dominate. Differences of up to 3 orders of magnitude occur at low temperatures in the molecular domain caused by the strong frequency dependence of the molecular opacities.

The analysis of the mean opacities has shown that the oxygen-bearing molecular opacity species TiO, SiO, and H_2O can contribute to the carbon-rich Planck mean gas opacities below 1000 K but not to the Rosseland mean gas opacities. The re-computation of the chemical gas composition on top of carbon-rich hydrodynamic models has shown that considerable amounts of oxygen-bearing molecules are present at large stellar distances even in the carbon-rich case. Oxygen-bearing molecules gain importance if a large amount of the carbon is consumed into dust.

A comparison of mean dust and mean gas opacities has revealed that the carbon-rich dust opacities are larger than the carbon-rich gas opacities at degrees of condensation larger than $\approx 10\%$ (depending on temperature and gas density). This is the basic reason for the strong influence of the dust on the hydrodynamic and thermodynamic structure of circumstellar shells. The difference between the oxygen-rich dust (SiO, iron) and the oxygen-rich gas opacity is much smaller than the corresponding differences in the carbon-rich case. Iron is negligible as a dust opacity source due to its very small opacity.

Molecular opacities have a strong influence on the structure and the dynamics of the wind for two reasons: First, the molecular opacities dominate the structure of the stellar atmosphere, which constitutes the base of the stellar wind. Second, radiation pressure on molecules provides a non-negligible force-term in the equation of motion and can have a direct impact on the dynamics of the wind.

The calculation of the initial static Planck models has revealed the occurrence of local pressure inversions which occur only in the carbon-rich case. The local pressure inversion coincides well with the maximum particle density of C_3 in the (T, ρ) plane. A closer inspection of the inner regions of the time-dependent models calculated with Planck mean gas opacities has shown that pressure inversions remain and even re-occur if perturbations caused by the interior pulsation are present. It has further been argued that such inversions are not Rayleigh-Taylor instable since the net acceleration of the affected mass elements is directed outwards in contrast to a mass element being affected by only gravitational acceleration when the net acceleration is directed inwards. Since pressure inversions are local phenomenons, the physical demand of a vanishing pressure as outer boundary condition at infinity is not violated and the physical relevance of the models is not affected by the occurrence of local pressure inversions.

The occurrence of dust enhanced shocks in models of cool pulsating stars as presented by Fleischer et al. (1992, 1994), Winters et al. (1997), and by Höfner et al. (1992, 1994, 1997) is a definite sign for the strong influence of the dust on the hydrodynamic and thermodynamic structure of the atmosphere by its large opacity. The occurrence of pressure inversions indicates that also the molecules can have an important influence especially on the inner, dust-free regions of a circumstellar shell. Such pressure inversions are caused by a strong peak in the gas opacity which, in addition, introduces small perturbations into the velocity field. If dust is formed, radiation pressure on dust causes an amplification of these molecular induced waves. Shocks, which are caused by the interior pulsation, are damped, party transmitted and partly reflected when they accounter a finite region of increasing density.

Time-dependent models of circumstellar dust shells with a strong molecular absorption component seem to exhibit rather a chaotic than a multiperiodic behavior, but more detailed investigations are needed to clarify this point.

Strong gas absorption causes the atmosphere to be less dense in general than an atmosphere with small gas absorption at the same optical depth. Consequently, dust formation is less efficient in models with strong molecular absorption resulting in smaller mass loss rates, smaller outflow velocities, and smaller dust-to gas ratios. Since favorable conditions for effective dust formation occur less frequent in a Planck model than in a model calculated with smaller gas absorption coefficients (Rosseland means, constant value), the grain size distribution is less homogeneous. Beside a larger amount of small particles, compared to a Rosseland model, also a few large particles would be injected into the ISM. The particle sizes in the Planck model are generally smaller than in a model calculated with a smaller gas absorption coefficients.

The analysis of the chemical composition of the time-dependent models, regarding in particular the molecular species included in the opacity calculation, has revealed a layered structure of the molecule's density: one layer comparable to the static models in or very close to the photosphere and another one either caused by levitation due to shocks or by levitation due to radiation pressure on molecules at larger radial positions. Radiation pressure on dust amplifies this effect, and provides an additional backwarming of these levitated regions. The comparison of column densities with the values estimated from the observations for mainly Miras and semi-regular variables shows a promising degree of agreement, in particular concerning a dust-free oxygen-rich model. The levitation by shock waves or by radiation pressure on molecules seems, therefore, to provide a natural explanation for the generation of the so-called "warm molecular layers" which more correctly should be called *dense molecular layers*.

It has been shown, however, that in the static case the frequency dependence of the gas opacity can influence substantially the thermodynamic structure of a stellar atmosphere. Furthermore, non-grey models computed with a moderate number of frequency points ($\approx 20 \ldots 50$) can yield more realistic atmospheric structures than models calculated with mean opacities (Helling & Jørgensen 1998). Since dust formation is very sensitive to small changes in the temperature (whereas dust evaporation is not), more efforts have to be undertaken to understand the role of molecules also with regard to the thermodynamic structure of a circumstellar envelope. Such investigations must combine time-dependent hydrodynamical model calculations, as presented in this work, and a frequency-dependent radiative transfer in a self-consistent way together with the dust complex. A possible way to attack this problem would be the application of a frequency dependent radiative transfer treatment on a reduced grid of frequencies in order to include the molecular line opacities discussed in this work.

The analysis of high resolution spectra has shown that turbulent motions in stellar atmospheres cause an additional line broadening beside the thermal and the Doppler broadening (e.g Fokin et al. 1996, Carpenter & Robinson 1997). Therefore, a further topic to be investigated is the possible influence of turbulent motions on the dust formation and the chemical composition of the gas, for instance by locally favored conditions for dust growth accompanied by local backwarming.

The Reynolds number, which is the control parameter of a viscous flow and which indicates whether the flow is laminar or turbulent, can be estimated for a hydrogen-dominated gas by (Lang 1992)

$$Re \approx 2\,10^4 \,\sqrt{T}\,\rho\, v\, l, \tag{5.1}$$

and for a helium-dominated (hydrogen-deficient) gas by

$$Re \approx 1.09\,10^4 \,\sqrt{T}\,\rho\, v\, l, \tag{5.2}$$

with l being the size of a turbule (or a characteristic scale), v the velocity and ρ the density at temperature T. If the Reynolds number $Re > 10^4$ (e.g. Birkhoff 1960), the gas is not able to damp small perturbations by its viscosity. Small disturbances are then amplified and may prevail over some time. Since energy is dissipated by viscous friction, energy supply is needed to maintain the turbulent motion (e.g. by convection).

For given T, ρ, and v a scale length l can be estimated from Eqs. (5.1) and (5.2) in a typical astrophysical medium such that $Re = 10^4$.

For typical values of an inner circumstellar shell, the critical length is $\approx 2\,10^2$ cm in order to enter the turbulent regime. Hydrostatic scale heights of such regions for the models discussed in this thesis are about $10^{-2}\,R_\star$ and, hence $Re \gg 10^4$ (compare Table 5). However, although the inner region of circumstellar shells seem to fall into

object	T_{gas} [K]	ρ_{gas} [g/cm^3]	v [cm/s]	reference	**Re**	**l** [cm]
inner CSE	3000	10^{-10}	$5\,10^5$	this work	$55\,l$	$1.5\,10^{11}$ [a]
brown dwarf ($\tau \approx 10^{-3}$)	1132	$5.49\,10^{-5}$	10^5 [c]	Tsuji et al. (1997)	$10^{11}\ldots10^{12}$	$4\ldots7\,10^5$ [b]
Wolf Rayet star	1400	10^{-19}	$2.5\,10^8$	Beck & Sedlmayr (1998)	$10^{-5}\,l$	$> 10^{10}$ ($\Leftrightarrow Re > 10^4$)
molecular cloud	20	$5\,10^{-21}$	$5\,10^4$ [c]	Blitz (1987)	$2\,10^{-11}\,l$	$> 10^{14}$ ($\Leftrightarrow Re > 10^4$)
cold ISM	80	$3\,10^{-24}$	10^5 [c]	Heiles & Kulkarni (1987)	$5\,10^{-14}\,l$	$> 10^{17}$ ($\Leftrightarrow Re > 10^4$)
warm ISM	6000	$3\,10^{-24}$	10^5 [c]	Heiles & Kulkarni (1987)	$4\,10^{-13}\,l$	$> 4\,10^{16}$ ($\Leftrightarrow Re > 10^4$)

Table 5.1: Estimations of astrophysical Reynolds numbers and critical scale lengths l

[a] static scale hight: $l \approx \frac{p_{gas}}{g\,\rho_{gas}}$ with $g = 1.26$ cm/s^2
[b] like [a] but $g \approx 10^5$ cm/s^2 ($T_{eff} = 1000$ K, C/O=0.43)
[c] typical microturbulent velocity deduced from observations

the turbulent regime, it has to be investigated whether turbulent motions can become strong enough to impose a considerable effects on the system compared to shocks or radiation pressure on molecules.

A somewhat different picture may be drawn for Brown dwarfs where no strong shocks influence the atmosphere. Brown Dwarfs are thought to be a perfect example for a static atmosphere since also radiation pressure on molecules seems negligible due to the very low luminosity of these stars. Therefore, turbulent motion may well influence the hydrodynamics and maybe even the local thermodynamics of such systems and thus, may modify the dust complex.

Similar considerations are possible for other astrophysical objects like Wolf Rayet stars[1], molecular clouds, and the ISM. Table 5 indicates that many astrophysical situations are characterized by large Reynolds numbers.

Turbulent motions are mathematically defined by a Fourier spectrum of the flow: if it is continues, turbulence occurs. The analyzes of the Fourier spectrum gives information about the size of the smallest occurring eddies, and the number of different scales to be numerically resolved (Griebel et al. 1995). It is widely believed that the turbulent motion in astrophysical environments are caused by convection (e.g. Zahn 1980), which is, however, a multi-scale phenomenon in time and space. The number of degree of freedoms of a fully developed three-dimensional turbulent flow, or alternatively, the number of grid points N, scales with the Reynolds number Re as $N \sim Re^{9/4}$, whereas present day computers allow for only a percentage resolution of $\approx 10^9$ spatial scales (see f.e. Kupka 1996, Canuto 1997). Hence, it is only possible to numerically resolve a flow that is considerable less turbulent than the real flow one wants to study.

[1]Wolf Rayet stars are luminous, massive, evolved, hydrogen-poor, hot stars ($T_\star$ = 25 000 ... 30 000 K) which, nevertheless, are observed to form large amounts of dust in their high speed wind with $v \approx 1100 \ldots 3500$ km/s (Lang 1992).

Appendix A

List of natural constants

name	symbol	value	dimension [cgs]	ref.
	π	3.141592653589793		
velocity of light	c	$2.99792458 \times 10^{10}$	cm s^{-1}	(1)
Planck's constant	h	$6.6260755 \times 10^{-27}$	erg s	(1)
gravitational constant	G	6.67259×10^{-8}	$cm^3 g^{-1} s^{-2}$	(1)
elementary charge	e	4.803242×10^{-10}	e.s.u.	(1)
Stefan-Boltzmann constant	σ	5.67051×10^{-5}	erg s^{-1} cm^{-2} K^{-4}	(1)
Boltzmann constant	k	1.380658×10^{-16}	erg K^{-1}	(1)
electron rest mass	m_e	$9.1093897 \times 10^{-28}$	g	(1)
atomic mass unit	a.m.u.	1.66053×10^{-24}	g	(2)
atomic mass of hydrogen	m_H	1.007825	a.m.u.	(2)
		1.678341×10^{-24}	g	
solar mass	$M_\odot$	1.9891×10^{33}	g	(1)
solar luminosity	$L_\odot$	3.8268×10^{33}	erg s^{-1}	(1)
solar radius	$R_\odot$	6.9599×10^{10}	cm	(1)

Table A.1: (1) = Lang (1992), (2) = Gerthsen et al. (1989)

Bibliography

Achmad, L., Lamers, H., Pasquini, L. (1997). Radiation driven wind models for A, F and G supergiants. *A&A* **320**, 196–208.

Alexander, D. R., Ferguson, J. W. (1994). Low–temperature Rosseland opacities. *ApJ* **437**, 879–891.

Allain, T. (1996). *Photodestruction and growth of interstellar polycyclic aromatic hydrocarbons*. Dissertation, Technische Universität Berlin, FRG.

Allard, F., Hauschildt, P. H., Baraffe, I., Chabrier, G. (1996). Synthetic spectra and mass determination of the brown dwarf Gliese 229B. *ApJ* **465**, L123–L127.

Allard, F., Hausschild, P., Miller, S., Tennyson, J. (1994). The influence of H2O line blanketing on the spectra of cool dwarf stars. *ApJ* **426**(2), L39–L41.

Allen, C. W. (1973). *Astrophysical Quantities*. London: The Athlone Press.

Anders, E., Grevesse, N. (1989). Abundances of the elements: Meteoric and solar. *Geochimica et Cosmochimica Acta* **53**, 197–214.

Aoki, W., Tsuji, T. (1997). High resolution infrared spectroscopy of CN and NH lines: nitrogen abundnce in oxygen-rich giants through K to late M. *A&A* **328**, 175–186.

Aringer, B., Jørgensen, U. G., Langhoff, S. R. (1997). SiO rotation-vibration bands in cool giants. *A&A* **323**, 202–210.

Arndt, T. U., Fleischer, A. J., Sedlmayr, E. (1997). Circumstellar Dust shells around Long-period Variables. VI. An approximative formula for the mass loss rate of C-rich stars. *A&A* **327**, 614–619.

Asplund, M., Gustafsson, B. (1996). Are the declines of R Coronae Borealis stars caused by super-Eddington luminosities? In C. S. Jeffery und U. Heber (Hrsg.), *Hydrogen-Deficient Stars*, pp. 39–42. ASP Conf. Ser. 96.

Asplund, M., Gustafsson, B., Kameswara Rao, N., Lambert, D. L. (1998). Abundance similarities between the R CrB star V854 Cen and the born-again Sakurai's object. *A&A* **332**(2), 651–660.

Asplund, M., Gustafsson, B., Kiselman, D., Eriksson, K. (1997). Line-blanketed model atmospheres for R Cornonae Borealis stars and hydrogen-deficient carbon stars. *A&A* **318**(2), 521–534.

Baschek, B., Scholz, M., Wehrse, R. (1991). The parameter R and T_{eff} in stellar models and observations. *A&A* **246**, 374–382.

Beck, H., Sedlmayr, E. (1998). Dust formation in the environments of hot stars. In T. Hartquist und D. Williams (Hrsg.), *The Molecular Astrophysics of Stars and Galaxies*, pp. 371–390. Oxford Science Pub.

BECK, H. K. B. (1993). *Ionization, Chemistry and Dust Formation in the Outflows of Classical Novae and Red Giants.* Dissertation, Technische Universität, Berlin, FRG.

BECK, H. K. B., GAIL, H.-P., HENKEL, R., SEDLMAYR, E. (1992). Chemistry in circumstellar shells. I. Chromospheric radiation fields and dust formation in optically thin shells of M-giants. *A&A* **265**, 626–642.

BIRKHOFF, G. (1960). *Hydrodynamics* (2nd ed.). Princeton, New Jersey: Princeton University Press.

BIZZARRI, A., HUBER, M., NOELS, A., GREVESSE, N., BERGESON, S., TSEKERIS, P., LAWLER, J. (1993). Ti-II transition probabilities and radiative lifetimes in Ti^+ and the solar titanium abundance. *A&A* **273**, 707–718.

BLITZ, L. (1986). The structure of molecular clouds. In G. Morfill und M. Scholer (Hrsg.), *Physical Processes in Interstellar Clouds*, Dortrecht, pp. 35–58. Reidel.

BOOTHROYD, A., SACKMANN, I.-J., AHERN, S. C. (1993). Prevention of high–luminosity carbon stars by hot bottom burning. *ApJ* **416**, 762–768.

BOWEN, G. H. (1988). Dynamical modelling of long-period variable star atmospheres. *ApJ* **329**, 299–317.

CAMI, J., DE JONG, T., TIELENS, A. G. G. M., JUSTTANONT, K., WATERS, L. B. F. M., YAMAMURA, I. (1999). Gas phase CO_2 around O-rich AGB stars. In T. Le Bertre, A. Lèbre, und C. Waelkens (Hrsg.), *IAU Symp. 191: AGB stars*, pp. Poster 2–30. Kluwer.

CANUTO, V. M. (1997). Sub-grid scale modeling: correct models and others. *ApJ* **478**, 322–325.

CARBON, D., GINGERICH, O., LATHAM, D. (1969). Model Atmospheres for Cool Dwarf Stars. In S. Kumar (Hrsg.), *Low Luminosity Stars*, New York. Gordon and Breach.

CARPENTER, K. G., ROBINSON, R. D. (1997). GHRS observations of cool low–gravity stars. III. Plasma flows and turbulence in the outer atmosphere of α orionis. *ApJ* **479**, 970–983.

CARSON, T., LUO, G., SHARP, C. (1992). Molecular Opacities and Stellar Structure. *Rev.Mex.Astron.Astrof* **23**, 217–221.

CHASE JR., M. W., DAVIES, C. A., DOWNEY JR., J. R., FRURIP, D. J., MCDONALD, R. A., SYVERUD, A. N. (1985). JANAF Thermochemical Tables. In *J. Phys. Chem. Ref. Dat., Vol.14 Suppl.1.* National Bureau of Standards.

CHERCHNEFF, I., BARKER, J. R., TIELENS, A. G. G. M. (1992). Polycyclic Aromatic Hydrocarbon formation in carbon-rich stellar envelopes. *ApJ* **401**, 269–287.

DALGARNO, A. (1962). *The Scattering of light by Atomic Systems*, Band III of *Spectral Reflectivity of the Earth Atmosphere.* Geoph.Corp. of America.

DAY, K. (1974). A possible identification of the 10-micron feature. *ApJ* **192**, L15–L17.

DE JONG, T., YAMAMURA, I., CAMI, J., ONAKA, T., WATERS, L. B. F. M. (1999). Discovery of the SO_2 7.3 microns Band in Oyxgen-rich Miras. In T. Le Bertre, A. Lèbre, und C. Waelkens (Hrsg.), *IAU Symp. 191: AGB stars*, pp. Poster 2–33. Kluwer.

DOMINIK, C., GAIL, H.-P., SEDLMAYR, E. (1989). The size distribution of dust particles in a dust-driven wind. *A&A* **223**, 227–236.

DOYLE, R. (1968). *The continuous spectrum of the hydrogen quasi-molecule.* Dissertation, Harvard University, Harvard, USA.

Ekberg, U., Eriksson, K., Gustafsson, B. (1986). Line blanketing in model atmospheres of carbon stars. *A&A* **167**, 304–310.

Fleischer, A. J. (1994). *Hydrodynamics and Dust Formation in the Circumstellar Shells of Miras and Long–Period Variables.* Dissertation, Technische Universität, Berlin, FRG.

Fleischer, A. J., Gauger, A., Sedlmayr, E. (1992). Circumstellar Dust shells around Long-period Variables. I. Dynamical models of C-stars including dust formation, growth and evaporation. *A&A* **266**, 321–339.

Fleischer, A. J., Gauger, A., Sedlmayr, E. (1995). Circumstellar Dust shells around Long-period Variables. III. Instability due to an exterior κ–mechanism caused by dust formation. *A&A* **297**, 543–555.

Fokin, A. B., Gillet, D., Breitfellner, M. G. (1996). Pulsating motions and turbulence in δ Cephei. *A&A* **307**, 503–515.

Frenklach, M., Feigelson, E. D. (1989). Formation of polycyclic aromatic hydrocarbons in circumstellar envelopes. *ApJ* **341**, 372–384.

Gail, H.-P., Sedlmayr, E. (1984). Formation of crystalline and amorphous carbon grains. *A&A* **132**, 163–167.

Gail, H.-P., Sedlmayr, E. (1985). Dust formation in stellar winds. II. Carbon condensation in stationary, spherically expanding winds. *A&A* **148**, 183–190.

Gail, H.-P., Sedlmayr, E. (1986). The primary condensation process for dust around late M-type stars. *A&A* **166**, 225–236.

Gail, H.-P., Sedlmayr, E. (1988). Dust formation in stellar winds. IV. Heteromolecular carbon grain formation and growth. *A&A* **206**, 153–168.

Gail, H.-P., Sedlmayr, E. (1998). Dust formation in M stars. In T. Hartquist und D. Williams (Hrsg.), *The Molecular Astrophysics of Stars and Galaxies*, Oxford, GB, pp. 285. Oxford Science Pub.

Gauger, A. (1997). private communication

Gauger, A., Gail, H.-P., Sedlmayr, E. (1990). Dust formation, growth and evaporation in a cool pulsating circumstellar shell. *A&A* **235**, 345–361.

Gehrz, R. D. (1989). Sources of stardust in the galaxy. In L. J. Allamandola und A. G. G. M. Tielens (Hrsg.), *Interstellar Dust*, Dordrecht, pp. 445–453. Kluwer Academic Publishers.

Gerthsen, C., Kneser, H. O., Vogel, H. (1989). *Physik* (16. ed.). Berlin: Springer.

Geyer, R. (1997). Zirkumstellare Staubhüllen Langperiodisch Veränderlicher als dynamische Systeme. Diplomarbeit, TU Berlin, FRG.

Goeres, A. (1993). The formation of PAHs in C–type star environments. *Rev. Mod. Astron.* **6**, 165–177.

Goeres, A., Sedlmayr, E. (1991). On the nucleation mechanism of effective fullerite condensation. *Chem. Phys. Lett.* **184**(4), 310–317.

Goeres, A., Sedlmayr, E. (1993). Hydrogen-blocking in C60-formation theories. *Fullerenes in Science and Technology* **1**(4), 563–570.

Goorvitch, D. (1994). Infrared CO Line List for the $X^1\Sigma^+$ State . *ApJSS* **95**, 535–552.

Grevesse, N., Lambert, D., Sauval, A., van Dishoeck, E., Farmer, C., R.H., N. (1991). Vibration-rotation bands of CH and the solar carbon abundance. *A&A* **242**, 488–495.

Grevesse, N., Noels, A. (1993). Cosmic abundance of the Elements. In *Origin and evolution of the elements*, Cambridge, pp. 14–25. Univerity Press.

Griebel, M., Dornseifer, T., Neuenhoeffer, T. (1995). *Numerische Simulation in der Strömungsmechanik*. Scientific Computing. Braunschweig, Wiesbaden: Vieweg.

Gustafsson, B., Bell, R. A., Eriksson, K., Nordlund, Å. (1975). A Grid of Model Atmospheres for Metal-deficient Giant Stars I. *A&A* **42**, 407–432.

Gustafsson, B., Jørgensen, U. G. (1994). Models of late–type stellar photospheres. *A&AR* **6**, 19–65.

Gustafsson, B., Ryde, N. (1996). Carbon stars and nucleosynthesis in galaxies. In R. F. Wing (Hrsg.), *IAU Symp. 177: The Carbon Star Phenomenon*, Dordrecht, pp. in press. Kluwer Academic Publishers.

Habing, H. (1996). Circumstellar envelopes and Asymptotic Giant Branch stars. *A&AR* **7**, 97–207.

Hashimoto, O. (1995). Infrared properties of circumstellar dust envelopes of oxygen–rich asymptotic giant branch stars. *ApJ* **442**, 286–295.

Hedgecock, I., Naulin, C., Costes, M. (1995). Measurments of radiative lifetimes of TiO ($A^3\Phi$, $B^3\Pi$, $C^3\Delta$, $c^1\Phi$, $f^1\Delta$, $E^3\Pi$). *A&A* **304**, 667–677.

Heiles, C., Kulkarni, S. (1986). Diffuse interstellar gas. In G. Morfill und M. Scholer (Hrsg.), *Physical Processes in Interstellar Clouds*, Dortrecht, pp. 13–33. Reidel.

Helling, C. (1996). Application of Opacity Sampling (OS) and Opacity Distribution Functions (ODF) to Model Calculations of Cool Giants. Diplomarbeit, TU Berlin and Niels Bohr Institut, Copenhagen.

Helling, C., Jørgensen, U. G. (1998). Optimizing the opacity sampling method. *A&A* **337**, 477–486.

Helling, C., Jørgensen, U. G., Plez, B., Johnson, H. R. (1996). Formation of PAHs, polyynes, and other macromolecules in the photosphere of carbon stars. *A&A* **315**, 194–203.

Höfner, S. (1997). private communication

Höfner, S., Dorfi, E. A. (1992). Dust formation in winds of long-period variables. II. Dust energetics, optical properties, chemistry, time scales. *A&A* **265**, 207–215.

Höfner, S., Dorfi, E. A. (1997). Dust formation in winds of long–period variables IV. Atmospheric dynamics and mass loss. *A&A* **319**, 648–654.

Höfner, S., Feuchtinger, M. U., Dorfi, E. A. (1995). Dust formation in winds of Long–period variables. III. Dynamical models and confirmation of a dust–induced κ–mechanism. *A&A* **297**, 815–827.

Höfner, S., Jørgensen, U. G., Loidl, R., Aringer, B. (1998). Dynamical model atmospheres of AGB stars. I. Atmospheric structure and dynamics. *A&A* **340**, 497–507.

Hubeny, I. (1997). *Stellar Atmospheres: Theory and Observations*, Band 497 of *Lecture Notes in Physics*, Chapter Stellar Atmospheres Theory: An Introduction, pp. 1–68. EADN Astrophysics School IX, Brussels, Belgium 1996: Springer.

Jeong, K. S., Winters, J. M., Sedlmayr, E. (1999). Dust formation in oxygen-rich circumstellar shells around long-period variables. In T. Le Bertre, A. Lèbre, und C. Waelkens (Hrsg.), *IAU Symp. 191: AGB stars*, pp. 233–238, in press. Kluwer.

John, M. (1995). Bildung von Eisen–Clustern in kühlen Sternwinden. Diplomarbeit, Technische Universität, Berlin, FRG.

John, T. (1988). Continuous absorption by the negative hydrogen ion reconsidered. *A&A* **193**, 189–192.

Jørgensen, U. (1989). The infrared spectrum of TX Piscium. *ApJ* **344**, 901–906.

Jørgensen, U. G. (1996). private communication

Jørgensen, U., Jensen, P. (1993). The Dipole Moment Surface and the Vibrational Transition Moments of H_2O . *J. Mol. Spect.* **161**, 219–242.

Jørgensen, U., Larsson, M. (1990). Molecular opacities of astrophysical interest: the $A^2\Pi$–$X^2\Sigma^+$ system of CN. *A&A* **238**, 424–434.

Jørgensen, U., Larsson, M., Iwamae, A., Yu, B. (1996). Line intensities for CH and their application to stellar atmospheres . *A&A* **315**, 204–211.

Jørgensen, U. G. (1990). The complete system of HCN combination bands in the spectrum of carbon stars. *A&A* **232**, 420–435.

Jørgensen, U. G. (1994a). Dominating Molecules in the Photospheres of Cool Stars. In U. G. Jørgensen (Hrsg.), *Molecules in the Stellear Environment*, Berlin, pp. 29–48. Springer.

Jørgensen, U. G. (1994b). Effects of TiO in stellar atmospheres. *A&A* **284**, 179–186.

Jørgensen, U. G., Almlöf, J., Siegbahn, P. E. M. (1989). Complete active space self-consistent field calculations of the vibrational band strengths for C_3. *ApJ* **343**, 554–561.

Jørgensen, U. G., Johnson, H. R. (1992). Radiative force on molecules and its possible role for mass loss in evolved AGB stars. *A&A* **265**, 168–176.

Jørgensen, U. G., Johnson, H. R., Nordlund, Å. (1992). Effects of sphericity in carbon star atmospheres. *A&A* **261**, 263–273.

Jun, B.-I., Jones, T., Norman, M. (1996). Interaction of Rayleigh-Taylor fingers and circumstellar cloudlets in young supernova remnants. *ApJ* **468**, L59–L63.

Jun, B.-I., Norman, M., Stone, J. (1995). A numerical study of Rayleight-Taylor instability in magnetic fluids. *ApJ* **453**, 332–349.

Justtanont, K., de Jong, T., Helmich, F. P., Waters, L. B. F. M., de Graauw, T., Loup, C., Izumiura, H., Yamamura, I., Beintema, D. A., Lahuis, F., Roelfsema, P. R., Valentijn, E. A. (1996). The ISO-SWS spectrum of NML Cyg. *A&A* **315**, L217–L220.

Justtanont, K., Feuchtgruber, H., de Jong, T., Cami, J., Waters, L., Yamamura, I., Onaka, T. (1998). Discovery of CO_2 emission in AGB stars with 13 μm dust feature. *A&A* **330**, L17–L20.

Karzas, W., Latter, R. (1961). Electron radiative transitions in a Coulomb field. *ApJS* **6**, 167–213.

Knapp, G. R. (1985). Mass Loss from evolved stars. IV. The dust-to-gas ratio in the envelopes of Mira variables and carbon stars. *ApJ* **293**, 273–280.

Köhler, T. M., Gail, H.-P., Sedlmayr, E. (1997). MgO dust nucleation in M–stars: Calculation of cluster properties and nucleation rates. *A&A* **320**, 553–567.

Krüger, D. (1997). *A computational multi-component method for modeling the evolution of size distribution functions and its application to cosmic dust grains*. Dissertation, Technische Universtät Berlin, Berlin, FRG.

Krüger, M. (1992). Koagulation von Staubteilchen in den Winden Roter Riesen. Diplomarbeit, Technische Universität, Berlin, FRG.

Kupka, F. (1996). Beyond mixing length theory. In S. J. Adelman, F. Kupka, und B. W. Weiss (Hrsg.), *Model atmospheres and spectrum systhesis*, pp. 73–85.

Lang, K. R. (1992). *Astrophysical Data: Planets and Stars*. New York: Springer-Verlag.

Langhoff, S., Bauschlicher Jr., C. (1993). A theoretical study of the electric dipole moment function of SiO. *Chem. Phy. Letters* **211**(4,5), 305–311.

Larsson, M. (1983). Conversion formulas between radiative lifetimes and other dynamical variables for spin-allowed electronic transitions in diatomic molecules. *A&A* **128**, 291–298.

Le Bertre, T. (1997). *Stellar Atmospheres: Theory and Observations*, Band 497 of *Lecture Notes in Physics*, Chapter Cool star winds and mass loss: Observations, pp. 133–157. EADN Astrophysics School IX, Brussels, Belgium 1996: Springer.

Loidl, R., Höfner, S., Jørgensen, U. G., Aringer, B. (1999). Dynamic model atmospheres of AGB stars. II. Synthetic near infrared spectra of carbon stars. *A&A* **342**, 531–541.

Lucy, L. B. (1971). The formation of resonance lines in extended atmospheres. *ApJ* **163**, 95–110.

Lucy, L. B. (1976). Mass loss by cool carbon stars. *ApJ* **205**, 482–491.

Maciel, W. J. (1976). Mass loss from Mira variables by the action of radiation pressure on molecules. *A&A* **48**, 27–31.

Mamon, G. A., Glassgold, A. E., Huggins, P. J. (1988). The photodissociation of CO in circumstellar envelopes. *ApJ* **328**, 797–808.

Mihalas, D. (1965). Model atmospheres and line profiles for early-type stars. *ApJS* **9**, 321–438.

Mihalas, D. (1978). *Stellar Atmospheres* (2^{nd} ed.). San Francisco: W. H. Freeman and Company.

Mihalas, D., Weibel Mihalas, B. (1984). *Foundations of Radiation Hydrodynamics*. Oxford University Press.

Neuforge, C. (1993). Low temperature Rosseland mean opacities. *A&A* **274**, 818–820.

Ohnaka, K., Tsuji, T. (1998). Quantitative analysis of carbon isotopic ratios in carbon stars. II. The effect of model atmosphere on the iso-intensity method. *A&A* **335**, 1018–1024.

Ohnaka, K., Tsuji, T., Aoki, W., Yamamura, I. (1998). Analysis of Infrared Spectra of Carbon Stars Observed by the ISO SWS. *Ap&SS* **255**, 369–375.

Patzer, A. B. C. (1998). *Non–equilibrium effects on chemistry and dust formation in circumstellar outflows*. Dissertation, Technische Universtät Berlin, Berlin, FRG.

Patzer, A. B. C., Köhler, T., Sedlmayr, E. (1995). Primary astrophysical dust formation: Laboratory desiderata. *Planet.& Sp.Sci.* **43**, 1233–1239.

Peach, G. (1970). Continuous absorption coefficients for non-hydrogenic atoms. *Mem. R. astr.* **73**, 1–123.

Pearse, R., Gaydon, A. (1965). *The Identification of Molecular Spectra* (3 ed.). London: Chapman & Hall LDT.

PLEZ, B., BRETT, J. M., NORDLUND, A. (1992). Spherical opacity sampling model atmospheres for M giants I. Techniques, data and discussion. *A&A* **256**, 551–571.

PLEZ, B., SMITH, V. V., LAMBERT, D. L. (1993). Lithium abundances and other clues to envelope burning in Small Magellanic Cloud Asymptotic Giant Branch Stars. *ApJ* **418**, 812–831.

QUERCI, F., QUERCI, M., TSUJI, T. (1974). Model atmospheres for C type stars. *A&A* **31**, 265–282.

RADZIG, A., SMIRNOV, B. (1985). *Reference Data on Atoms, Molecules and Ions*, Band 31 of *Springer Series in Chemical Physics*. Springer Verlag.

RICHTMYER, R. D., MORTON, K. W. (1967). *Difference methods for initial-value problems* (2^{nd} ed.). New York: John Wiley & Sons.

RUSSEL, S., DOPITA, M. (1992). Abundances of the heavy elements in the magellanic clouds. III Interpretation of results. *ApJ* **384**, 508–522.

RYDE, N., ERIKSSON, K., GUSTAFSSON, B. (1999). The nature of the circumstellar CO_2 emission from M giants. *A&A* **341**, 579–586.

SCHOLZ, M., TSUJI, T. (1984). The effects of spherical extension upon the photospheric structure and spectrum of red giants: comparison of M and C stars. *A&A* **130**, 11–18.

SCHRÖDER, K.-P., WINTERS, J. M., SEDLMAYR, E. (1999). Tip-AGB stellar evolution in the presence of a pulsating, dust–induced "superwind". *A&A* **submitted**.

SEATON, M. J., YAN, Y., MIHALAS, D., PRADHAN, A. K. (1994). Opacities for stellar envelopes. *MNRAS* **266**, 805–828.

SEDLMAYR, E., WINTERS, J. M. (1996). Grain Formation in the Winds of Cool Red Giant Stars. In R. F. Wing (Hrsg.), *IAU Symp. 177: The Carbon Star Phenomenon*, Dordrecht, pp. in press. Kluwer Academic Publishers.

SHARP, C. M. (1992). Molecular opacities for solar and enhanced CNO abundances: relevance for accretion disks. *A&AS* **94**, 1–12.

SOMERVILLE, W. B. (1964). The continuous absorption coefficient of the negative hydrogen molecular ions. *ApJ* **139**, 192–197.

STEIN, W., GAUSTAD, J., GILLETT, F. (1969). Circumstellar infrared emission from 2 pecular objects 1 Aqr and R CrB. *ApJ* **155**, L3–L6.

TREFFERS, R., COHEN, M. (1974). High-resolution spectra of cool stars in the 10- and 20-micron regions. *ApJ* **188**, 545–552.

TSCHARNUTER, W. M., WINKLER, K.-H. (1979). A method for computing selfgravitating gas flows with radiation. *Comp.Phys.Comm.* **18**, 171–199.

TSUJI, T. (1973). Molecular abundances in stellar atmospheres II. *A&A* **23**, 411–431.

TSUJI, T. (1994). Astrophysical Applications of Approximate Methods of Molecular Opacities – from Stars to Substellar Brown Dwarfs. In U. Jørgensen (Hrsg.), *Molecules in the Stellar Environment*, Berlin, Heidelberg, pp. 79–97. Springer.

TSUJI, T., OHNAKA, K., AOKI, W., YAMAMURA, I. (1997). Warm molecular envelopes of M giants and Miras: a new molecule forming region unmasked by the ISO SWS. *A&A* **320**, L1–L4.

TSUJI, T., OHNAKA, K., HINKLE, K. H., RIDGWAY, S. T. (1994). High resolution infrared spectra of silicon monoxide and silicon isotopic abundances in cool luminous stars. *A&A* **289**, 469–491.

Unno, W., Kondo, M. (1976). The Eddington approximation generalized for radiative transfer in spherically symmetric systems. I. Basic method. *PASJ* **28**, 347–354.

Unno, W., Kondo, M. (1977). The Eddington approximation generalized for radiative transfer in spherically symmetric systems. II. Nongray extended dust–shell models. *PASJ* **29**, 693–710.

van Buren, D., Dgani, R., Noriega-Crespo, A. (1994). The wind of EG Andromedea is not dust driven. *AJ* **103**(3), 1112–1114.

Wallerstein, G., Knapp, G. R. (1998). Carbon stars. *ARAA* **36**, 369–434.

Wentzel, D. (1970). On the instability of a stellar envelope due to radiation pressure. *ApJ* **160**, 373–377.

Winters, J. M. (1994). *Internal structure and optical appearance of circumstellar dust shells around cool carbon giants.* Dissertation, Technische Universität, Berlin, FRG.

Winters, J. M. (1998). Dust formation and mass loss in evolved stars. *Ap&SS* **255**, 257–266.

Winters, J. M., Dominik, C., Sedlmayr, E. (1994). Theoretical spectra of circumstellar dust shells around carbon-rich asymptotic giant branch stars. *A&A* **288**, 255–272.

Winters, J. M., Fleischer, A. J., Gauger, A., Sedlmayr, E. (1994). Circumstellar Dust shells around Long-period Variables. II. Theoretical lightcurves of C–stars. *A&A* **290**, 623–633.

Winters, J. M., Fleischer, A. J., Le Bertre, T., Sedlmayr, E. (1996). Optical appearance of dynamical models for circumstellar dust shells around long–period variables: AFGL 3068. In R. F. Wing (Hrsg.), *IAU Symp. 177: The Carbon Star Phenomenon*, Dordrecht, pp. in press. Kluwer Academic Publishers.

Winters, J. M., Fleischer, A. J., Le Bertre, T., Sedlmayr, E. (1997). Circumstellar dust shells around long–period variables V. A consistent time–dependent model for the extreme carbon star AFGL 3068. *A&A* **326**, 305–317.

Winters, J. M., Le Bertre, T., Keady, J. J. (1999). Infrared appearance of dust forming LPVs. In T. Le Bertre, A. Lèbre, und C. Waelkens (Hrsg.), *Asymptotic Giant Branch Stars. I.A.U. Symp. 191*, pp. 261–266. Kluwer.

Woitke, P. (1997). private communication

Woitke, P. (1998). Time-dependent behaviour of cool-star winds. In L. Kaper und A. W. Fullerton (Hrsg.), *Cyclical variability in stellar winds*, pp. 278–288. Springer.

Woitke, P., Krüger, D., Sedlmayr, E. (1996). On the gas temperature in the shocked circumstellar envelopes of pulsating stars I. Radiative heating and cooling rates. *A&A* **311**, 927–944.

Wood, P. R. (1979). Pulsation and mass loss in Mira variables. *ApJ* **227**, 220–231.

Woolf, N. J., Ney, E. P. (1969). Circumstellar infrared emission from cool stars. *ApJ* **155**, L181–L184.

Yamamura, I., de Jong, K., Justtanont, J., Cami, J. (1998). Spectroscopic study of carbon stars with the ISO-SWS. In L. B. F. M. Waters, C. Waelkens, K. A. van der Hucht, und P. A. Zaal (Hrsg.), *ISO's view on stellar evolution*, pp. 351–357. Kluwer Academic Publishers.

Yamamura, I., de Jong, T., Onaka, T., Cami, J., Waters, L. B. F. M. (1999). Detection of warm SO_2 gas in oxygen-rich AGB stars. *A&A* **341**, L9–L12.

ZAHN, J. P. (1980). Stellar convection theory. In D. F. Gray und J. L. Linsky (Hrsg.), *Stellar turbulence*, Berlin, Heidelberg, pp. 1–14. Springer.

Dank

Herzlich bedanke ich mich bei allen, die mich während der Zeit der Erstellung dieser Arbeit begleiteten und unterstützten. Den Mitgliedern des Institutes für Astronomie und Astrophysik danke ich für die Hilfsbereitschaft und Toleranz, die sie mir entgegenbrachten.

Ich danke Herrn Prof. Dr. E. Sedlmayr für die Betreuung meiner Promotion und für die Möglichkeit, diese am Institut für Astronomie und Astrophysik anfertigen zu können. Insbesondere möchte ich Herrn Prof. Dr. E. Sedlmayr für seine stetigen – auch nicht-physikalischen – Denkanstöße danken, die für mich sehr wertvoll waren und unverwechselbar zum Klima dieses Institutes beitragen.

Herrn Priv. Doz. Dr. J.P. Kaufmann danke ich für die Erstellung des Zweitgutachtens, Herrn Prof. Dr. G. von Oppen für die Bereitschaft, den Prüfungsvorsitz zu übernehmen.

Auch unseren SUPER-Usern möchte ich für ihre Unterstützung danken. Wenn die Platte wieder einmal voll, die Rechner hilflos überlastet und damit der Absturz unvermeidlich war, habt Ihr Euch bemüht, trotzdem alles am Laufen zu halten.

Meiner Zimmerkollegin Dr. Beate Patzer danke ich für ihre stete Bereitschaft zu helfen, Fragen zu klären und – ganz besonders – solche auch zu stellen. Hab' Dank für die Tips zum ersten Teil dieser Arbeit.

Dr. Jan Martin Winters gilt mein besonderer Dank für seine Offenheit und für die interessierte, kritische Betrachtungsweise meiner Arbeit. Auch wenn die Zeit wieder einmal knapp wurde, warst Du immer bereit, zu helfen. Vielen Dank für die Korrektur in letzter Minute & die Bierrunden!

Ganz besonders herzlich möchte ich Dr. Peter Woitke danken, ohne dessen unermütliche Unterstützung diese Arbeit in dieser kurzen Zeit nicht hätte beendet werden können. Obwohl Du mit Deinen unbequemen Fragen das Ziel in die Ferne zu rücken schienst, warst Du immer da, wenn ich Dich brauchte.

Meinen Eltern und meiner Schwester möchte ich von ganzem Herzen für das Glück danken, eine solche Familie zu haben. Ohne Euch wäre ich nie bis hierher gekommen.

Lebenslauf

Name	Christiane Helling
Geburtsdatum	11.06.1969
Geburtsort	Merseburg
Eltern	Marlies Helling, Lothar Helling
Staatsangehörigkeit	deutsch
Familienstand	ledig

Schulbesuch

1976–1986	10-klassige Polytechnische Oberschule in Berlin
1986–1988	Erweiterte Oberschule in Berlin
01.07.1988	Abschluß: Abitur (Allgemeine Hochschulreife)

Studium

1989–1990	Studium der Wirtschaftinformatik an der Technischen Universität Dresden
1990–1993	Physikgrundstudium an der Freien Universität Berlin
1993–1996	Physikhauptstudium an der Technischen Universität Berlin
1994–1996	Studien- und Diplomarbeit am Niels-Bohr-Institut, Universität Kopenhagen
Oktober 1996	Abschluß des Physikstudiums an der TU Berlin: Diplom Thema der Diplomarbeit am Institut für Astronomie und Astrophysik: *Application of Opacity Sampling (OS) and Opacity Distribution Function (ODF) to Model Calculations of Cool Giants*

Beruflicher Werdegang

1988–1989	Praktikum im Rechenzentrum des EVDR - Bahnconsult
1993	Praktikum im Bereich Vorentwicklung bei BMW - München
1997–1999	Stipendiatin der FAZIT-Stiftung am Institut für Astronomie und Astrophysik der TU Berlin

61 *Manche sah ich da, die der Mißgunst sich*
Um anderer Glück ergaben.
Blutge Runen standen auf ihrer Brust
Vermerkt des Meineids halber.

62 *Manchen sah ich da, der weglos mußte*
In der Öde traurig irren.
Der Lohn wird dem, der dieser Welt
Eitelkeit sich äffen läßt.

70 *Männer sah ich da, die großmütig*
Den Armen geholfen hatten:
Heilige Bücher lasen die Himmlischen
Über ihren Häuptern.

Die Edda, *Das Sonnenlied*